CHARACTERIZING THE TENSILE BEHAVIOR OF ADDITIVELY MANUFACTURED Ti-6Al-4V USING MULTISCALE DIGITAL IMAGE CORRELATION

BY

DAVID FOEHRING

THESIS

Submitted in partial fulfillment of the requirements
for the degree of Master of Science in Aerospace Engineering
in the Graduate College of the
University of Illinois at Urbana-Champaign, 2017

Urbana, Illinois

Advisers:

Professor John Lambros
Professor Huck Beng Chew

Abstract

In this work, the tensile behavior of an additively manufactured (AM) alloy, titanium 6Al-4V, or Ti-6Al-4V (by wt. 90% titanium, 6% aluminum, 4% vanadium), is examined on multiple length scales using two-dimensional (2-D) digital image correlation (DIC) techniques. Ti-6Al-4V is one of the AM metals that is currently commercially available for use in a variety of engineering applications. This work focuses on characterizing the relationship between the microstructure and bulk mechanical properties of the AM Ti-6Al-4V specimens and understanding how unique microstructural features pertaining to AM metals, such as columnar grain morphology and nonequilibrium phase structures, influence the micro-scale deformation behavior. A low magnification in-situ DIC study (referred to as the macro-scale study) was performed during tension experiments to assess the bulk properties of most specimens while the specimens were loaded, and a high magnification ex-situ DIC study (referred to as the micro-scale study) was performed on a single sample using a microscope after the sample was unloaded and removed from the load frame to observe the heterogeneous strain accumulation at this smaller scale. The experimentally-measured mechanical properties of AM Ti-6Al-4V were compared against conventionally processed Ti-6Al-4V. AM Ti-6Al-4V specimens exhibited greater strength than conventionally processed Ti-6Al-4V due to the acicular, or needle-like, grain structure. In the micro-scale study, alternating regions of high and low strains were observed to accumulate along these needles, or laths. The effects of build orientations (related to microstructure anisotropy), powder bed layering thicknesses (30 and 60 microns), and heat treatment, on the macro-scale properties were examined. A significant decrease in strength was observed in samples subjected to annealing heat treatment as compared to as-built specimens with no heat treatment. This behavior was due to the coarsening of the grain structure observed in scanning electron microscope

images. AM Ti-6Al-4V tension specimens exhibited higher strength when the direction of applied tension was perpendicular to the AM build orientation. Upon further investigation in the micro-scale study, this observed anisotropy is thought to be related to interfaces of consecutively deposited layers as regions of high strain seen in the micro-scale study were observed to accumulate at changes in structure associated with the deposition of layers.

Acknowledgements

I have many people to be thankful for during my time as a graduate research assistant here at the University of Illinois at Urbana Champaign (UIUC). First and foremost, I would like to thank my advisers, Professor John Lambros and Professor Huck Beng Chew, for their guidance on my research throughout this past year. Thank you to my labmates, Robert Waymel, Arthur Ding, Manue Martinez, and Renato Bichara Vieira, for all the help you provided when I needed it. Thanks to Debashish Das for helping me prepare samples as well. I am grateful to Greg Milner and Lee Booher from the Aerospace Engineering Research Machine Shop for manufacturing the various fixtures and parts required to conduct many of the experiments I ran. I would like to thank UIUC's Materials Research Laboratory (MRL) staff for the training services provided to use the scanning electron microscopes (SEM) and vibratory polisher available at MRL, and Peter Kurath for maintaining the equipment at Advanced Materials Testing and Evaluation Laboratory (AMTEL) so I could run my experiments on schedule. Finally, I would like to thank the University of Illinois Research Board for providing the grant that made my research possible.

Table of Contents

Chapter 1: Introduction

1.1 Motivation and Background

Additive manufacturing (AM) is a presently emerging manufacturing technology that is starting to see more widespread use in real world components. There are strong design, cost, material efficiency, and energy efficiency benefits to AM, and AM metals are becoming especially important in the aerospace industry. Although AM with metallic materials is now possible for stainless steel, nickel alloys, aluminum alloys, and titanium alloys, the majority of research efforts on AM metals have focused on the titanium alloy, Ti-6Al-4V, which is of particular interest to the aerospace industry. While the macro-scale mechanical properties of AM Ti-6Al-4V have been widely studied, there is still a lack of understanding of how the unique microstructural features of AM metals influence these bulk properties. Such an understanding is especially important for proper qualification and certification of mission-critical components (Seifi, Salem, Beuth, Harrysson, & Lewandowski, 2016). This is further complicated by the fact that there are several different approaches to producing geometrically-similar AM parts, including a variety of adjustable processing parameters that may lead to large variabilities in the underpinning microstructures.

This work focuses on characterizing the relationship between the microstructure of an AM Ti-6Al-4V alloy produced by GPI Prototype & Manufacturing Services and its macroscale mechanical properties, using the experimental technique of digital image correlation (DIC). One advantage in using DIC as compared to other optical techniques, such as photoelasticity or interferometry, is the ability to obtain 2-D full field strain data at multiple length scales since DIC

has no inherent length scale unlike the aforementioned optical techniques that are limited by the wavelength of light or the optical components used. Two length scales were studied using DIC in this work to characterize the mechanical properties and are presented in two different chapters (Chapters 3 and 4). The first length scale, referred to as the macro-scale, considers the bulk mechanical properties of AM Ti-6Al-4V alloy obtained through static uniaxial tension tests. The second length scale, referred to as the micro-scale, considers the local strains associated with heterogeneities related to the unique microstructure of AM Ti-6Al-4V alloy. The correlation between results obtained at both of these length-scales allows one to relate the mechanical behavior with microstructural features of AM Ti-6Al-4V alloys.

1.1.1 Additively Manufactured Metals

Additive manufacturing is a general term that defines the process of building a solid part from a three-dimensional Computer-Aided Design (CAD) based model by fusing material together layer by layer (Gibson, Rosen, & Stucker, 2015), in contrast to subtractive manufacturing, which starts with a solid piece and removes material until a desired shape is achieved. When applied to metals, AM can include several different types of approaches that can be grouped into three categories according to process type: powder bed fusion (PBF), directed energy deposition (DED), and sheet lamination. These categories and the following content listing the AM techniques are summarized in Table 1.1 borrowed from Dutta and Froes (2016). PBF involves depositing a layer of metal powder, scanning a predefined cross-section of the bed with a heat source to either sinter or completely melt the powder and repeating the process to build a three-dimensional (3-D) part one 2-D cross-section at a time. Two common heat sources used in PBF are an electron beam and a laser beam. Electron beam PBF refers to the electron beam melting (EBM) technique whereas laser beam PBF refers to selective laser sintering (SLS), direct metal laser sintering (DMLS), laser

melting (LM), selective laser melting (SLM), and laserCUSING. DED is a process where material is injected into a meltpool and the part is built up without a surrounding powder bed. This material can be a metallic powder as is the case for direct metal deposition (DMD), laser engineered net shaping (LENS), and direct manufacturing (DM) or it can be a metal wire as in shaped metal deposition (SMD) or wire and arc additive manufacturing (WAAM). To add to the confusion, several of the listed AM techniques are essentially the same, distinguished only in name by the company for which the process was invented (Dutta & Froes, 2016). For the purposes of clarity relevant to this work, a distinction should be made between direct metal laser sintering (DMLS) and direct metal laser melting (DMLM). As they are defined, DMLS does not involve full melting of the material and instead is a sintering process while DMLM involves full melting for highly dense parts (Castells, 2016). Sometimes these terms are used interchangeably and it can be unclear which technique was used. In fact, the specimens used in this work were erroneously labelled as DMLS in prior years before the correction was clarified that these specimens are DMLM (GPI Prototype & Manufacturing Services). A schematic for the laser melted PBF process is shown in Figure 1.1 taken from Dutta and Froes (2016).

Table 1.1: List of additive manufacturing technologies categorized by type and borrowed from Dutta and Froes (2016).

AM Category	Technology	Company	Description
Directed energy deposition (DED)	Direct metal deposition (DMD)	DM3D Technology LLC (formerly POM Group)	Uses laser and metal powder for melting and depositing using a patented close loop process
	Laser engineered net shaping (LENS)	Optomec, Inc.	Uses laser and metal powder for melting and depositing
	Direct manufacturing (DM)	Sciaky, Inc.	Uses electron beam and metal wire for melting and depositing
	Shaped metal deposition or wire and arc additive manufacturing (WAAM)	Not commercialized yet (patented by Rolls Royce Plc.)	Uses electric arc and metal wire for melting and depositing
Powder bed fusion (PBF)	Selective laser sintering (SLS)	3D Systems Corp. (acquired Phenix Systems)	Uses laser and metal powder for sintering and bonding
	Direct metal laser sintering (DMLS)	EOS GmbH	Uses laser and metal powder for sintering, melting and bonding
	Laser melting (LM)	Renishaw Inc.	Uses laser and metal powder for melting and bonding
	Selective laser melting (SLM)	SLM Solutions GmbH	Uses laser and metal powder for melting and bonding
	LaserCUSING	Concept Laser GmbH	Uses laser and metal powder for melting and bonding
	Electron beam melting (EBM)	Arcam AB	Uses electron beam and metal powder for melting and bonding
Sheet lamination	Ultrasonic consolidation	Fabrisonic	Uses ultrasonic energy to consolidate layers of sheet metal and make parts

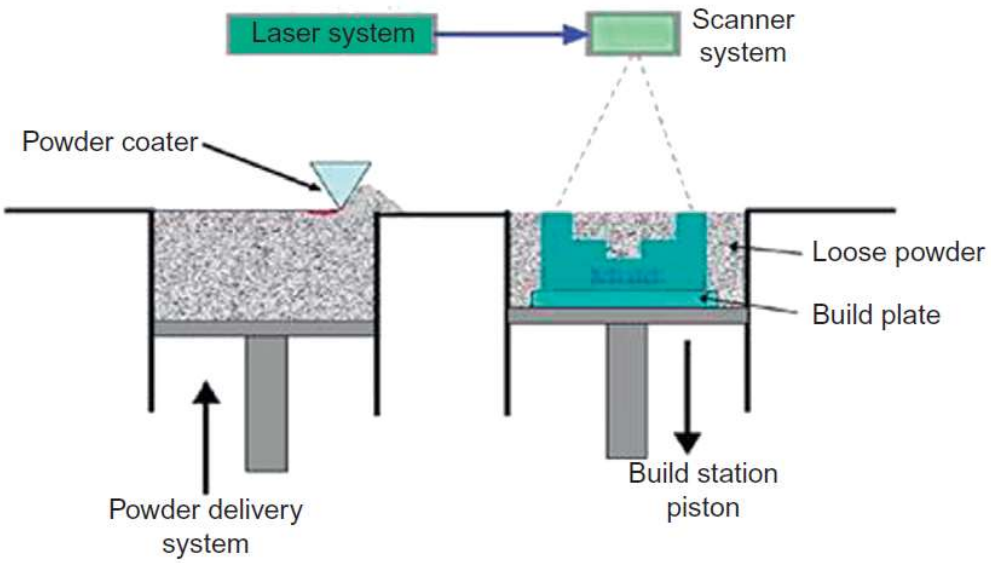

Figure 1.1: Schematic of the laser melted powder bed fusion process borrowed from Dutta and Froes (2016).

There are several variables unique to AM that can be used to control the process of the build, which in turn, affects the resultant material properties. Some variables associated with DMLM are scanning parameters such as laser power, scanning speed, spacing between raster paths (hatch spacing) or raster pattern; environmental conditions such as choice to preheat the powder bed; or other variables like the direction of the build relative to the part dimensions, the powder particle size, or the thickness to deposit for each layer of the build (Lewandowski & Seifi, 2016). To ensure complete fusion of powder particles, scanning parameters are usually selected based on the total energy density that the laser will provide in a relationship shown in Equation 1.1 where energy density, E, is a function of the laser power, P, the scanning velocity, V, the hatch spacing, h, and the layer thickness, t.

$$E = \frac{P}{Vht} \text{ from Gong, et al. (2015)} \tag{1.1}$$

The magnitude of the input energy density has a large effect on the porosity, microstructure, and properties of the AM material. A minimum energy density is required to ensure full powder fusion, but too much energy density can lead to porosity as well due to either entrapped gases or holes left in the melt pool at high energies termed improper closure of the keyhole (Gong, et al., 2015). Anisotropy in the strength of AM metals can be seen due to the directional microstructure seen in the build. Laser melted parts typically show elongated columnar grains aligned with the build direction with various microstructures dependent on the chosen material and processing conditions (Lewandowski & Seifi, 2016). The raster pattern can influence the tilt of these columnar grains with respect to the build direction (Thijs, Verhaeghe, Craeghs, Van Humbeeck, & Kruth, 2010).

The thermal history of laser melted parts can be quite complex due to the cyclic heating of the material as the laser passes several times over the same area not only to initially melt the powder, but also to remelt portions of previous layers to allow fusion of subsequent deposited layers. Even after solidification, laser passes can reheat prior layers to temperatures that can alter the microstructure (Kelly & Kampe, 2004). Cooling rates are often very high, and as a result, as-built (non-heat treated) microstructures are often nonequilibrium and exhibit high strength with low ductility. Parts can be built on preheated substrates or be subjected to post-processing heat treatments to equilibrate the microstructure and increase ductility, often at the expense of strength (Lewandowski & Seifi, 2016).

1.1.2 Titanium 6Al-4V

Titanium 6Al-4V, or Ti-6Al-4V, is a two-phase titanium alloy with alloying contents of 6% aluminum and 4% vanadium by weight. Titanium itself is an allotropic metal that undergoes phase transformation from a hexagonal close packed (hcp) structure (α phase) to a body-centered cubic (bcc) structure (β phase) at around 882ºC. This temperature is often referred to as the β transus temperature (Simonelli, 2014). Various alloying additions work to stabilize either the α or β phase by changing this transus temperature with aluminum being an α phase stabilizer, while vanadium is a β phase stabilizer (Sandala, 2012). The alloying additions to Ti-6Al-4V change the β transus temperature to roughly 995ºC (Vrancken, Thijs, Kruth, & Van Humbeeck, 2012).

Two phase titanium alloys can take on several different types of grain morphologies based on thermal processing history, which can mechanically behave very differently. With the α phase stable at room temperature, two types of α phase dominant morphologies typically formed are a fully lamellar morphology and a bi-modal morphology (Lutjering, 1998). These are seen in Figure 1.2 in images taken from Lutjering (1998). In a lamellar morphology, the α phase forms grains of

narrow laths that dominate the structure. In contrast, a bi-modal morphology contains regions of α lath structure mixed with equiaxed alpha grains (Banerjee & Williams, 2013). A great deal of discussion could be spent on the intricacies of the material structure and properties as a result of the different types of processing routes for titanium, however, this is beyond the scope of this work. Instead, the focus of this thesis will be on structure and properties that result from the complex thermal history present in AM metals.

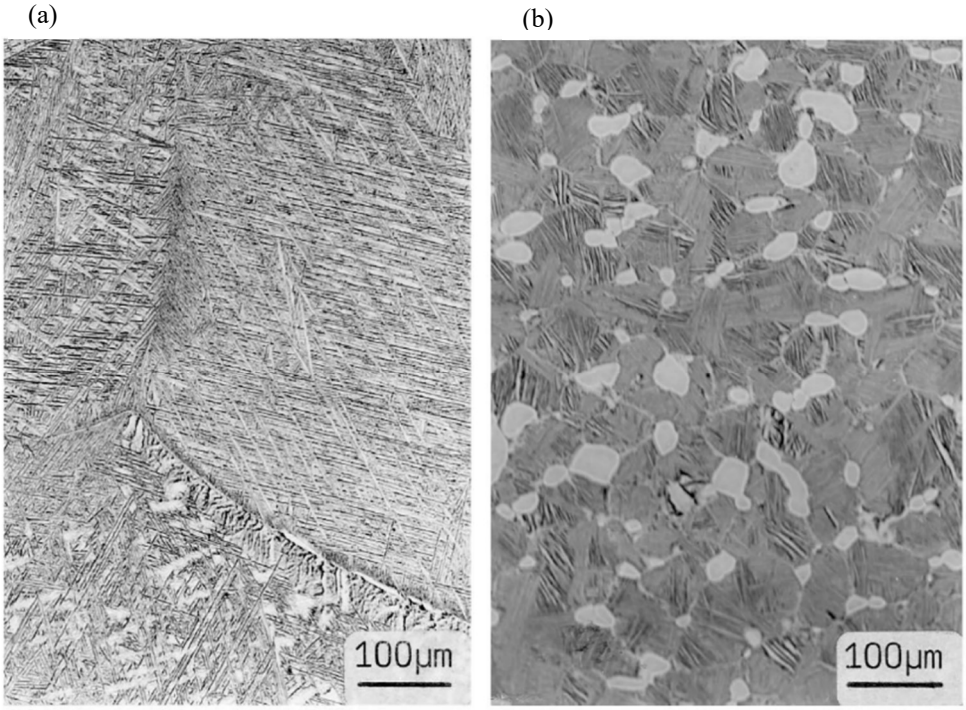

Figure 1.2: Ti-6Al-4V micrographs of a fully lamellar microstructure (a) and a bimodal microstructure (b). Images borrowed from Lutjering (1998).

It has been commonly reported in the literature that the resultant microstructure of Ti-6Al-4V using AM SLM techniques is an acicular, or needle-like, α martensitic structure that forms inside of prior β grain boundaries (Vrancken et al., 2012). Acicular α martensite is a phase structure that forms at very high cooling rates and can transform to a lamellar α phase (coarser laths) and coarsen upon subsequent passes of the scanning laser (Prabhu, Vincent, Chaudhary, Zhang, & Babu, 2015) and (Kelly & Kampe, 2004). In fact, prior layers can be brought to temperatures above the β transus upon reheating of subsequent layers (Kelly & Kampe, 2004). The prior β phase grain boundaries are remnants from the transformation of the Ti-6Al-4V β phase to α phase as the material cools below the β transus. β phase grains need not exist to observe this prior β grain boundary structure (Vrancken et al., 2012).

Prior β grains are usually columnar in appearance with lengths that traverse several deposited powder bed layers in the build direction. The appearance of the prior β grain boundaries can be affected by the input energy as well as the layer thickness used during the build (Wu, et al., 2004) & (Xu, et al., 2015). At higher input energies, the length of the prior beta grains becomes shorter and can appear more equiaxed (Wu, et al., 2004). Also, as the layer thickness increases, so does the width of the prior β grains (Xu, et al., 2015). The α phase can take on several morphologies dependent on the cooling rate and these morphologies can coexist within the same part (Kelly & Kampe, 2004). At high cooling rates faster than 410K/s, acicular α martensite is formed from β. At cooling rates lower than 2K/s, α phase begins to form along β grain boundaries (called grain boundary α) where lamellar α can form into similarly oriented colony structures. If the cooling rate is greater than 2K/s but lower than 20K/s α phase grows directly in the middle regions of the β grains in a lamellar "basketweave" structure (Prabhu et al., 2015). One interesting common observation is that EBM Ti-6Al-4V tends to contain low amounts of martensite due to higher energy inputs and slower cooling rates as compared to laser melted Ti-6Al-4V. This can have the effect of a reduction in yield strength and outlines the importance of process parameter control on the microstructure (Xu, et al., 2015). The influence of other processing parameters not discussed here on the microstructure of AM Ti-6Al-4V is detailed in several works including Wu, et al. (2004), Thijs, et al. (2010), Xu, et al. (2015), and Yang, et al. (2016).

As aforementioned, the different phases and morphologies ultimately control the mechanical properties of Ti-6Al-4V alloys. Since as-built (non-heat treated) AM Ti-6Al-4V microstructures are lamellar type grain morphologies in nature, a short description will be given here on what each phase contributes to the overall properties for lamellar microstructures (Vrancken et al., 2012). The most influential feature for lamellar microstructures is the α colony

size, which effectively sets the slip length for the material. Reducing this slip length is key to increasing the strength, and at high enough cooling rates such as that required to form martensite, the slip length effectively becomes the width of a single α plate. At the other end of the spectrum, the maximum α colony size and slip length is limited by the size of the β grain boundaries. Ductility first increases with increasing cooling rate in lamellar structures, then decreases after reaching a maximum. This is due to a change in failure mode from a ductile transcrystalline dimple type to a ductile intercrystalline dimple type of fracture that occurs along α-layers at β grain boundaries (Lutjering, 1998). Fracture usually occurs in titanium alloys where highly planar localized shear bands result in a shear related fracture or where strain compatibility causes the formation of microvoids at interfaces (Banerjee & Williams, 2013).

1.1.3 Digital Image Correlation

One of the main experimental techniques used in this work was digital image correlation (DIC). DIC is a technique where images taken at different times are compared to observe the motion and/or deformation of an object (Sutton, Orteu, & Schreier, 2009). Specifically, the intensities of groups of pixels in one image are compared to the intensities of pixel groups in another using optimization techniques. Groupings of pixels referred to as subsets are compared rather than individual pixels since pixel intensity values are generally not unique within a given image. A subset defined in a reference image is found in a second image using an algorithm that minimizes the square differences in gray-scale values for the pixels defined in that subset and a subset in the second image. Subset locations are then defined by points usually located at the center of that subset. The location of a subset in one image is then compared to the location of the same subset in another image to find the subset displacement. By correlating several subsets between

images within a region on the sample surface, a 2-D field of surface displacements can be found. This displacement field can then be converted into a strain field.

To illustrate the motion of a point within a subset between two images, a schematic of subset motion is shown in Figure 1.3. The location of point, q', in *x* and *y* coordinates within a deformed subset with center, p', can be related to point, *q*, in a reference subset with center, *p*, using a Taylor series expansion given in Equations 1.2 and 1.3.

$$x'_p = x_q + u_p + \frac{\partial u_p}{\partial x}\Delta x + \frac{\partial u_p}{\partial y}\Delta y + \frac{1}{2}\frac{\partial^2 u_p}{\partial x^2}\Delta x^2 + \frac{1}{2}\frac{\partial^2 u_p}{\partial y^2}\Delta y^2 + \frac{\partial^2 u_p}{\partial x \partial y}\Delta x \Delta y \tag{1.2}$$

$$y'_p = y_q + v_p + \frac{\partial v_p}{\partial x}\Delta x + \frac{\partial v_p}{\partial y}\Delta y + \frac{1}{2}\frac{\partial^2 v_p}{\partial x^2}\Delta x^2 + \frac{1}{2}\frac{\partial^2 v_p}{\partial y^2}\Delta y^2 + \frac{\partial^2 v_p}{\partial x \partial y}\Delta x \Delta y \tag{1.3}$$

$$\Delta x = x_q - x_p \tag{1.4}$$

$$\Delta y = y_q - y_p \tag{1.5}$$

In Equations 1.2 and 1.3 and the schematic in Figure 1.3, variables include *x* and *y* coordinates of point *q*, x_q and y_q; deformed *x* and *y* coordinates of point *q*, now called q', $x'_{q'}$ and $y'_{q'}$; the initial *x* and *y* coordinates of point *p*, x_p and y_p; *x* and *y* components of the displacement of point *p,* u_p and v_p, respectively; partial derivatives of u_p in the *x* direction, $\frac{\partial u_p}{\partial x}$, u_p in the *y* direction, $\frac{\partial u_p}{\partial y}$, v_p in the *x* direction, $\frac{\partial v_p}{\partial x}$, and v_p in the *y* direction, $\frac{\partial v_p}{\partial y}$; and second derivatives of u_p and v_p, $\frac{\partial^2 u_p}{\partial x^2}$, $\frac{\partial^2 u_p}{\partial y^2}$, $\frac{\partial^2 v_p}{\partial x^2}$, $\frac{\partial^2 v_p}{\partial y^2}$, $\frac{\partial^2 u_p}{\partial x \partial y}$, and $\frac{\partial^2 v_p}{\partial x \partial y}$. Additionally, the terms *Δx* and *Δy* indicate the difference in the *x* component and *y* component of points *p* and *q* as defined in Equations 1.4 and 1.5. The terms containing derivatives allow the subset to change size and shape.

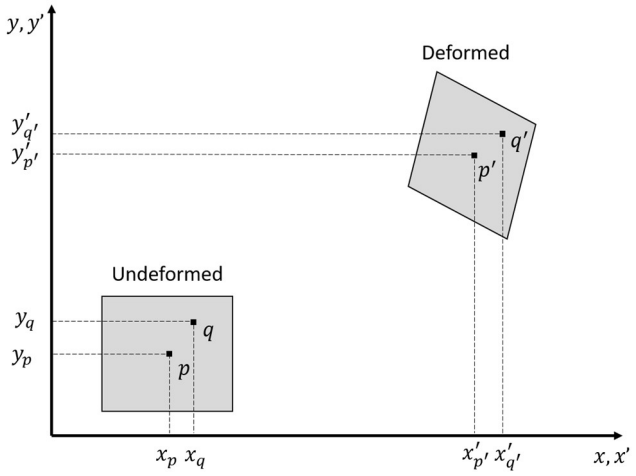

Figure 1.3: Schematic showing subset motion as well as motion within a subset.

One trait a specimen must have to effectively correlate surface displacements is a surface pattern or texture. To eliminate some of the issues that arise during correlation, ideal surface patterns or textures should contain no preferred orientation and be non-periodic. Distributions in grayscale pixel intensities for images of surface patterns are usually presented in histograms as a metric for the quality of the pattern. Pixel intensity distributions with single peaks are usually preferred (Abanto-Bueno, 2004). Because the length scale limitation for DIC is based on the pattern scale and not a distance, it has the major advantage of use at many different length scales. This allows for a multi-scale approach to measuring surface deformations and the ability to capture heterogeneous strain accumulation along slip bands and grain and twin boundaries as seen in Carroll, Abuzaid, Lambros, and Sehitoglu (2013) or the transfer of slip across grain boundaries as seen in Abuzaid Sangid, Carroll, Sehitoglu, and Lambros (2012).

1.2 Objectives

The overarching goal of this work is to characterize and relate the microstructural features to the bulk mechanical properties of AM Ti-6Al-4V alloys. The specific objectives are as follows:

- To characterize the mechanical properties of the AM Ti-6Al-4V specimens using uniaxial tension experiments, determine if there are any differences due to a change in build orientation or layer thickness, describe these possible differences, and compare measured properties to those seen in literature.
- To characterize the microstructure of the as-built specimens, observe changes due to build orientation or layer thickness effects, and determine the features unique to the AM process.
- To evaluate the effects any characteristic microstructural features, especially those possible features unique to the AM process, have on the material deformation behavior by mapping strain accumulation to microstructural features. This particular approach has not been seen in literature for AM metals at the present time.

1.3 Overview

This overview section is provided as a guide for navigating the material presented in this work. The second chapter gives specific information on the nature and preparation of specimens used in this work as well as specific descriptions on the experimental methods used such as the validation and use of in-situ macro-scale DIC and ex-situ micro-scale DIC, uniaxial static tension experiments, hardness testing, and analytical scanning electron microscope (SEM) measurements such as electron backscattered diffraction. Chapter 3 focuses on the results of in-situ macro-scale DIC uniaxial static tension experiments and includes a discussion and comparison with results found in literature specific to AM Ti-6Al-4V. Then, Chapter 4 explores the mechanical behavior observed from ex-situ micro-scale DIC measurements with a focus on directly relating calculated surface strains to microstructural features. These measurements result from loading a Ti-6Al-4V sample into the plastic region of a stress-strain curve in two separate cycles and observing the accumulated strains after the sample is unloaded. Measurements are then related to microstructural

features seen in SEM images. Finally, conclusions from Chapters 3 and 4 are summarized and recommendations for future work are made.

Chapter 2: Experimental Techniques

2.1 Specimen Information and Preparation

2.1.1 Tensile Specimens

Due to the directionality associated with the additive manufacturing process, it is necessary to define a coordinate system for the build process. For this purpose, the ASTM/ISO standard 52921 will be used (ISO/ASTM International, 2013). A schematic illustrating this coordinate system is shown in Figure 2.1 where the *z*-axis is the build direction and the *x* and *y*-axes correspond to the in-plane directions of the scan. Even more specifically, the *x*-axis is parallel to the front of the machine and the *y*-axis is orthogonal to both the *x* and *z*-axes. However, for the purposes of these experiments, the *x* and *y*-axes are considered indistinguishable as any differences between the two will be small compared to the differences between *z*-direction and *x* or *y*-directions. To complete the definition of sample orientation, the sample dimensions must be defined with respect to the coordinate system of the build process. For flat plate-type tension specimens, the longest dimension is stated first with the orientation of that direction defined. Then, the second largest dimension is stated second with its respective orientation and finally the smallest dimension stated last with the final orientation. For cylindrical parts, this nomenclature is simplified to labelling parts per whichever axis the cylinder axis aligns. This is again shown schematically in Figure 2.1.

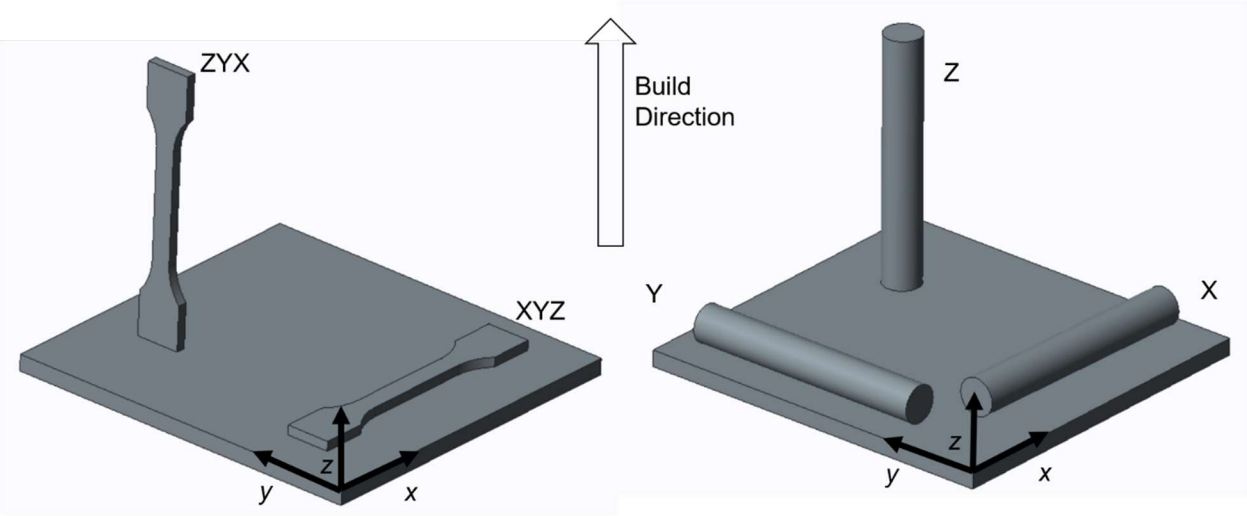

Figure 2.1: ASTM Standard 52921 AM part nomenclature and coordinate system.

All specimens used in this work were made of direct metal laser melted (DMLM) Ti-6Al-4V and were of flat plate-type test specimen geometry that fell within ASTM standard E8/E8M – 16a guidelines (ASTM International, 2016). Processing parameters used during the build are unknown. The dimensions of the tensile specimen geometry are shown in Figure 2.2. Samples were built in two different orientations, ZXY and XYZ, and using two different powder bed layer thicknesses, 30µm and 60µm. Additionally, a few samples were heat treated at 850°C for 5 hours and cooled in air to assess the effects on mechanical properties of a release of possible residual stresses present after manufacture following a modified heat treatment procedure seen in Vrancken et al. (2012). Table 2.1 gives an overview of the experiments performed on the specimens used in this work along with their build orientations and layer thicknesses.

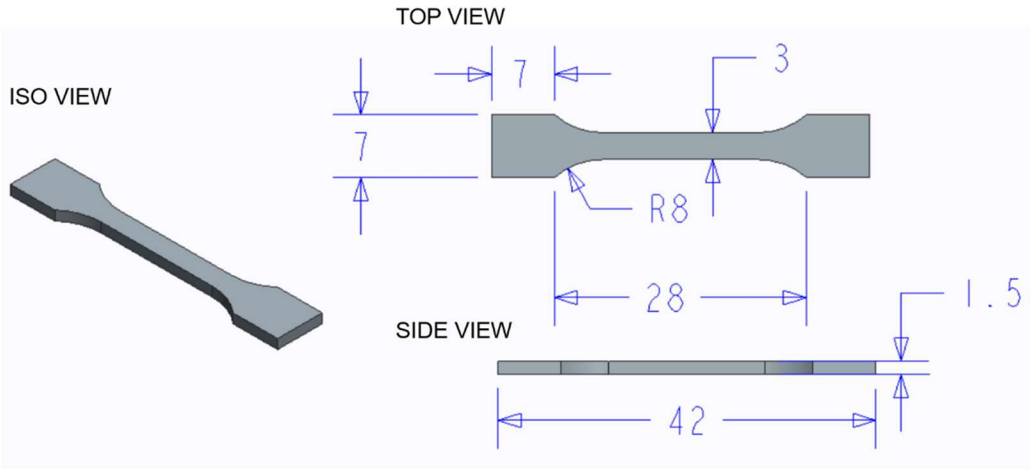

Figure 2.2: Flat plate-type tension specimen dimensions. All dimensions shown are in mm.

Table 2.1: List of Ti-6-4 samples used in this work and the types of experimentation methods performed on them. The axis labelling refers to that outlined in Figure 2.1 and the 30 or 60 refers to the powder bed thicknesses of 30µm and 60µm, respectively. AB indicates samples tested in the as-built condition without any heat treatment, HT refers to samples that underwent heat treatment of 850ºC for 5 hours and while the annealed temper refers the conventionally processed sample purchased from McMaster-Carr that was given an annealing heat treatment of any time and temperature (McMaster-Carr Supply Company [US], 2017).

Sample	Manufacturing Type	Build Orientation	Temper	Layer Thickness (µm)	In-Situ DIC	Ex-Situ DIC
Z30AB-1	AM	ZXY	AB	30	Yes	No
Z30AB-2	AM	ZXY	AB	30	Yes	No
Z30AB-3	AM	ZXY	AB	30	Yes	No
Z30AB-4	AM	ZXY	AB	30	No	Yes
Z30HT-1	AM	ZXY	HT	30	Yes	No
Z30HT-2	AM	ZXY	HT	30	No	No
Z60AB	AM	ZXY	AB	60	Yes	No
XY30AB-1	AM	XYZ	AB	30	Yes	No
XY30AB-2	AM	XYZ	AB	30	No	No
XY60AB	AM	XYZ	AB	60	Yes	No
Conventional	Conventional	N/A	Annealed	N/A	No	No

2.1.2 In-Situ and Ex-Situ DIC Measurements

Two approaches to DIC measurements seen in Table 2.1 were used in this work. One approach was used during the uniaxial tension experiments where images were captured at a defined frequency while a specimen was loaded and DIC-calculated strain could be compared

directly to the extensometer measured strain. This is referred to as the in-situ measurement. The other approach was to take surface images before performing a tension experiment, then interrupting the experiment at a pre-defined strain level after material yielding and unloading the sample to take further images. These two sets of images would then be correlated in what will be referred to as the ex-situ measurement approach.

Somewhat related to these two measurement approaches are the magnification levels used for DIC measurements. In-situ measurements were taken at lower magnifications than ex-situ measurements due to practical difficulties of high magnification image capturing (see section 2.2.6). However, it is not impossible to capture higher magnification in-situ measurements, and lower magnification ex-situ measurements are easily obtainable. Because of this distinction, a clear definition on magnification will be made here. Low magnification will be defined as any measurement where resolutions greater than 1μm per pixel are used whereas high magnification will refer to measurements able to resolve less than 1μm per pixel.

2.1.3 Digital Image Correlation Sample Preparation

Tensile sample preparation for both in-situ and ex-situ DIC measurements involved several steps that will be detailed here. In summary, sample preparation contained three major steps: grinding, polishing and patterning. Table 2.2 at the end of this section summarizes the grinding and polishing procedure. Due to the high surface roughness of the AM Ti 6-4 samples compared to the physical size of the specimens as seen in Figure 2.3, grinding was needed on all four faces in the reduced cross-section region of the tensile specimen. This allowed the "load bearing" cross-section to be measured more accurately since many of the surface particles did not realistically contribute to this area, thus allowing stress to be estimated more accurately. Powder particle size can be roughly estimated based on images of partially melted particles attached to the surface seen

in Figure 2.3, and it appears particles up to 30µm in size were used on the 30µm layer thickness sample. Particle size on the 60µm layer thickness samples is still unknown. Grinding the flat sides of the samples consisted of using a series of silicon carbide grinding papers on a Struers DAP-V wheel. This machine had a tap water feed that continuously ran during the grinding steps. Initial grinding was done with 320 grit (P400) paper on the wheel with even pressure applied by hand. This removed the surface roughness from manufacturing and allowed coarse speckle patterns to be applied for low magnification DIC. If higher magnification DIC was needed, as it was for most samples in this work, the initial 320 grit grinding allowed the sample to be mounted to a grinding and polishing fixture, using Crystalbond 555HMP low melting point adhesive. The sample was again ground with 320 grit paper until it became planar with the fixture and no beveling of the sample was visually apparent. It was noticed that this step often resulted in the sample bending and ultimately debonding after significant material removal – a fact which is attributed to the presence of residual stresses near the surface that were relieved during surface grinding. In the event this did occur, samples were then rebonded to the fixture and re-flattened. The 320 grit grinding step was subsequently followed by 600 grit (P1200) and 800 grit (P1500) grinding steps to finish the grinding procedure. Care was taken to clean the sample, fixture, and polishing wheel with soap and water between steps to ensure larger particles did not induce large scratches during the finer grinding steps. For some samples, this three-step grinding procedure proved to be enough for a fine speckle pattern to be subsequently applied. In fact, 800 grit was found to be sufficient for patterns generated with an airbrush due to the limitations of the speckle size achieved.

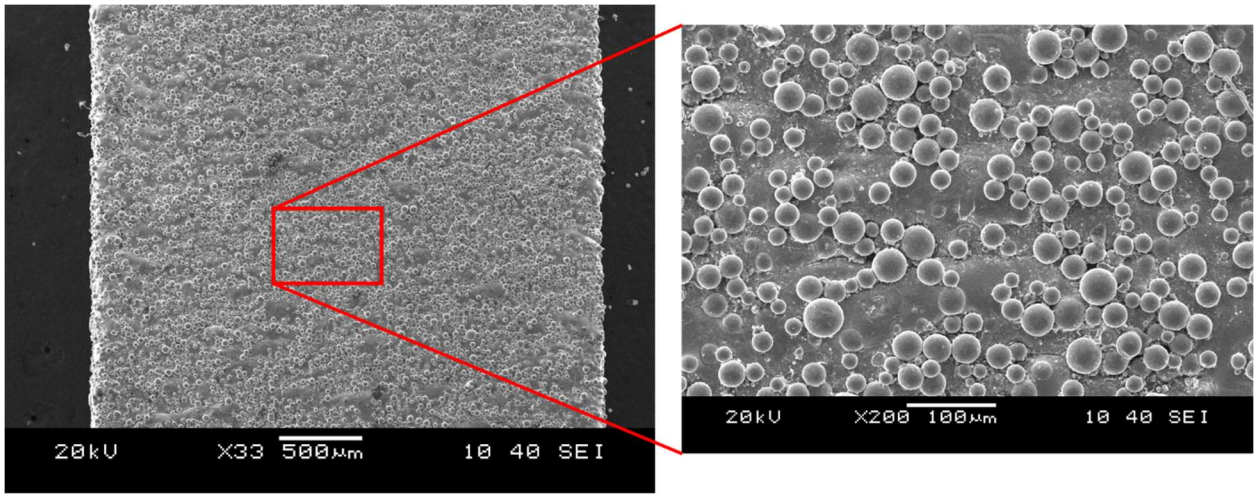

Figure 2.3: As-built surface roughness on an AM tensile sample as seen from secondary electron imaging on JEOL 6060LV scanning electron microscope.

Like the grinding procedure, the polishing procedure consisted of three steps. The first step used a 9µm diamond suspension on a Buehler Ultra-Pad polishing pad. The sample was contra-rotated while the Struers DAP-V wheel was spinning at low rpm to prevent comet tailing. This step lasted for ten minutes. A 3µm diamond suspension and Buehler Trident polishing pad was used for the second polishing step. Again, the sample was contra-rotated on the wheel for the entire ten-minute duration of the polishing step. Distilled water was added periodically to provide lubrication during the first two polishing steps. Final polishing was performed on a vibratory polishing machine at University of Illinois' (UIUC) Materials Research Laboratory (MRL) with an alumina suspension for four to six hours for most samples. Some samples were polished even longer (up to 17 hours) and exhibited surface topology associated with certain microstructural features.

Table 2.2: Grinding and polishing procedure

Step	Type	Paper/Pad	Compound	Lubricant	Contra-rotation
1	Grinding	320 grit (P400) Silicon Carbide	N/A	tap water	No
2	Grinding	600 grit (P1200) Silicon Carbide	N/A	tap water	No
3	Grinding	800 grit (P1500) Silicon Carbide	N/A	tap water	No
4	Polishing	Buehler Ultra-Pad	9µm diamond	distilled water	Yes
5	Polishing	Buehler Trident Pad	3µm diamond	distilled water	Yes
6	Polishing		0.15µm alumina	polishing slurry	No

Speckle patterning of specimens for the DIC technique was achieved in one of three ways based on the resolution requirements of the pattern. For low magnification strain field measurements, a black spray paint was applied directly from the can by angling the can nozzle slightly away from the sample allowing the paint to fall onto the surface in a misting manner. Patterns suitable for low and high magnification measurements were applied using an airbrush and spray paint thinned with acetone. Finally, patterns that allowed high magnification DIC measurements in these experiments were achieved by depositing filtered fine silicon powder particles on the surface using compressed air in a technique outlined in more detail in Jonnalagadda et. al. (2010). Examples of patterns using these three techniques are seen in Figure 2.4.

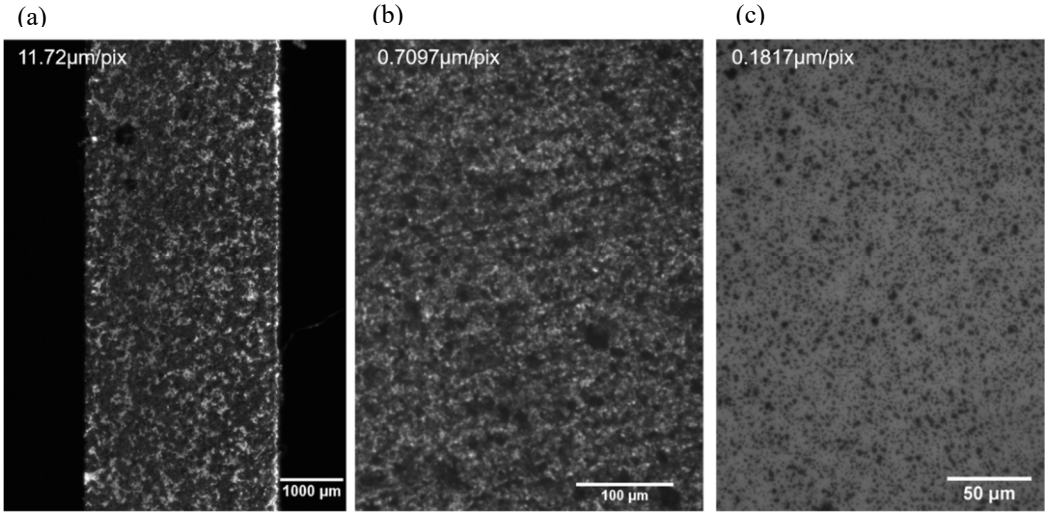

Figure 2.4: Typical patterns seen with (a) the spray paint "misting" technique, (b) the airbrush, and (c) silicon powder particle deposition.

2.2 Experiments and Measurements

2.2.1 Digital Image Correlation Technique Validation

To validate the DIC technique for the airbrushed speckle pattern and the silicon powder particle pattern shown in Figure 2.4, a set of experiments was created to determine the error associated with DIC as well as the ability of the technique to capture applied displacements and rotations. For the error measurement experiment, two different cameras, a Prosilica GX 1050 and an Olympus Q-Color3, were used. Rigid body motion experiments were done using the Prosilica camera. These two cameras were the same ones to be used in the in-situ (Prosilica) and ex-situ (Olympus) imaging of the tension samples described a bit later. The two macro lenses used for in-situ low magnification DIC measurements were a TAMRON SP AF 180mm F/3.5 Di LD[IF] Macro 1:1 and a Navitar 12X Zoom lens with 2X adapter. These were used with the Prosilica camera while the Olympus camera was attached to a microscope for high magnification ex-situ DIC.

In the first experiment, referred to as the baseline noise experiment, two images were taken consecutively of a speckle-patterned tensile specimen that was clamped in place without any motion or deformation between images. For the Prosilica camera baseline noise measurement a tensile specimen was speckle-patterned with spray paint. The sample used for the Olympus camera noise measurement had a pattern obtained using the silicon powder particle deposition method. Both speckle patterns are shown in Figure 2.5 with their respective histograms and show a distribution of pixel intensities without any high pixel counts at grayscale values of either 0 or 255 indicating that no grayscale values below or above the intensity detection range limits of the camera were artificially assigned values of 0 or 255. This is usually referred to as clipping.

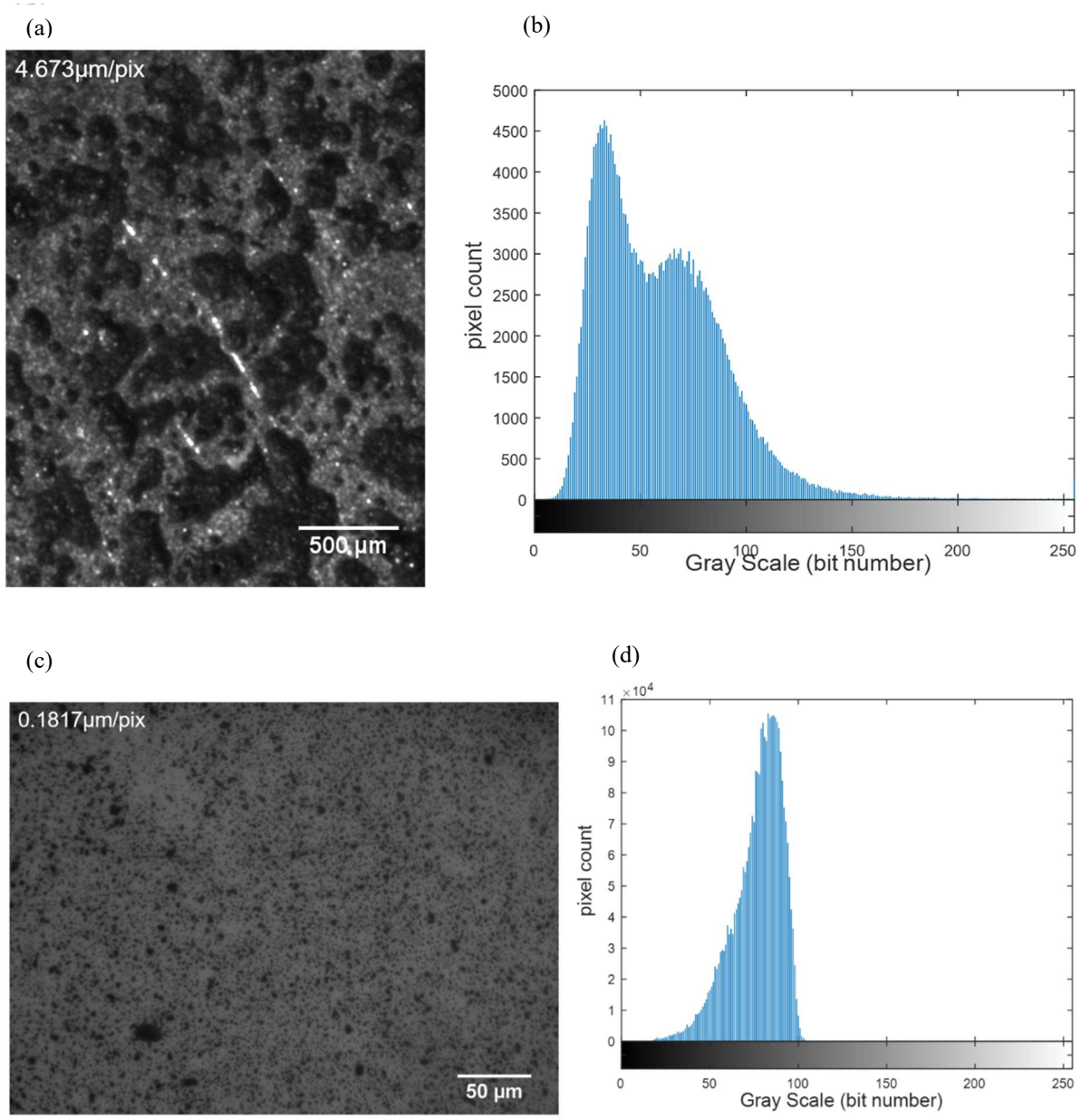

Figure 2.5: Baseline noise tests on each camera were performed on two speckle patterns made with (a) spray paint and (c) silicon powder. Their histograms are seen in (b) and (d), respectively.

The baseline noise experiment allows for the characterization of inherent system measurement error as any displacement computed by the VIC 2-D correlation software is due to camera, lighting, support and/or pattern noise. It represents the baseline DIC resolution limitations obtainable for a particular pattern and camera combination. Camera noise is usually random in nature, so any computed displacement field should appear as randomly oriented vectors in a quiver

plot. The quiver plots for both specimens are shown in Figure 2.6. Table 2.3 and Table 2.4 show the magnitude of the average motion and the standard deviation of motion calculated in both pixels and μm for both baseline noise measurements. It is important to note that the standard deviation is significantly lower than one pixel indicating that sub pixel displacement resolution is possible with DIC.

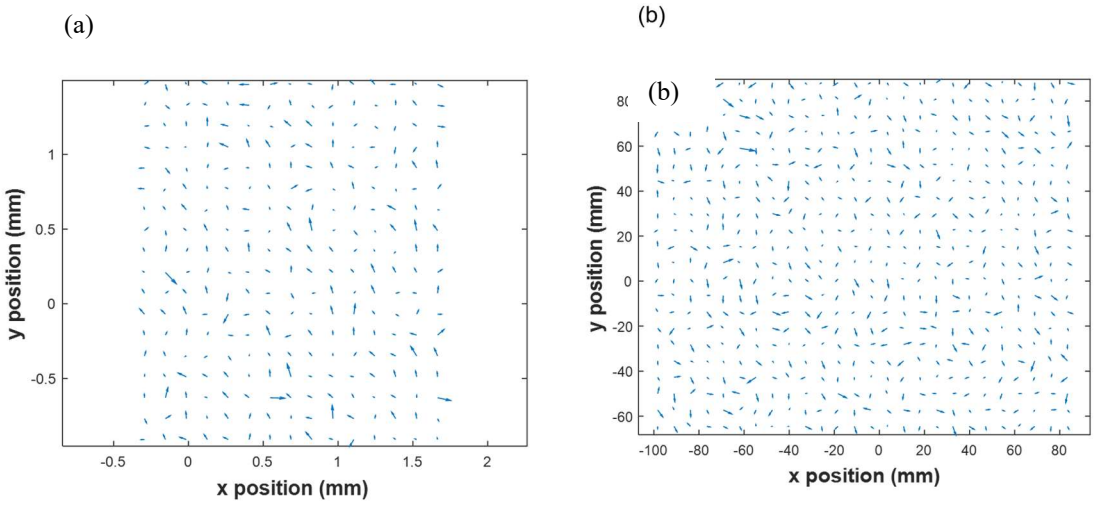

Figure 2.6: Quiver plot showing the calculated motion due to random noise for the (a) Prosilica GX camera and (b) the Olympus Q-Color3 camera. For visualization purposes, arrows are scaled by a factor of 100 and only every third arrow is plotted in (a). Also, arrows are scaled by a factor of 200 and only every eighth arrow is plotted in (b).

Table 2.3: Average and standard deviation of correlation point displacements for Figure 2.6(a).

Prosilica Baseline Test	***u* (pixels)**	***v* (pixels)**	***u* (μm)**	***v* (μm)**
mean	-0.0168	-0.0303	-7.82E-05	-1.41E-04
standard deviation	0.0425	0.0487	1.98E-04	2.27E-04

Table 2.4: Average and standard deviation of correlation point displacements for Figure 2.6(b).

Olympus Baseline Test	***u* (pixels)**	***v* (pixels)**	***u* (μm)**	***v* (μm)**
mean	0.0088	0.0228	0.0016	0.0041
standard deviation	0.0350	0.0336	0.0064	0.0061

The second calibration experiment was a rigid body translation measurement of the spray paint speckle-patterned tensile specimen. This consisted of clamping a sample to a translation stage

and applying a specific known rigid body displacement and then using the DIC technique to calculate the resulting displacement. The displacement resolution of the screw-driven translation stage was defined by tick marks on the turn wheel at 0.01mm. In this experiment, a uniform displacement field seen across the region of interest implies rigid body translation, and that is what is seen in the quiver plot in Figure 2.7(a) below. This was done for a variety of displacement magnitudes, and the measured displacements averaged over the field from DIC are plotted against applied displacements in Figure 2.7(b) showing measurements that closely follow a line with a slope equal to one. The spatial resolution for this experiment was 15.6 µm per pixel, while a subset size of 40 was used with a step of 15 pixels for a total of 550 data points.

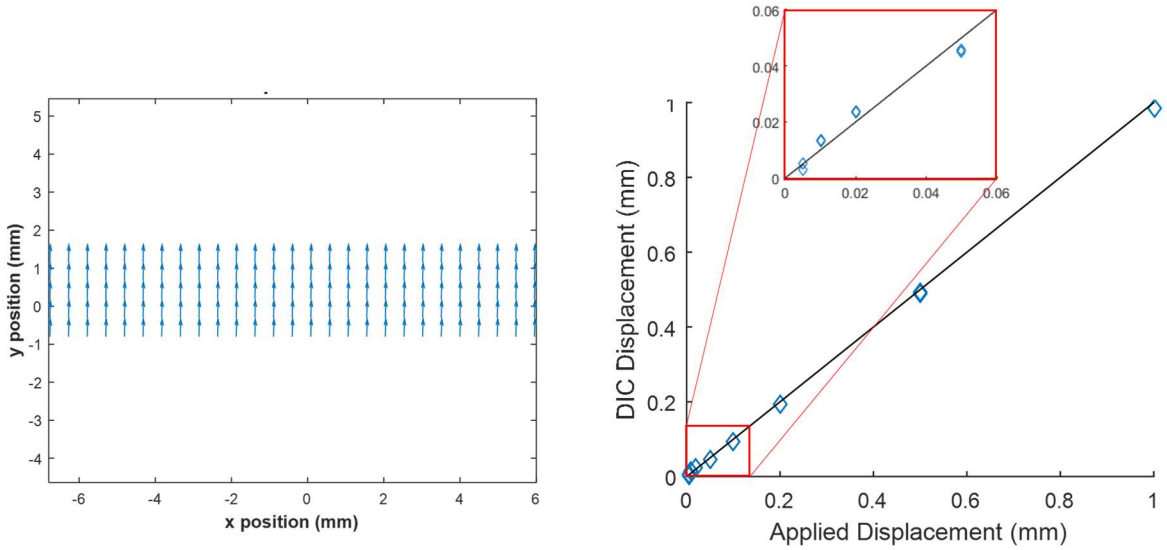

Figure 2.7: (a) Quiver plot showing the displacement field for an applied displacement of 0.5mm. Arrows are scaled by a factor of 0.75 and every other arrow is plotted. (b) Plot of the applied displacement vs. the average measured displacement from DIC. A line with a slope of one is plotted to compare against.

An attempt was made to determine the minimum applied displacement interval that would be captured by DIC and due to the displacement increment resolution of the translation stage, the minimum applied displacement practically achievable in this experiment was 0.01 mm. Nonetheless, when this displacement was applied a calculated DIC displacement agreeing within

1 percent error was observed. At the 15.6 μm per pixel spatial resolution used, this corresponds to a displacement of 0.64 pixels indicating sub-pixel motion resolution is achievable.

The final DIC technique validation experiment tested the ability of DIC to capture rigid body rotation. In a similar manner to the rigid body translation experiments, the same sample was clamped to a rotation stage with tick marks such that a minimum rotation angle of 0.5º was achievable and applied rotations were compared to the measured rotations from DIC. A pixel spatial resolution of 23.4 μm per pixel was used with a subset of 40 and a step of 50 pixels for a total of 39 correlation points. A quiver plot resulting from an applied rotation of three degrees is shown in Figure 2.8(a) where the magnitude of displacement increases linearly with distance from the center of rotation. Rotation angle, θ, was calculated using Equation 2.1 and averaged over the entire field where v represents the displacement in the y-direction in a standard two-dimensional coordinate system, x represents the x-coordinate position, and i represents the point of rotation calculation (Abanto-Bueno, 2004). A plot showing the average measured rotation over the field versus the applied rotation is shown below in Figure 2.8(b) with the line $y=x$ plotted alongside.

$$\tan\theta = \frac{v_{i+1}-v_i}{x_{i+1}-x_i}, i = 1,2,3,\dots n \tag{2.1}$$

(a) (b)

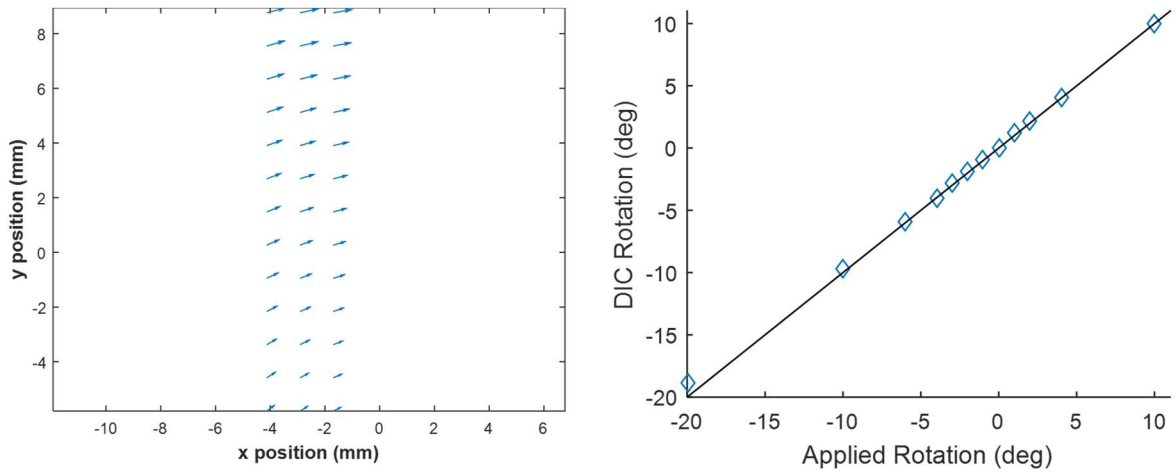

Figure 2.8: (a) Quiver plot showing the displacement field for an applied rotation of three degrees. Arrows are scaled by a factor of 0.5. (b) Plot of the applied rotation vs. the average calculated rotation from DIC with a $y=x$ plotted for comparison

In practice, there is a minimum rotation angle that can be correlated using DIC as well as a maximum angle. Attempts were made to quantify these angles and the measurement error associated with them. A rigid body rotation of 1º gave an error of 7.58% between the measured and applied rotations while on the other end, an applied rotation of -20º gave an error of 5.86%. For reference, 1.88% error was measured at an intermediate angle of three degrees shown in Figure 2.8. These values of error agree reasonably well with those given in Abanto-Bueno (2004).

2.2.2 Hardness Tests

Micro hardness tests were conducted using a Shimadzu micro hardness tester HMV-M on many of the tension specimens in this work. These indentations were used as the fiducial markers to align images taken ex-situ. The nature of these fiducial markers will be discussed in more detail later. In addition, these indentations provided information on the hardness variation between samples when converted using the Vickers scale in Equation 2.2 where d is the averaged diagonal measurement of each indentation and F is the force in kgf, which was set at 0.3 kgf.

$$HV = 1.8544\frac{F}{d^2} \quad (2.2)$$

Diagonal distances were measured as pixel distances using images taken on an optical microscope with a 20X objective magnification lens and converted to μm using known a known 0.3492 μm per pixel resolution (see section 2.2.6 for more details on this calculated resolution). All samples were fully polished using the procedure outlined in section 2.1.3 before testing.

2.2.3 Ultrasound Experiments

A set of ultrasound experiments were performed to determine the elastic modulus of the DMLM Ti-6Al-4V samples in a non-destructive manner and validate the modulus measured via uniaxial static tension experiments. The procedure for these experiments was as follows. An ultrasonic transducer and an ultrasonic detector were coated in honey to ensure good coupling and placed in contact with the sample to be tested. An ultrasonic wave generator produced an ultrasonic wave through the transducer, which travelled through the part and the signal was detected by the detector and acquired on an oscilloscope. A schematic of this experimental setup is given in Figure 2.9. One set of transducers and detectors was included for measuring normal or dilatational ultrasonic waves while another set was used for measuring shear waves. Using the measured length of the part, the time delay between sending and detecting the signal, and a known material density obtained from an ASM online database (ASM Aerospace Specification Metals Inc. (a)), the elastic modulus of the material could be calculated with Equations 2.3a-e. The mathematical symbols included in these equations are the elastic modulus (E), dilatational wave time (T_d), shear wave time (T_s), dilatational wave speed (C_d), shear wave speed (C_s), Poisson's ratio (ν), material density (ρ), and shear modulus (μ).

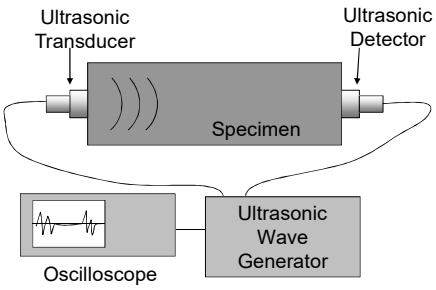

Figure 2.9: Schematic of the ultrasound experiments used to determine the elastic modulus of the DMLM Ti-6Al-4V.

$$C_d = \frac{d}{T_d} \tag{2.3a}$$

$$C_s = \frac{d}{T_s} \tag{2.3b}$$

$$\mu = C_s^2 \rho \tag{2.3c}$$

$$\nu = \frac{\frac{1}{2}\left(\frac{C_d}{C_s}\right)^2 - 1}{\left(\frac{C_d}{C_s}\right)^2 - 1} \tag{2.3d}$$

$$E = 2\mu(1+\nu) \tag{2.3e}$$

2.2.4 Uniaxial Static Tension Experiments

Uniaxial tension experiments were performed at UIUC's Advanced Materials Testing and Evaluation Laboratory (AMTEL) at Talbot Laboratory on an Instron 8500R test machine fitted with a 1000kN load cell on the flat plate-type tension specimens. The load frame along with the in-situ DIC setup is pictured in Figure 2.10. A Labview program was used to control the machine. Tension experiments were run using position control where a defined displacement rate of 0.01 mm/s was used. After vertically aligning the sample in the Instron machine using a fixture, an Instron 2620-826 extensometer was attached to the sample using a few rubber bands as a secondary strain measurement to the in-situ DIC strain measurement. Position, load and strain from the

extensometer were sampled at 2 Hz and synchronized with the image capturing rate for the in-situ DIC measurement and when combined with the displacement rate, resulted in anywhere from 100-300 data points during the loading duration of each sample. Some samples were loaded to failure, while for others loading was interrupted at specific strain levels after material yielding to view the plastic strain accumulation using ex-situ DIC measurements.

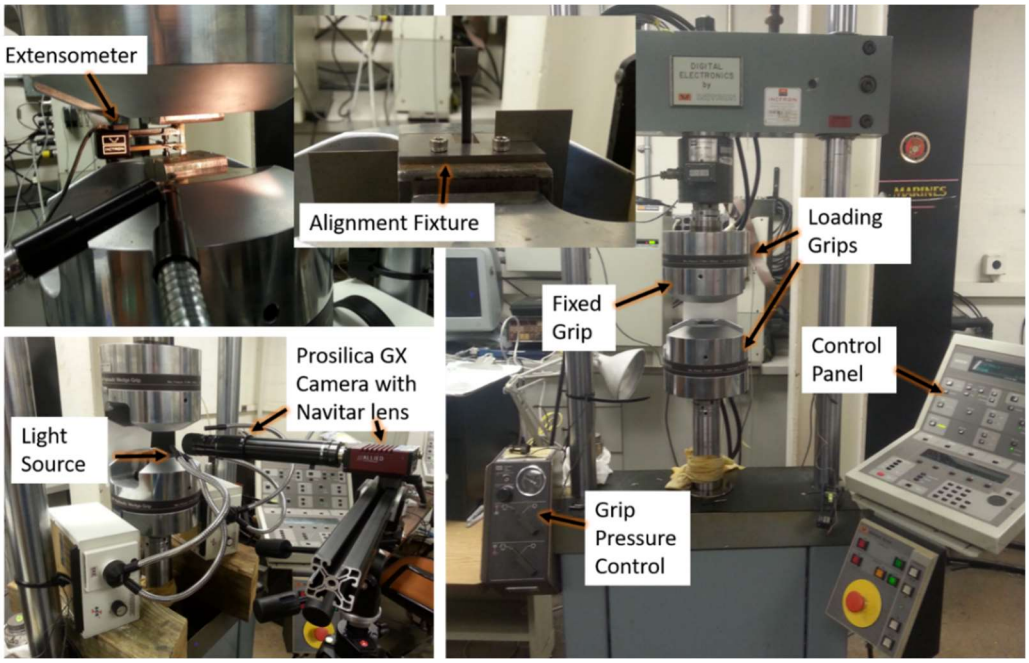

Figure 2.10: Static tension experiments machine setup.

2.2.5 In-Situ Digital Image Correlation

In-situ DIC was performed using a Prosilica camera mounted on a tripod with a Navitar 12X Zoom lens with 2X adapter (see Figure 2.10). The pixel resolution for most in-situ imaging was around 4 μm/pixel although this was specifically measured for each experiment performed. As mentioned above, images were captured at 2 Hz to match the data capturing rate of the measurements from the extensometer and load frame. The start times of both the in-situ image capturing and the Instron machine displacement ramp were synchronized at the start of the test.

During a tension test, which was always run in displacement control at a rate of 0.01 mm/s, the magnitude of the measured displacement, v, in the tension direction, y, should be zero at the fixed end of the Instron machine and at the actuator should be equal to the displacement rate multiplied by the amount of time since the beginning of the test at the grip in motion. The slope of a linear regression fit to a plot of average displacement in the y-direction, v, (tension direction) versus the position in the y-direction away from the fixed end should then equal the strain. To validate the in-situ image correlation displacement measurements, this plot was made from tension test data of the Z30AB-2 sample (see Table 2.1) and shown in Figure 2.11. The slope of the line was measured at 0.0173 at a point where the extensometer measured a strain of 0.0170 showing an agreement within 2%.

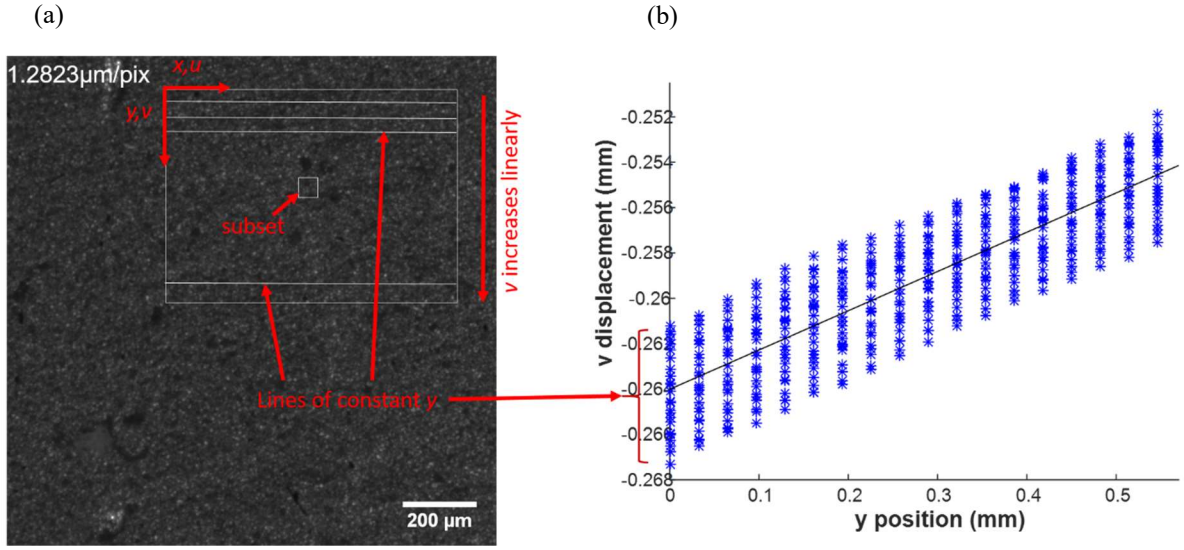

Figure 2.11: (a) Image from tension test of Z30AB-3 sample showing area of interest (large outer box), subset size (small inner box), horizontal lines where displacement data was pulled (these are the vertically aligned points in (b)), and the coordinate system axes. DIC parameters were a subset size of 40x40 pixels and step size of 5 pixels. (b) Plot of the displacement in the y-direction, v vs. the y-position during a static tension test. For visualization purposes, only every fifth y-position is shown as a vertical line of data points, and only every fifth point at that y-position is shown. A linear regression fit was made to all data points with a slope of 0.0173.

While displacements were calculated using VIC-2D 2009 from Correlated Solutions Inc., global strain for a particular image was computed using a straight-line fit to the displacement data for the in-situ measurement and using field displacement gradients for the ex-situ data. In the case

of using field displacement gradients, splines were fit to the data and the gradient at each correlation point was computed and plotted onto a contour plot. Taking the displacement in the *x*-direction to be *u* and the displacement in the *y*-direction to be *v*, the displacement gradient of *u* in the *x*-direction at each point is equal to ε_{xx}, the gradient of *v* in the *y*-direction is ε_{yy} and half the sum of the gradient of *u* in the *y*-direction and the gradient of *v* in the *x*-direction gives the shear strain.

2.2.6 High Magnification Ex-Situ Digital Image Correlation

High magnification ex-situ DIC was performed using the Olympus Q-Color3 camera on an optical microscope. High magnification ex-situ imaging allowed for increased pixel resolution compared to the lower magnification in-situ DIC. High magnification is more easily achieved in ex-situ imaging for two practical reasons. One reason is the reduced depth of focus at higher optical magnifications makes it challenging for in-situ images to remain in focus as a solid is stressed when out of plane deformations become large due to the Poisson effect. Secondly, high magnifications usually necessitate short working distances between the specimen and the lens. Bulky high magnification image capturing systems may not be practical in close proximity to tension test machines in the lab. The disadvantages to high magnification ex-situ DIC are the inability to take images of specimens under applied stress and the reduced field of view in single images. Due to this reduced field of view, several pictures were usually taken and stitched together to cover the area of interest. Two translation stages, one mounted onto another, were placed under the optical microscope and allowed images to be taken in a discrete, grid like fashion. These, along with the optical microscope can be seen in Figure 2.12.

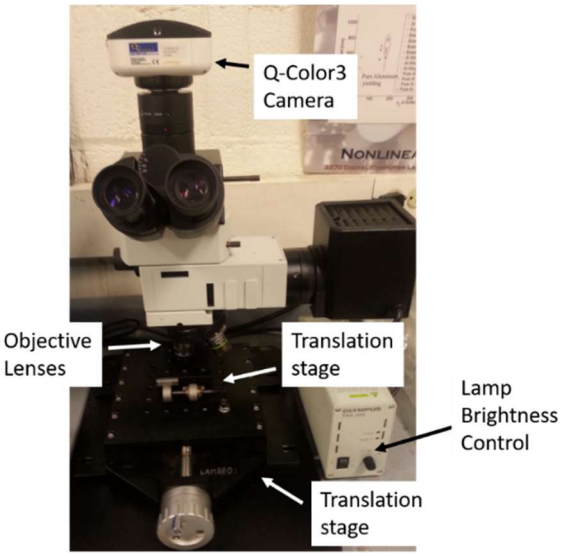

Figure 2.12: Optical Microscope with translation stages and Q-Color3 camera used for ex-situ imaging

Taking pictures in a grid-like fashion and aligning the ex-situ images with the correlated strain fields required the use of fiducial marks on the specimen surface. These fiducial markers must satisfy four important criteria that are explained in more detail in Carroll (2011) in order to ensure successful alignment and useful data. Mainly, the markers must be sufficiently numerous to ensure proper alignment, permanent so location or orientation is not lost, small enough to allow alignment with the desired level of resolution and they must not interfere with the measurement (Carroll, 2011). Micro hardness indentations can be scaled in size based on the applied force to allow for precise alignment with sub-grain level accuracy, remain visible in Electron Backscatter Diffraction (EBSD) and SEM backscattered electron image mode although they form localized compressive stresses in the material localized to the indentation, the relative size of the indentation compared to the area of interest is made small to allow negligible interference. Thus, micro hardness indentations were chosen to outline the area of interest in a pattern similar to that used in Carroll (2011).

The procedure for ex-situ imaging usually went as follows: the specimen of interest was given fiducial markers to assist in alignment. Then, one or more images were taken in a grid-like fashion using the translation stages under the microscope to cover the entire area of interest with about a 60% area overlap between adjacent images. An experiment was then conducted on the specimen. For a standard tension specimen, this meant performing a tension experiment and stopping the test when reaching a plastic strain, usually around 2-3% strain. Finally, images were either stitched together and then correlated as one image or correlated as individual images with their strain contour plots stitched together. Special care was taken to ensure the specimen images were taken with an equivalent light exposure between measurements. This meant avoiding the adjustment of the brightness setting on the microscope light and comparing histograms of images taken in each ex-situ measurement. In addition, maintaining proper optical focus within a single image was critical to ensure correlation between image sets. Thus, the focus was often adjusted as the sample was translated especially for samples with large topology or viewing under high magnification.

Several objective lens magnifications were available for ex-situ imaging including 4X, 20X, and 40X lenses. A 2X built-in objective lens magnifier allowed for additional magnifications of 8X and 80X. For simplicity in understanding the scales used in this work, these magnifications were converted into a distance per pixel measurement shown in Table 2.5. These measurements were made using a 1951 USAF resolution test chart where line thicknesses of known dimensions were measured in pixels and converted into the values shown in Table 2.5. Line thicknesses chosen for a particular resolution measurement were picked such that the thickness took up as much of the field of view as possible. All magnifications in this work are thus referred to by this measurement.

Table 2.5: Magnification Conversion

Magnification	4X	8X	20X	40X	80X
μm/pix	1.7400	0.8711	0.3492	0.1817	0.0967

2.2.7 Digital Image Correlation Parameters

For convenience, parameters for both the in-situ and ex-situ DIC measurements are presented in Table 2.6 and Table 2.7, respectively. Table 2.6 and Table 2.7 include the lenses used for the in-situ or ex-situ measurements, pattern type, resolution in μm/pixel, subset size in pixels, step size in pixels, and number of correlation points for all samples tested in this work. Ex-situ measurements were only made for sample Z30AB-4, thus Table 2.7 only includes DIC parameters for this sample.

Table 2.6: Digital image correlation parameters for in-situ experiments shown in this work. Refer to Table 2.1 for information on the build parameters for each sample.

Sample	lens	pattern type	resolution (μm/pix)	subset (pix)	step (pix)	Area (mm x mm)	correlation points
Z30AB-1	TAMRON	spray paint	12.008	60	30	2.16 x 6.49	133
Z30AB-2	Navitar	airbrush	2.196	40	10	1.10 x 0.97	2295
Z30AB-3	Navitar	airbrush	1.2823	40	5	0.80 x 0.58	11466
Z30AB-4	N/A	N/A	N/A	N/A	N/A	N/A	N/A
Z30HT-1	Navitar	airbrush	4.316	101	50	1.73 x 2.16	99
Z30HT-2	N/A	N/A	N/A	N/A	N/A	N/A	N/A
Z60AB	Navitar	airbrush	4.262	80	40	1.70 x 2.39	165
XY30AB-1	Navitar	airbrush	3.333	80	40	1.87 x 1.87	225
XY30AB-2	N/A	N/A	N/A	N/A	N/A	N/A	N/A
XY60AB	Navitar	airbrush	3.162	60	30	2.47 x 0.95	297
Conventional	N/A	N/A	N/A	N/A	N/A	N/A	N/A

Table 2.7: Digital image correlation parameters for ex-situ experiments shown in this work. Refer to Table 2.1 for information on the build parameters for each sample.

Sample	lens	pattern type	resolution (μm/pix)	subset (pix)	step (pix)	Area (μm x μm)	correlation points
Z30AB-4	40X	silicon powder	0.1817	31	5	808 x 603	614422

2.2.8 Analytical Scanning Electron Microscope Measurements

Microstructural imaging was necessary in order to interpret macro-scale properties and micro-scale behavior of the AM samples used in this work. Much of this microstructural imaging was performed using a scanning electron microscope (SEM), and three SEM imaging techniques are shown throughout this work. In the first imaging technique, a JEOL 6060LV microscope located at UIUC's MRL was used in secondary electron imaging mode to visualize fracture surface features on samples brought to failure during the uniaxial tension experiments at different magnifications. The second technique also involved the JEOL 6060LV microscope at UIUC's MRL using its backscattered electron imaging mode. Using this mode, certain microstructural features such as grain boundaries were made visible and could be mapped to DIC calculated strain fields using the fiducial marker technique described in section 2.2.6. The second imaging technique was called electron backscatter diffraction (EBSD) where grain orientations could be mapped at many points that cover a region of interest. EBSD measurements presented in this work were performed by EBSD Analytical (from Lehi, Utah). Using the mapped grain orientation field, a threshold in the difference of grain orientation between adjacent mapped points can then be defined to determine where grain boundaries lie. This allows for the quantification of grain size over the entire field. Maps of orientation showing grain boundaries can be aligned and overlapped with DIC calculated strain fields, and micro-scale mechanical behavior can be related directly to microstructural features. Preferential grain alignment, called texture, can also be determined using EBSD and related to observed mechanical properties.

Chapter 3: Macro-Scale Study of AM Mechanical Behavior

3.1 Hardness Tests

As mentioned earlier, hardness indentations made for the purpose of creating fiducial markers were created using a 0.3 kgf weight. At the same time, using Equation 2.2, Vickers hardness values were calculated for several samples. Results of the hardness tests sorted by sample type are shown in Table 3.1. Indentations were made on 3 different samples for group Z30AB and one sample each for the remaining groups. The pixel distance measurement of an average diagonal length for one indentation ranged from 99 to 115 pixels corresponding to distances of 33.9 to 39.3μm, respectively.

Table 3.1: Vickers hardness test results in VHN using 0.3kgf weight

Sample	Z30AB	Z30HT	XY30AB	Conventional
Average	439.3	390.6	437.6	386.0
Number of Indentations	13	3	3	3
Standard Deviation	26.3	31.9	10.6	30.4

Two observations are immediately apparent from Table 3.1: hardness values have little to no dependence on build orientation (compare Z30AB and XY30AB) and heat treatment has the effect of material softening with hardness values being comparable to conventionally processed Ti-6Al-4V (compare Z30HT and Conventional). However, it must be stated that while the average hardness of the Z30HT specimen was 11% lower than the average hardness of the Z30AB specimens, the standard deviations for each measurement are quite high as seen in Table 3.1. More information on the mechanical behavior is needed to further assess any possible differences in properties.

The values presented in Table 3.1 agree reasonably well with values seen in the literature for both the magnitude of the hardness measurement and the effect of heat treatment. Measurements for a martensitic laser melted Ti-6Al-4V in Thijs et al. (2010) for instance were around 409HV for the process control optimized sample using a 0.3 kgf weight. Additionally, Kasperovich and Hausmann (2013) saw hardness drops from 360HV to 351HV and 321HV for the two different annealing treatments chosen on the initially martensitic microstructure of laser melted Ti-6Al-4V. This drop in hardness observed in Kasperovich and Hausmann (2013) again agrees reasonably well with the drop seen in Table 3.1.

3.2 Uniaxial Static Tension Experiments

3.2.1 Mechanical Properties

All samples that underwent uniaxial tension tests (listed in Table 2.1) in this work are presented in Table 3.2 and their corresponding stress-strain are curves plotted together in Figure 3.1 for comparison. For the purposes of consistency and completeness of data, strain in Figure 3.1 was taken from the extensometer only, although in many cases DIC measurements were also made. The speckle patterns on some of the high magnification ex-situ measurements were too poor in quality for the lower magnification in-situ measurements. Thus, the extensometer gives more complete information. Samples that possessed the same manufacturing parameters and heat treatment, have been grouped by color in Figure 3.1. Not all samples were loaded to failure as described in section 2.2.4, and those that were taken to failure have an “X” marked on the last data point before the sample ultimately failed.

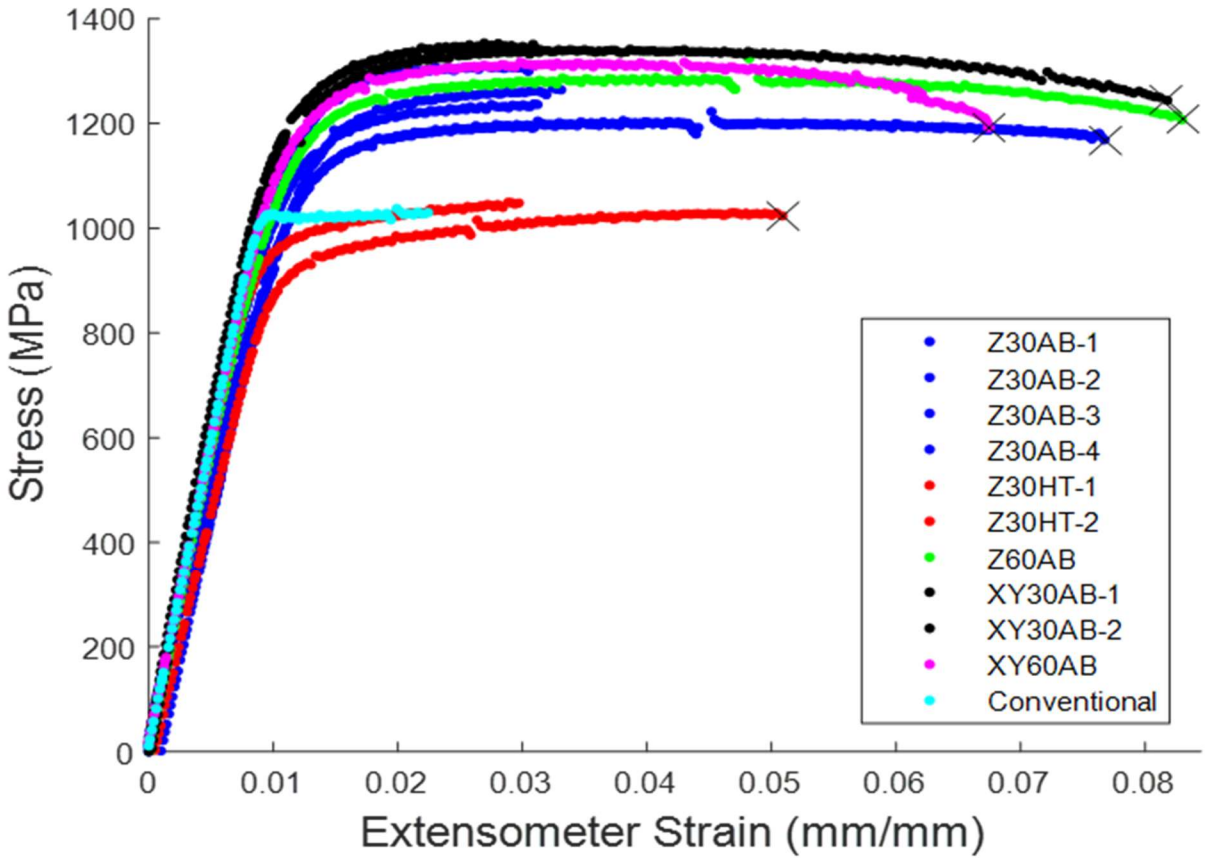

Figure 3.1: Stress-strain plot for all uniaxial tension tests. Strain was pulled from extensometer measurements. See Table 2.1 for more details on the nature of individual samples. Samples of the same type (e.g. Z30AB, Z30HT, etc.) are grouped by color. Specimens taken to failure are distinguished by an "X" located on the last data point before failure.

Stress was plotted against in-situ DIC measured strain as well and shown in Figure 3.2. Some samples included in Figure 3.1 that exhibited poor correlation due to the scale of the pattern are omitted from Figure 3.2. Samples Z60AB and XY30AB had large DIC measured strains as the experiments progressed towards failure even though there was good agreement in strain measured by the extensometer and calculated using DIC in the elastic region of the stress-strain curves. Thus, the strain axis on Figure 3.2 was scaled to cut these large strains out. As mentioned in section 1.1.3, at large strains DIC results can sometimes be poor. In a similar manner to Figure 3.1, samples brought to failure are distinguished with an "X" marked on the last data point.

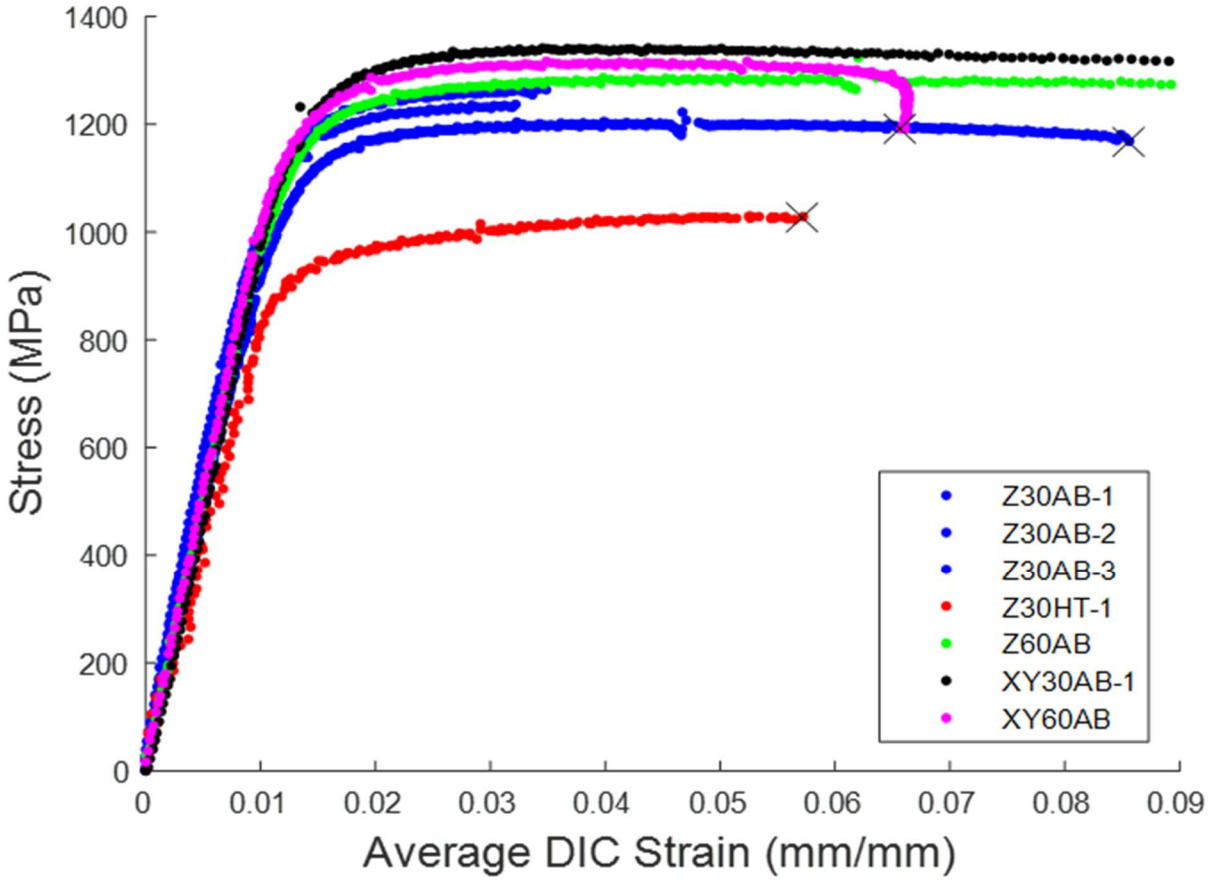

Figure 3.2: Stress-strain plot for all uniaxial tension tests. Strain was pulled from DIC measurements. See Table 2.1 for more details on the nature of individual samples. Samples of the same type (e.g. Z30AB, Z30HT, etc.) are grouped by color. Specimens taken to failure are distinguished by an "X" located on the last data point before failure.

One observation that was made when performing the in-situ DIC measurements was that the average DIC-measured strain (ε_{yy} in the tension direction) followed the extensometer measurement closely until around 2-3% strain was reached when the DIC measurement started to deviate with higher measured strains at each data point as seen in Figure 3.3. This was observed in a case example in Sutton, Orteu and Schreier (2009) and thought to be due to the necking region of the material occupying a much larger portion of space in the area of interest for the DIC measurement than the portion it occupied between the extensometer clamps.

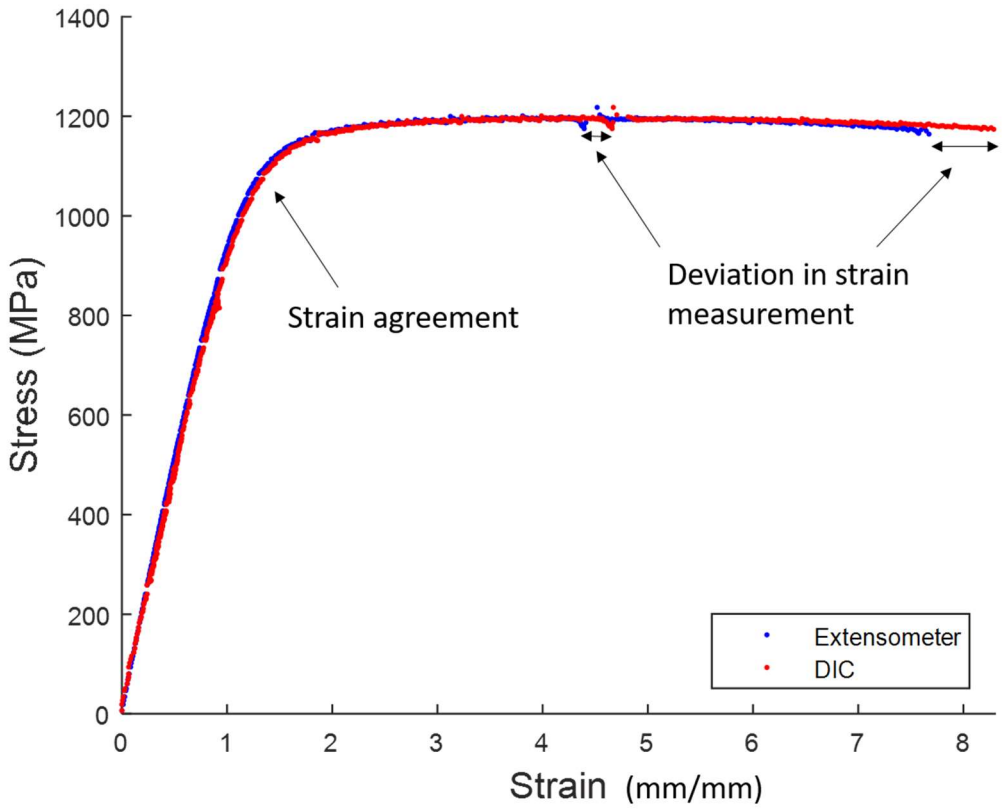

Figure 3.3: Stress strain plot for sample Z30AB-1 showing the deviation in strain measurement around a strain of 0.03mm/mm.

Using the data shown in Figure 3.1, a linear regression fit was made to the stress and strain for each sample from the initial stress to 600MPa (a value less than the lowest yield stress recorded in Table 3.2). The slope of this line was taken to be the elastic modulus of the material, also shown in Table 3.2. Additionally, the slope of a linear regression fit was made to stress and DIC calculated strain (see section 2.2.5 for more details on in-situ DIC strain calculation). For both the extensometer strain measurements and DIC strain calculations, this regression fit was then offset to pass through 0.2% strain (0.002mm/mm) and the intersection between the linear fit and the data for each curve was taken as the yield strength. Ultimate tensile strength (UTS) for each sample was taken as the maximum stress level reached for each sample that was brought to failure. UTS was not calculated for samples that had their tests interrupted for ex-situ measurements. Strain to

failure (ε_f) was calculated in mm/mm using the extensometer measurement since the DIC calculated strain could be highly dependent on the size of the area of interest (see the discussion in section 2.2.5 for more on DIC vs extensometer strain measurements). For sample group types with multiple samples (Z30AB, Z30HT, and XY30AB in Table 3.2), mechanical properties were averaged, and standard deviations have been presented in parenthesis as seen in Table 3.2. Sample group types included Z30AB (consisting of samples Z30AB-1, Z30AB-2, Z30AB-3, and Z30AB-4 from Table 2.1), Z30HT (samples Z30HT-1 and Z30HT-2), Z60AB (sample Z60AB), XY30AB (samples XY30AB-1 and XY30AB-2), XY60AB (sample XY60AB) and Conventional (Conventional sample).

Table 3.2: Mechanical properties of specimens from uniaxial tension experiment. Yield strength and elastic modulus were calculated from extensometer and DIC measurements. In sample group types where data on multiple samples are available, the average value and standard deviation are calculated with the latter defined in parenthesis.

Sample Type	Elastic Modulus Extensometer (GPa)	Elastic Modulus DIC (GPa)	Yield Strength Extensometer (MPa)	Yield Strength DIC (MPa)	Ultimate Tensile Strength (MPa)	Strain to failure (mm/mm)
Z30AB	107.6(5.2)	101.8(8.2)	1094.5(63.7)	1123.0(43.8)	1222.7	0.0767
Z30HT	106.2(9.5)	78.9	936.9(40.9)	927.8	1029.5	0.0509
Z60AB	116.7	100.0	1125.9	1141.7	1323.9	0.0830
XY30AB	113.3(20.9)	97.7	1264.9(81.0)	1221.0	1342.0	0.0763
XY60AB	115.3	101.3	1187.2	1190.5	1317.1	0.0675
Conventional	116.8	N/A	1017.2	N/A	N/A	N/A

For easier visualization of some of the data included in Table 3.2, a bar graph showing the UTS and extensometer measured yield strength and strain to failure (in mm/mm) for each sample group type is shown in Figure 3.4. In this graph, yield strength is averaged in sample groups with multiple samples. Yield strength was calculated from a strain offset of 0.002 from the extensometer data and strain to failure was again calculated using the extensometer strain as described above.

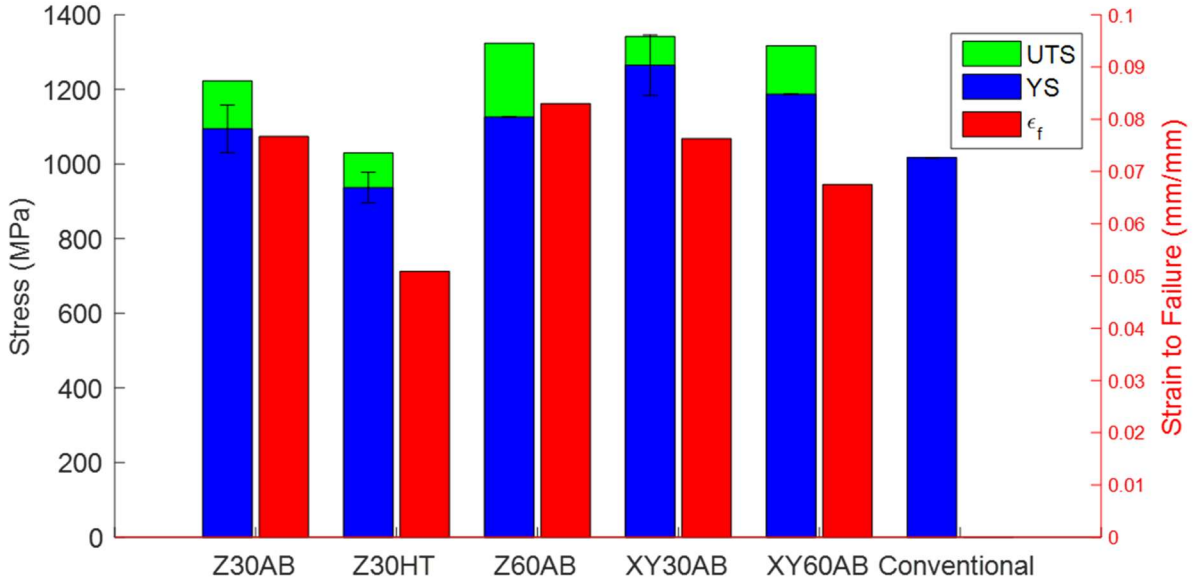

Figure 3.4: Yield strength, UTS, and strain to failure for each sample group. Yield strength and elongation to fracture come from extensometer measurements. In the cases where multiple samples were used, the yield strength is averaged. No UTS or strain to failure values are given for the conventional sample as the conventional sample was not brought to failure. Error bars showing the standard deviation in yield strength are included when applicable.

As a check that the elastic modulus from extensometer and DIC measurements during uniaxial tension tests seems reasonable, the measured elastic moduli presented in Table 3.2 can be compared against the elastic modulus derived from the nondestructive ultrasound experiments the procedure of which is presented in section 2.2.3. Measurements taken from two different samples revealed a calculated elastic modulus of 119.5 GPa for the first sample of length 78 mm and 111.5 GPa for the second sample of length 164 mm, which agree well with the calculated elastic modulus values presented in Table 3.2.

Major observations from Figure 3.1, Figure 3.4, and Table 3.2 that will be discussed in more detail in the following sections include lower yield and ultimate strengths for the Z30HT samples compared to the Z30AB specimens, an increase in yield strength seen in XYZ orientation samples compared to the ZXY orientation, no significant change in mechanical properties for

samples of different layer thicknesses and a wide range in elongation to fracture values between specimens with a particularly low strain to failure seen in the Z30HT-1 sample.

3.2.2 General Comparison to Literature

For comparison purposes, the standard values for the properties of annealed and solution treated and aged (STA) Ti-6Al-4V are given in Table 3.3 as well as typical properties for DMLS Ti-6Al-4V (ASM Aerospace Specification Metals Inc. (a)), (ASM Aerospace Specification Metals Inc. (b)), and (Dutta & Froes, 2016). The properties for annealed Ti-6Al-4V are for a heat treatment temperature of 700-785ºC of unspecified time while the properties for the STA Ti-6Al-4V were for a solution treatment temperature of 900-955ºC with aging at 540ºC for unspecified time (ASM Aerospace Specification Metals Inc. (a)) & (ASM Aerospace Specification Metals Inc. (b)). Properties cited for DMLS Ti-6Al-4V are of the as-built configuration with no form of heat treatment (Dutta & Froes, 2016).

Table 3.3: Typical mechanical properties of conventionally processed as-built, annealed, and DMLS as-built Ti-6Al-4V. Properties for conventionally processed annealed Ti-6Al-4V are from (ASM Aerospace Specification Metals Inc. (a)), STA Ti-6Al-4V from (ASM Aerospace Specification Metals Inc. (b)) and DMLS Ti-6Al-4V from Dutta and Froes (2016).

Material	Yield Strength (MPa)	Ultimate Tensile Strength (MPa)	Strain to failure (mm/mm)
Ti-6Al-4V, Annealed	880	950	0.14
Ti-6Al-4V, STA	1100	1170	0.1
Ti-6Al-4V, DMLS	1125-1140	1210-1240	0.08

Out of the eight non-heat treated AM samples tested, five samples had yield strengths greater than 1100 MPa in both the extensometer and DIC measurements. The average of these eight samples was 1153 MPa for the extensometer measurements and 1188 MPa for the DIC measurements, which are both higher than the solution treated and aged Ti-6Al-4V yield strength as might be expected according to DMLS values from Table 3.3. Additionally, every non-heat

treated sample tested to failure exhibited a higher ultimate tensile strength and lower strain to failure than is quoted for STA Ti-6Al-4V again confirming the higher UTS and lower elongation DMLS Ti-6Al-4V Table 3.3 values. The increased strength and reduced strain to failure is likely due to the highly non-equilibrium martensitic type microstructure that forms as a result of high cooling rates commonly seen in laser sintered AM Ti-6Al-4V (Lewandowski & Seifi, 2016). The characteristic needle-like structure of martensite can be seen in a SEM using backscattered electron imaging composition mode on several of the as-built samples as shown in Figure 3.5.

(a)

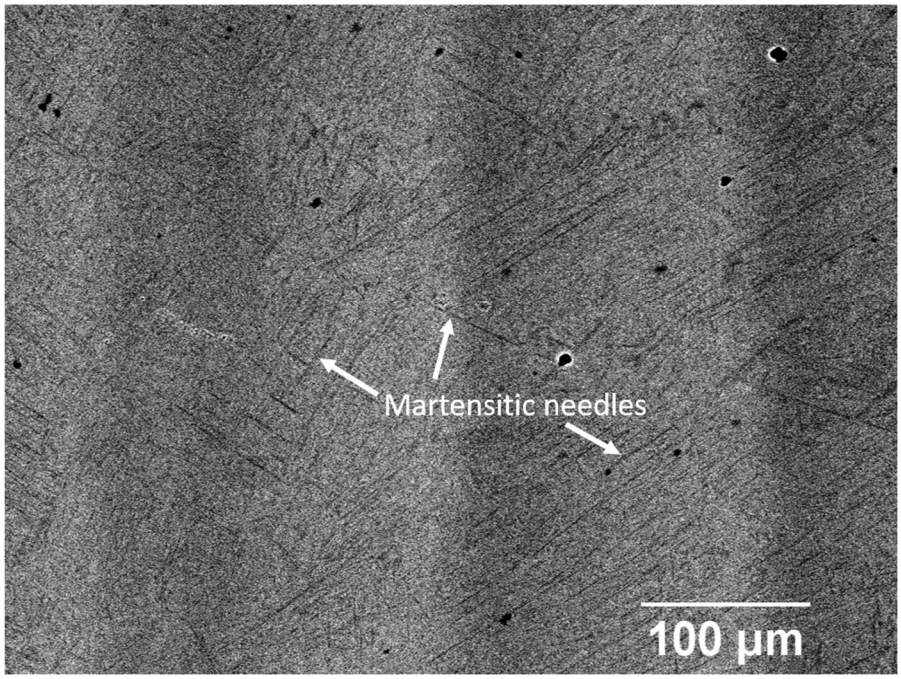

Figure 3.5

(b)

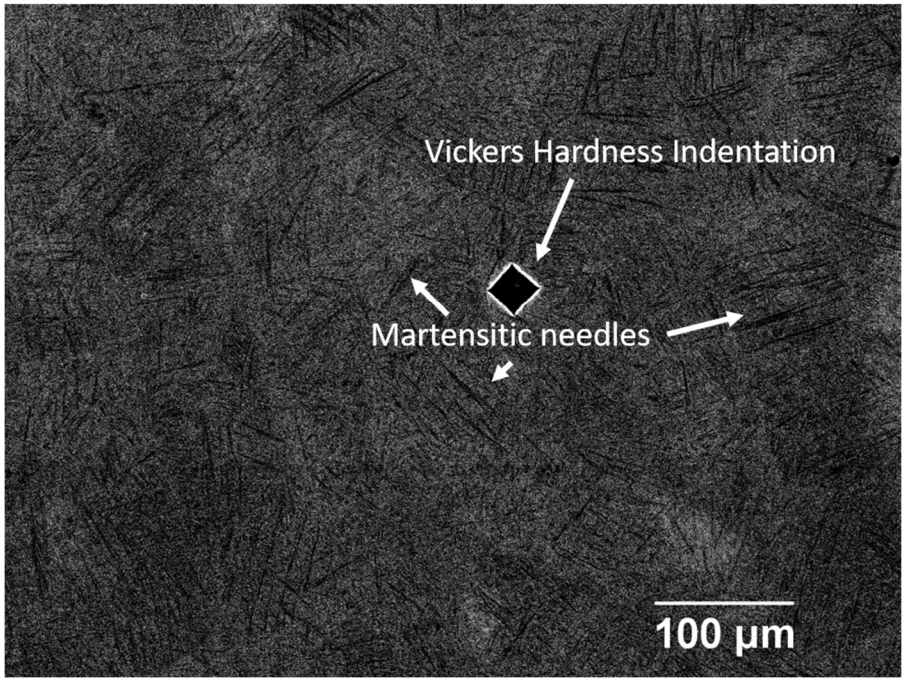

Figure 3.5 (cont.): Characteristic acicular, or needle-like, structure of martensite captured in backscatter electron mode on a JEOL 6060LV SEM for (a) Z60AB sample and (b) XY30AB-2 sample.

As described in Chapter 1, α+β stabilized Ti-6Al-4V can take on one of two characteristic microstructures, bi-modal or lamellar, with preference towards lamellar structures in AM metals. One of the key factors that influences the strength of lamellar structures in α+β type Ti-6Al-4V alloys is the α colony size. The α colony size effectively sets the slip length and the yield strength. The size of α colonies and the α plates that form within α colonies are controlled by both the cooling rate from temperature drops above the β-transus temperature (995ºC for Ti-6Al-4V) and the size of any prior β grain boundaries that the α colonies nucleate within (Lutjering, 1998) and (Vrancken et al., 2012). This prior β grain size sets a maximum on the size of any α colonies formed. The highest strength alloys formed with a Ti-6Al-4V lamellar type structure contain the martensitic-type structure seen in Figure 3.5 where an α colony size is in essence equivalent to a single α′ martensite plate width. Ductility also increases with increasing cooling rate until a

maximum is reached after which a sharp decline is seen in strain to failure at cooling rates higher than 15-20°C/s (Lutjering, 1998). Cooling rates seen in laser sintered AM metals were calculated in excess of 1000°C/s in Islam, Purtonen, Piili, Salminen & Nyrhila (2013) and in Yang, et al. (2016), which exceeds the minimum cooling rate needed for martensite formation (Prabhu et al., 2015).

3.2.3 Effect of Heat Treatment on Strength

One observation that is immediately obvious from Figure 3.1 and Figure 3.4 is the yield strength reduction of the Z30HT samples compared to the Z30AB samples. Table 3.2 confirms this in both the extensometer and DIC measurements where both measurements show lower yield strengths in the Z30HT samples that are significantly outside the range of the standard deviations (shown in parenthesis in Table 3.2) for both the Z30AB and Z30HT samples. The Z30HT sample shows slightly lower yield strength compared to the conventional sample and slightly greater yield strength than shown in Table 3.3 for annealed conventional Ti-6Al-4V. The average yield strength from the extensometer of 937 MPa was close to the 909 MPa seen in Vrancken et al. (2012) for a very similar heat treatment to the one used here. Also, after yielding the strain hardening rate of the conventional sample was somewhat lower as seen in Figure 3.1 where the curve flattens out as compared to the smoother transition from the elastic to plastic regions of the stress strain curve in the Z30HT samples. This was also observed in a bimodal structured conventionally processed Ti-6Al-4V alloy in Facchini et al. (2010). Although it is unknown what the microstructure is for the annealed conventional Ti-6Al-4V in Table 3.3, the microstructures of the Z30HT samples and conventional sample used in this work can be compared using SEM backscattered electron composition mode generated images seen in Figure 3.6.

(a)

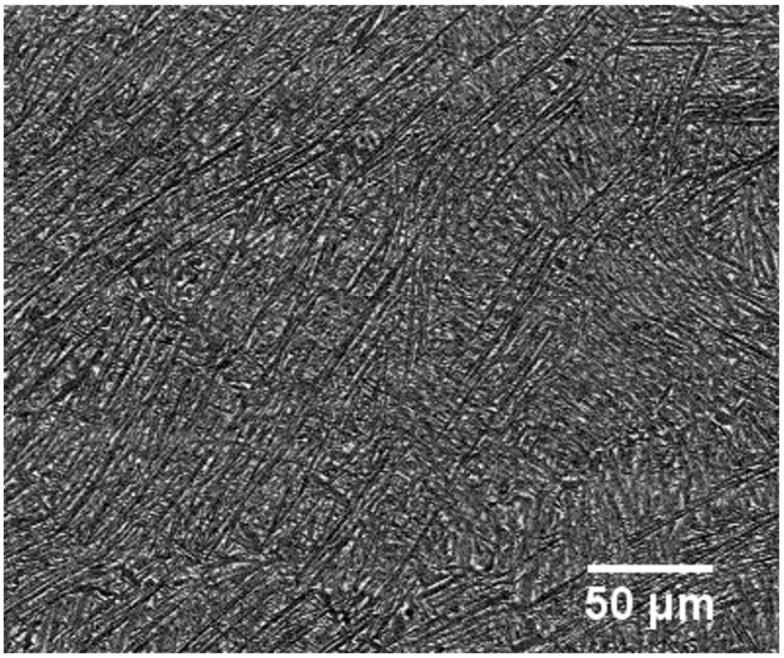

(b)

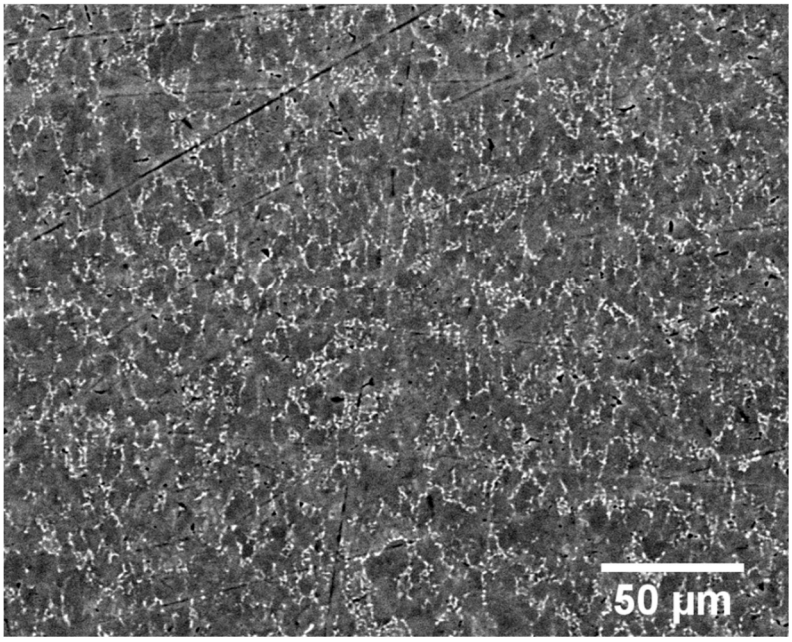

Figure 3.6: Backscattered electron imaging mode of JEOL 6060LV SEM capturing structure of (a) Z30HT-2 sample and (b) conventional sample used in this work. Note the lamellar α phase structure in (a) where large regions of plates (seen as the dark lines) in close proximity are similarly oriented. This is in contrast to the overlapping alternating plate structure believed to be martensite seen in Figure 3.5. The structure of the conventional sample in (b) appears to be bimodal in nature with distinct phase separation of α phase (dark globular regions) and β phase (light regions).

Figure 3.6 shows that the microstructure differs substantially between the Z30HT samples (Figure 3.6(a)) and the conventionally processed samples (Figure 3.6(b)). In Figure 3.6(a) a lamellar type structure is seen whereas a bimodal type structure is seen in Figure 3.6(b). A clear difference can be seen between the overlapping alternating plate structure for both samples in Figure 3.5 and the large regions of similarly oriented α phase lamellae in Figure 3.6(a). In the bimodal structure depicted in Figure 3.6(b) the darker globular regions correspond to α phase whereas the lighter regions filling in the gaps are believed to be β phase based on comparisons to Facchini, et al. (2010). A lamellar α+β structure is seen in the Z30HT sample because a bimodal structure can only be achieved through hot working in addition to an annealing heat treatment (Facchini, et al., 2010). The heat treatment of the Z30HT samples was chosen such that the temperature of 850°C was below the β transus temperature of 995°C to allow the breakdown of α′ martensite and coarsening of α plates and colony sizes without influencing any prior β phase (Vrancken et al., 2012). Coarsening of α colony size is most likely the driving factor for the reduction in yield strength in the Z30HT samples as compared to the Z30AB samples.

3.2.4 Effect of Orientation on Strength

XYZ oriented samples (sample groups XY30AB and XY60AB) have a higher yield strength than ZXY oriented samples (sample groups Z30AB and Z60AB). This is seen in Table 3.2 for both extensometer and DIC measurements of yield strength. Greater yield strength seen in the XYZ orientation as compared to the ZXY orientation is also seen in tension experiments on AM Ti-6Al-4V in Rafi, Starr, & Stucker (2013), Brandl, Baufield, Leyens, & Gault (2010), and Baufield, Van der Biest, & Gault (2010). Although previous work has ascribed anisotropy of static tensile properties to several possible attributes including lack of fusion defects or microstructural features, it appears there is still debate on this topic. Recent studies on part density show most

modern AM metals can be built to densities matching conventionally processed metals given the correct input scanning parameters (Gong, et al., 2015). Lack of fusion on large scales that can be anisotropic in nature is typically avoided using modern AM techniques making the case that anisotropic properties due these types of defects of little significance (Qiu, Adkins, & Attallah, 2013). Because of this, any anisotropy in mechanical properties may be attributed to microstructural features, of which there are many explanations available in literature. Carroll et al. (2015) proposes an explanation for anisotropic strain to failure that suggests that the presence of α phase along prior β grain boundaries allows for preferential slip and void nucleation in shape metal deposition (SMD) manufactured parts. Because of this and the fact that grain boundaries are longer and more continuous in the build direction due to their columnar nature, Carroll et al.'s (2015) work suggests that samples with tension applied transverse to the build direction can suffer from reduced strain at failure. Indeed, void nucleation is often seen at interfaces where grain boundary α phase is present in lamellar Ti-6Al-4V structures (Banerjee & Williams, 2013). Another possible explanation attributes anisotropic tensile strength to microstructural discontinuities and void nucleation. The explanation goes as follows. As a layer is melted onto previously solidified layers and columnar β grains form at high temperature before solidifying to α phase as explained in more detail in section 1.1.2, the new layer solidifies with a potentially different orientation of α phase than is on the prior layer creating a microstructural interface of discontinuity. Aligning the tension axis in the normal direction to the discontinuity (i.e., tension axis aligned with the build direction) causes the site of the discontinuity to be a concentration area for void nucleation and coalescence (Rafi et al., 2013). Since α grains are highly anisotropic in titanium α+β alloys, misalignments can cause stress discontinuities at sites of grain structure discontinuity. Indeed, elastic discontinuities are often the site of microvoid formation in these types of alloys (Banerjee & Williams, 2013).

The term discontinuity is important here. Whether it originates exactly from this misorientation of α grains or some other effect associated with the complex thermal history of AM parts is less important on the discussion of anisotropy of AM metals than the discontinuity's presence and its repeating directional orientation. Microstructural discontinuities may be seen optically or using an SEM in the form of layer bands described later in Chapter 4. An image of these layer bands is presented here in Figure 3.7.

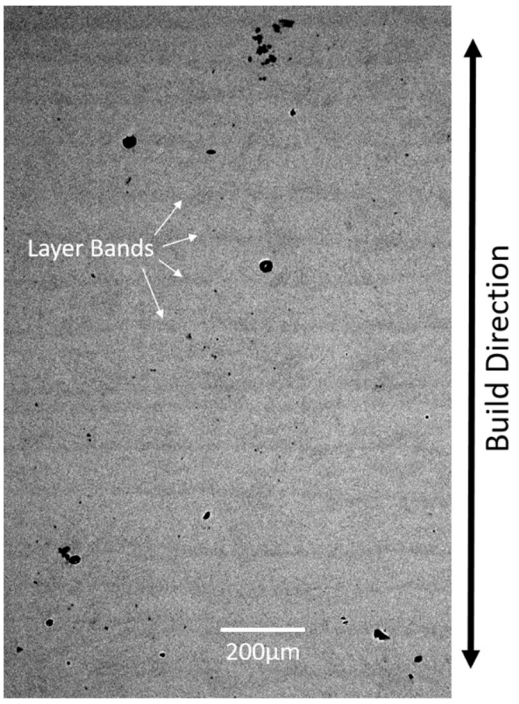

Figure 3.7: SEM backscattered electron image showing layer bands on sample Z30AB-4 that may be visible microstructural discontinuities. See section 4.1.2 for more information on the characteristics and possible origins of these bands.

3.2.5 Effect of Layer Thickness

Comparing the influence of the build layer size (thickness) on the tensile properties, the yield strength and elongation to fracture are larger for the Z60AB sample (i.e., 60 µm build layer) compared to the Z30AB sample (i.e. 30µm build layer). With respect to layer thickness this observation is inverted as these properties are smaller for the XY60AB as compared to the

XY30AB sample. However, yield strength values of the 60 μm build layer samples fall well within the standard deviation of the 30 μm samples, and thus, no clear dependence on build layer size is seen. This may result from the fact that the laser scanning input energy density used in the DMLM process, an important parameter in determining the resultant microstructure, is usually kept constant regardless of layer thickness to ensure consistent part density and mechanical properties. Input energy density, calculated from Equation 1.1, is dependent on the laser power, hatch spacing, layer thickness and scanning velocity. When a single parameter such as layer thickness is changed, another parameter is usually adjusted to compensate and keep energy density consistent. Although the actual scanning parameters for the samples used in this work are unknown, this is a common practice in AM builds. One feature that does change microstructurally with change in layer thickness is the prior β grain size (Xu, et al., 2015). However, as mentioned earlier, the part strength is mostly controlled by the α colony size, or in the case of martensitic microstructure, the α′ lath width (Lutjering, 1998). α′ lath width in AM parts is usually very small and thus not restricted by the size of prior β grain boundaries (Xu, et al., 2015) & (Lutjering, 1998).

3.2.6 Ductility and Failure

There is quite a significant spread in strain to failure among all samples with the Z60AB sample showing the largest strain to failure, followed by the XY30AB-1, Z30AB-1, XY60AB, and Z30HT-1 samples in that order (Table 3.2). The drop in strain to failure in the Z60AB sample to the Z30HT-1 sample is 0.0321, which is a decrease of 39%. All as-built samples failed at typical elongation levels seen in DMLS Ti-6Al-4V with the largest deviation from the "typical" 0.08 value given in Table 3.3 being the 0.0675 seen in the XY60AB sample. AM Ti-6Al-4V metals typically suffer from lower ductility as compared to conventionally processed Ti-6Al-4V due to the martensitic microstructure and potentially large residual stresses (Vrancken et al., 2012) and

(Facchini, et al., 2010). Most literature shows annealing type heat treatments improve ductility in AM samples. Vrancken et al. (2012), Facchini et al. (2010), and Simonelli et al. (2014) all show improvements in ductility for several types of heat treatments of laser melted Ti-6Al-4V. Facchini et al. (2010) suggests that the relief of residual stresses is largely responsible for the improved ductility seen in that work. This was observed in Facchini et al.'s (2010) work when laser melted Ti-6Al-4V samples underwent heat treatments that removed observed microcracks (more on these microcracks later) while maintaining the martensitic microstructure and showed greatly improved ductility in the uniaxial tension experiments. However, improved ductility from heat treatment was not seen in the Z30HT-1 sample brought to failure in this work. In fact, the ductility of the Z30HT-1 sample was by far the lowest ductility seen out of the tested samples. To understand this behavior and the typical fracture behavior of AM samples, the fracture surfaces of three samples were viewed under a JEOL 6060LV SEM.

Figure 3.8 shows the fracture surfaces for sample Z30AB-1(a), Z30HT-1(b), and XY30AB-1(c). From Figure 3.8 it appears that the fracture surface of the Z30HT-1 has a larger region of high roughness than the Z30AB-1 sample or the XY30AB-1 sample. In addition, there are several more imperfections on the fracture surface as pointed out by the red arrows in Figure 3.8. Some of these imperfections are shown in more detail in Figure 3.9. This observation could explain why the Z30HT-1 specimen failed with lower elongation to fracture. Testing more than this one sample may provide better statistical results.

(a)

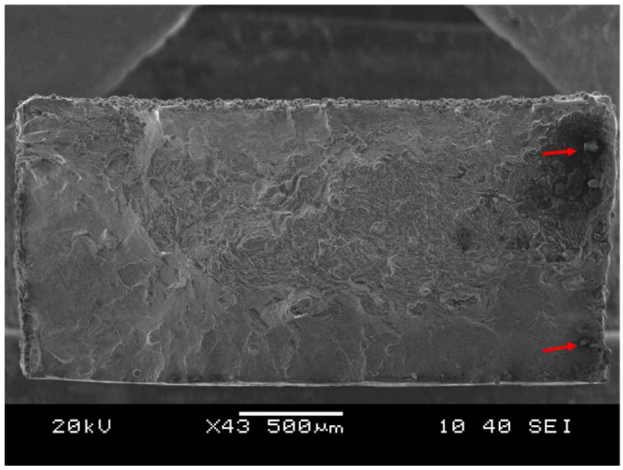

(b)

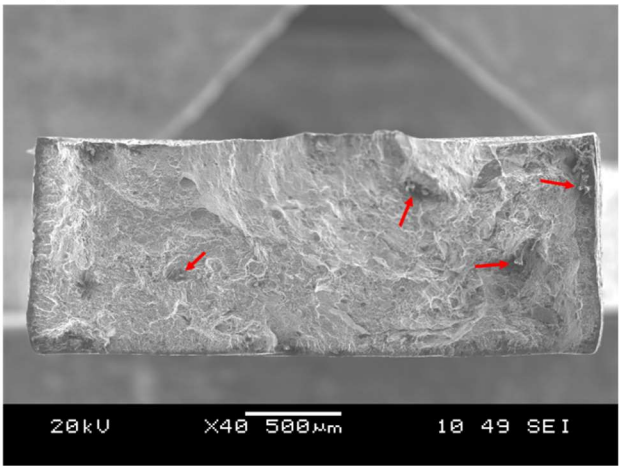

(c)

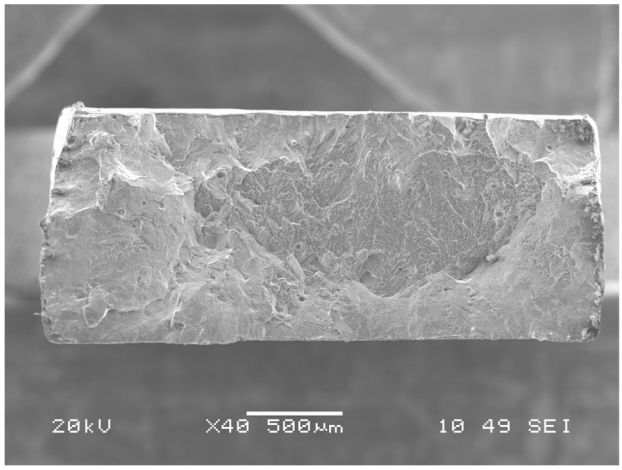

Figure 3.8: SEM secondary electron images of fracture surfaces of specimen Z30AB-1 (a), Z30HT-1 (b), and XY30AB-1 (c). Obvious manufacturing imperfections are indicated with red arrows.

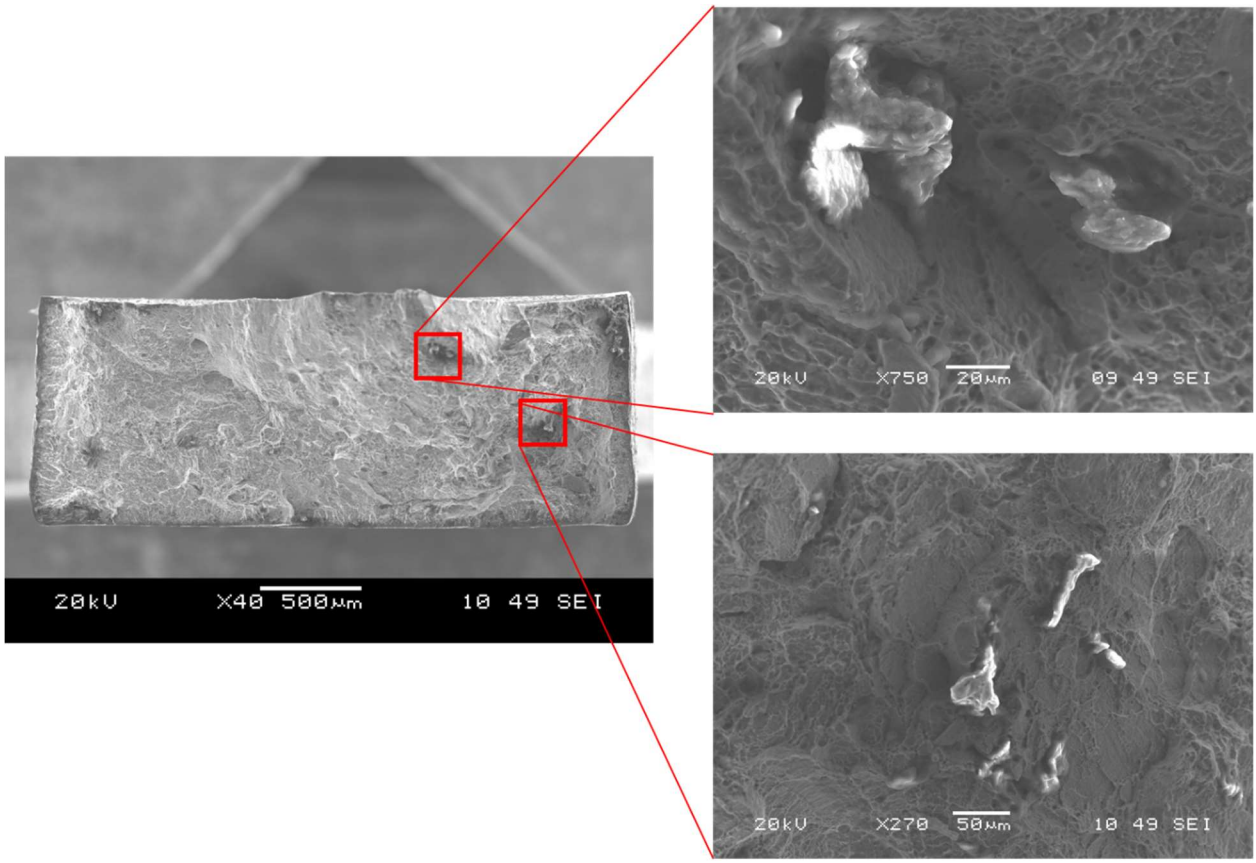

Figure 3.9: Secondary electron images of imperfections on the fracture surface of the Z30HT-1 specimen at higher magnification.

There are other notable features seen on the fracture surfaces that also agree with existing literature on laser melted Ti-6Al-4V. Figure 3.10(a) shows several pores on the surface of the Z30HT-1 sample that are roughly the size of powder particles indicating incomplete melting of a particle (Simonelli, Tse, & Tuck, 2014). Figure 3.10(b) shows a close up of a single such pore with the unmelted powder particle having fallen out. Surrounding this large defect pore are numerous microvoids at higher magnification on the XY30AB-1 specimen, which are typical of the void nucleation-growth-coalescence failure mechanism in ductile materials, including conventional Ti-6Al-4V.

(a) (b)

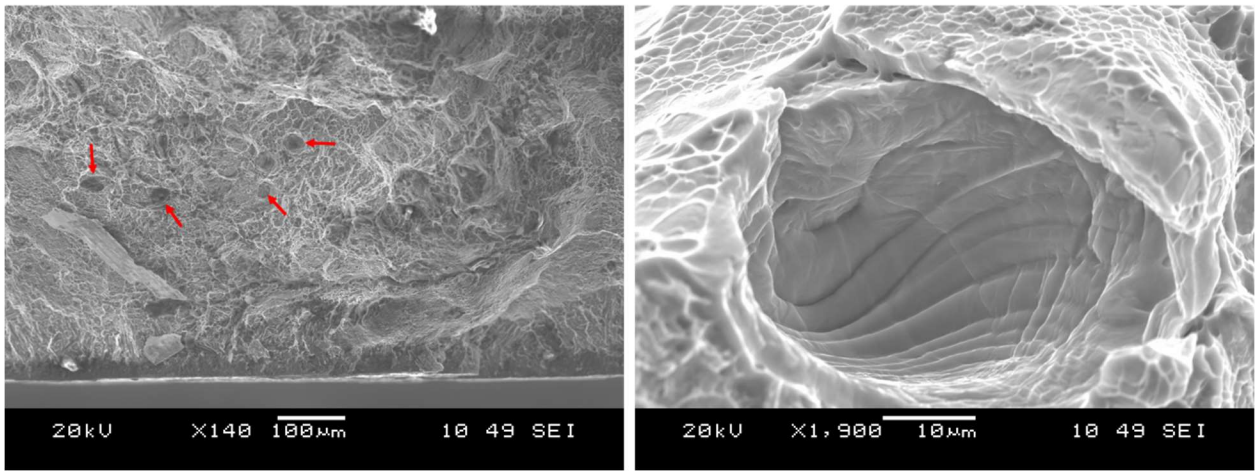

Figure 3.10: Porosity of present on the fracture surface of Z30HT-1 (a) and XY30AB-1 (b) due to incomplete melting as seen in secondary electron images from an SEM. Pores are indicated by red arrows in (a). Note the size of the pore is roughly equivalent to the powder size of 30µm. In (b) the relative scale of microvoids can be compared to that of the pores.

Terraced features shown on the fracture surface of XY30AB-1 in Figure 3.11 were also seen in Simonelli et al. (2014). They were attributed to regions of intergranular failure where crack propagation occurred across prior β grains along the α phase grain boundaries (Simonelli et al., 2014). Note the regions of voiding across the terrace faces indicating potentially large deformation.

(a) (b)

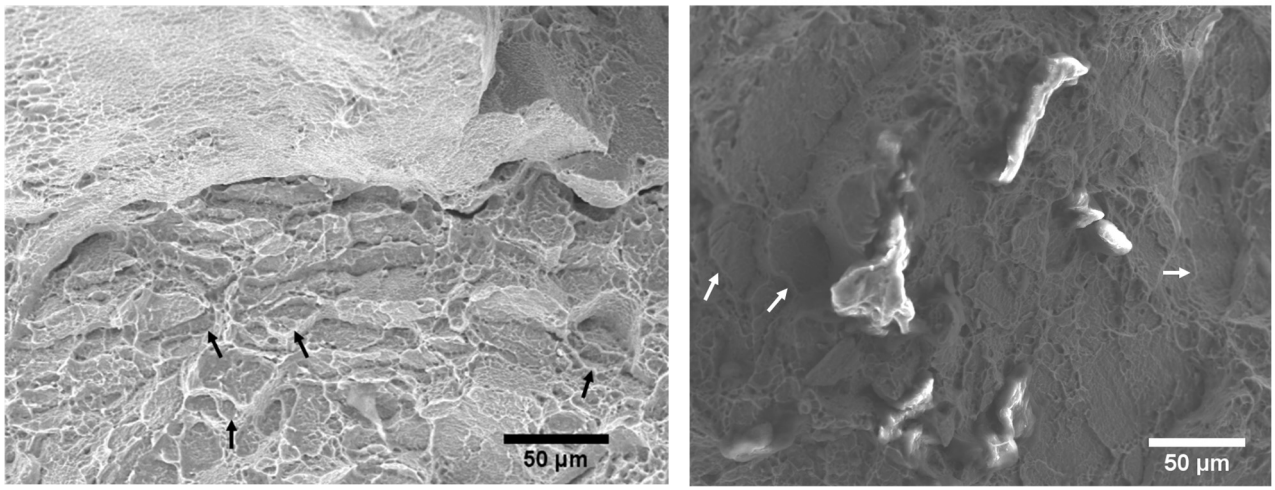

Figure 3.11

(c)

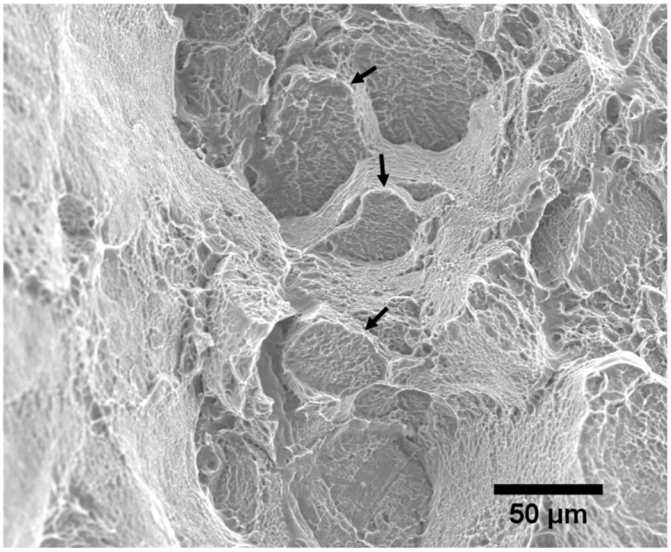

Figure 3.11 (cont.): Terrace-like features on the fracture surface of the Z30AB-1 (a), Z30HT-1 (b), and XY30AB-1 (c) samples as viewed in secondary electron imaging mode on the SEM. These features were noted in Simonelli et al. (2014) and attributed to intergranular fracture.

Cracks were noticed in various regions of the fracture surface as well on the Z30AB-1, Z30HT-1, and XY30AB-1 samples. These are shown in Figure 3.12.

(a)

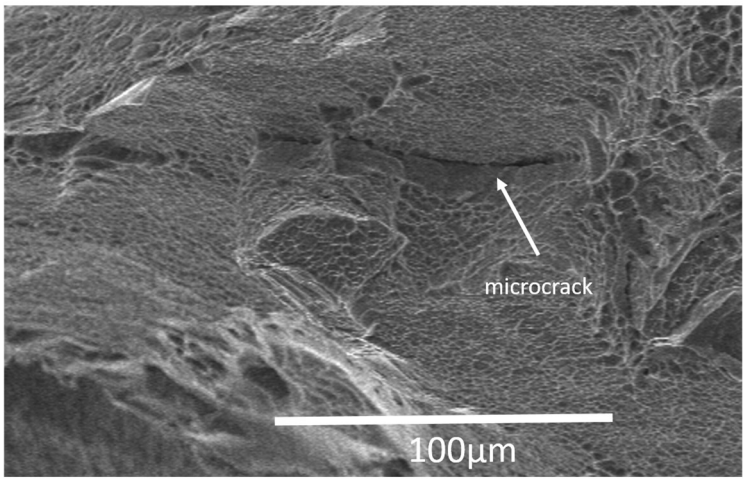

Figure 3.12

(b)

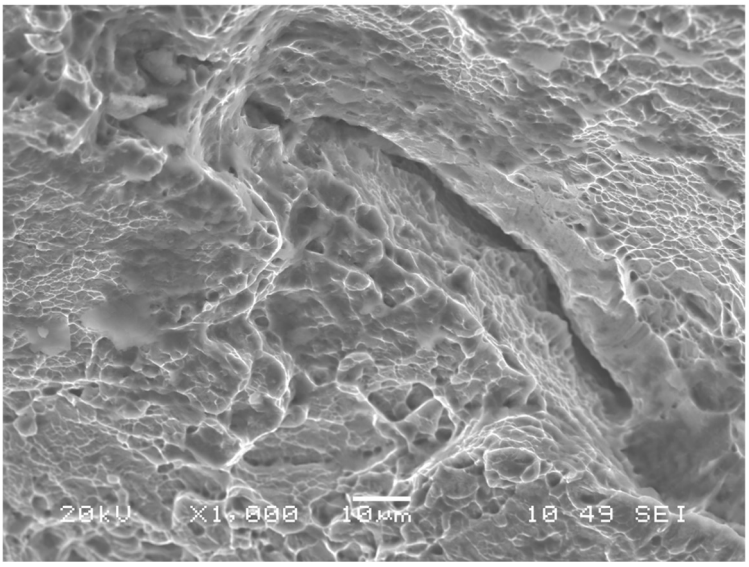

(c)

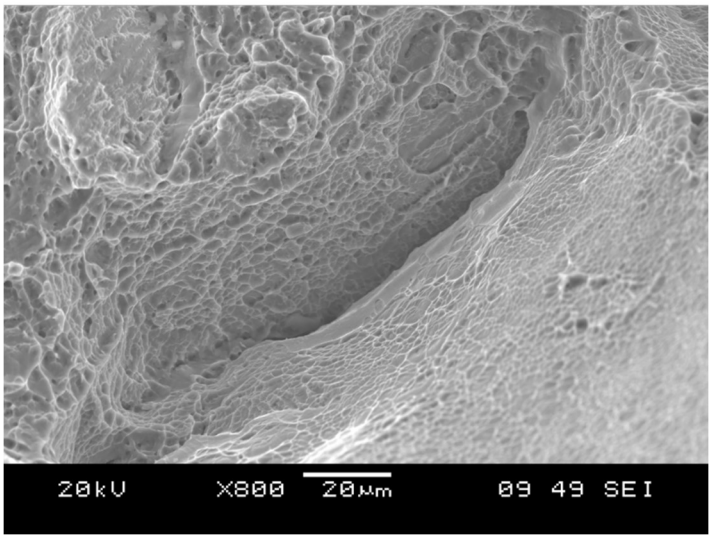

Figure 3.12 (cont.): Secondary electron images of cracks observed on the fracture surface of the Z30AB-1 (a), Z30HT-1 (b), and XY30AB-1 (c) samples.

The cracks in Figure 3.12 are similar in appearance and size to microcracks noted in laser melted Ti-6Al-4V presented in Facchini et al. (2010) that were thought to be due to incomplete homologous wetting between layer interfaces as described in Das (2003). Homologous wetting here refers to the wetting of the surface of previously solidified material with newly melted

material of the same composition as is seen in laser melted AM builds (Das, 2003). Incomplete homologous wetting usually produces microcracks at interfaces where newly melted material incompletely wets the surface of previously solidified material as is seen at layer interfaces in Das (2003). A potential solution to this would be to increase the input energy density of the laser during scanning to partially re-melt previously solidified layers (Das, 2003). The cracks seen in Facchini et al. (2010), though few in number, were clearly seen in optical microscope images to align directly with layer interfaces of subsequently deposited layers during the AM build process. However, microcracks were not seen to align with potential layer interfaces in the fractured samples presented in this section as the crack planes appear to run parallel with the build direction and skewed in orientation with respect to the edges of the fracture surfaces in many cases across the fracture surfaces of the Z30AB-1, Z30HT-1, and XY30AB-1 samples. To visualize this more clearly, the fracture surface images from Figure 3.12 are oriented with respect to the build direction and presented in Figure 3.13 where the AM build coordinate system, the build direction, and direction of applied tension during the uniaxial tension test are shown. Although crack surface normal vectors are not shown in Figure 3.13, they would lie roughly within the *xy*-plane and perpendicular to the proposed laser scan raster direction shown as red arrows in Figure 3.13. Even though these microcracks seen in Figure 3.13 do not line up with potential layer interfaces likely due to partial remelting of previously solidified layers during the AM build as suggested in Das (2003), it is quite possible that incomplete homologous wetting can occur within a build plane as a laser scan raster path melts powder material in a line alongside solidified material along adjacent previous raster paths. The exact raster pattern is unknown for the samples used in this work, however, proposed adjacent laser raster scan path arrows are shown in Figure 3.13 to visualize the possible incomplete homologous wetting between adjacent scan paths. This rastering (represented

as red arrows in Figure 3.13) occurs within the *xy*-plane and may be skewed with respect to the *x* or *y* axes as is typical for AM builds (Thijs et al., 2010). What is proposed in this present work is that the observed microcracks in the present samples form due to incomplete wetting of the surface of previously solidified material by an advancing melt pool along the next adjacent laser scan raster path within the same layer of the build (hence the chosen directions of the raster scan arrows in red with respect to the microcrack alignment). In fact, the microcrack pictured in Figure 3.13 for the XY30AB-1 sample shows a height of about 45µm in the build direction, which is comparable to the 30µm build layer thickness and possible depth of the melt pool. This combined with the fact that these microcracks are observed to align perpendicular to the *xy*-plane remains consistent with the proposed hypothesis that these cracks are confined to the same build layer. In terms of anisotropy, it may be expected that since these microcracks have preferential orientation, there might be an inherent anisotropy to them. However, since the rastering direction is often rotated with each layer, the microcrack alignment may also differ from layer to layer resulting in no inherent anisotropy.

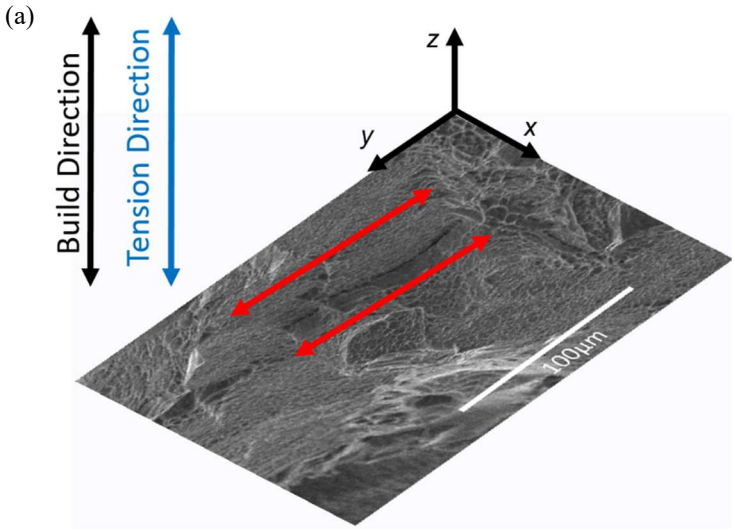

Figure 3.13

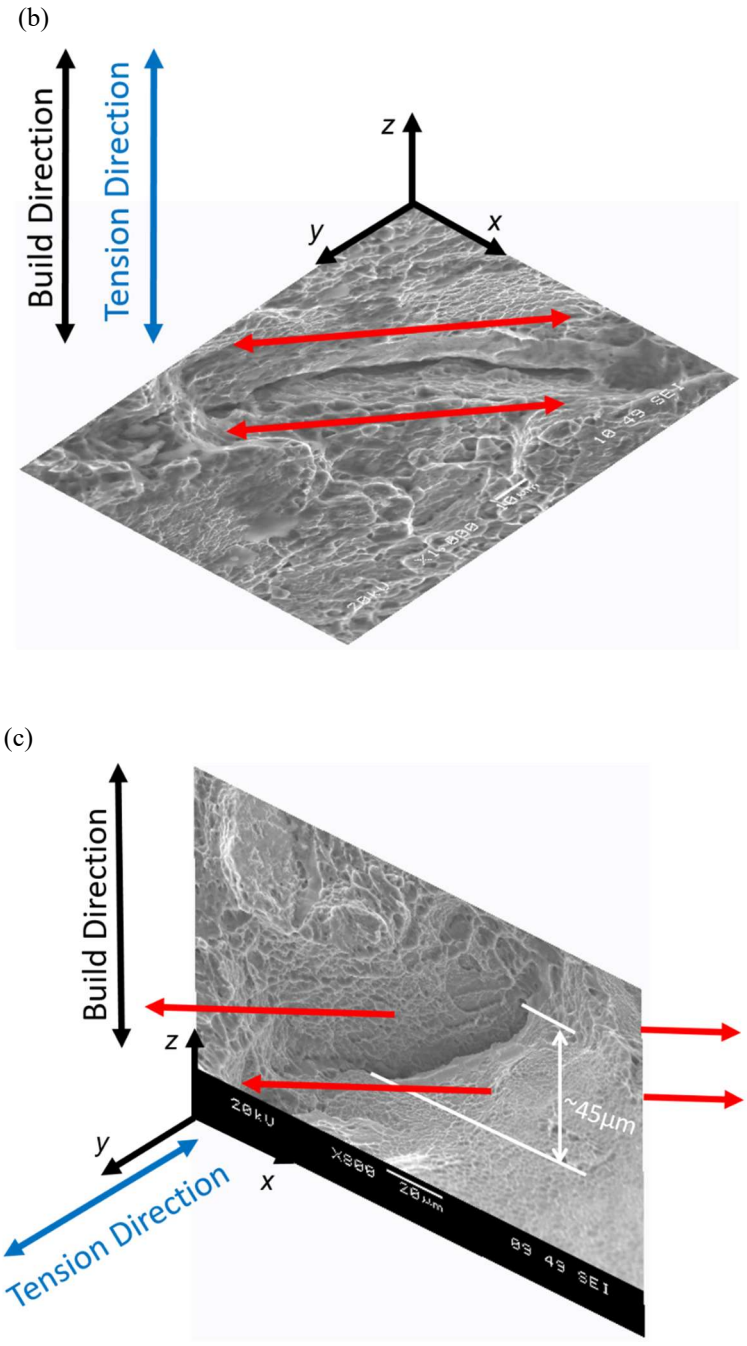

Figure 3.13 (cont.): Images of microcracks seen in samples Z30AB-1 (a), Z30HT-1 (b), and XY30AB-1 (c) from Figure 3.12 oriented with respect to an AM build coordinate system. The build direction is labelled and aligned with the *z*-axis and the direction of applied tension is shown in the double arrows seen in blue. The red double arrows indicate the proposed paths of adjacent laser raster scans.

Another important observation seen from the images in Figure 3.12 is that ductile microvoids similar to those seen in Figure 3.10 are present around the microcrack but vanish at

distances very near to the crack. In Facchini et al. (2010), the lack of ductile features near the microcracks are suggested to indicate the poor work hardenability of the material, and the presence of these microcracks are thought to possibly contribute to the lower ductility seen in AM parts. As poor ductility as well as microcracks were observed in the parts presented in this work, it seems reasonable that a similar relationship can be seen here.

Chapter 4: Micro-Scale Study of Material and Mechanical Behavior

4.1 Additively Manufactured Ti-6Al-4V Structure

4.1.1 Electron Backscatter Diffraction Analysis

As mentioned earlier, an electron backscatter diffraction (EBSD) analysis was performed on two of the samples procured, meant to be representative of the material in general. These two samples were one each of the Z30AB and Z60AB configurations. Color coded grain orientation maps for both samples are presented in Figure 4.1. Contour pole figures and inverse pole figures for the samples are seen in Figure 4.2 and grain size histograms for both samples are presented in Figure 4.3. The data for these figures were provided by EBSD Analytical located in Lehi, Utah. The area of the scan in the orientation maps was marked out using fiducial markers and measured about 1000x1000 μm in size. The step size used was 0.5 μm, which yielded over 4 million data points for each map. Dark areas in the grain orientation maps indicate areas where the diffraction patterns were too weak to be indexed with a high degree of confidence. Decreasing the step size may have reduced the total area of unindexed points at the cost of increased scanning time unless the area of the scan is reduced. Therefore, it is recommended for future work to choose both a smaller area to scan as well as a smaller step size to do just this.

(a)

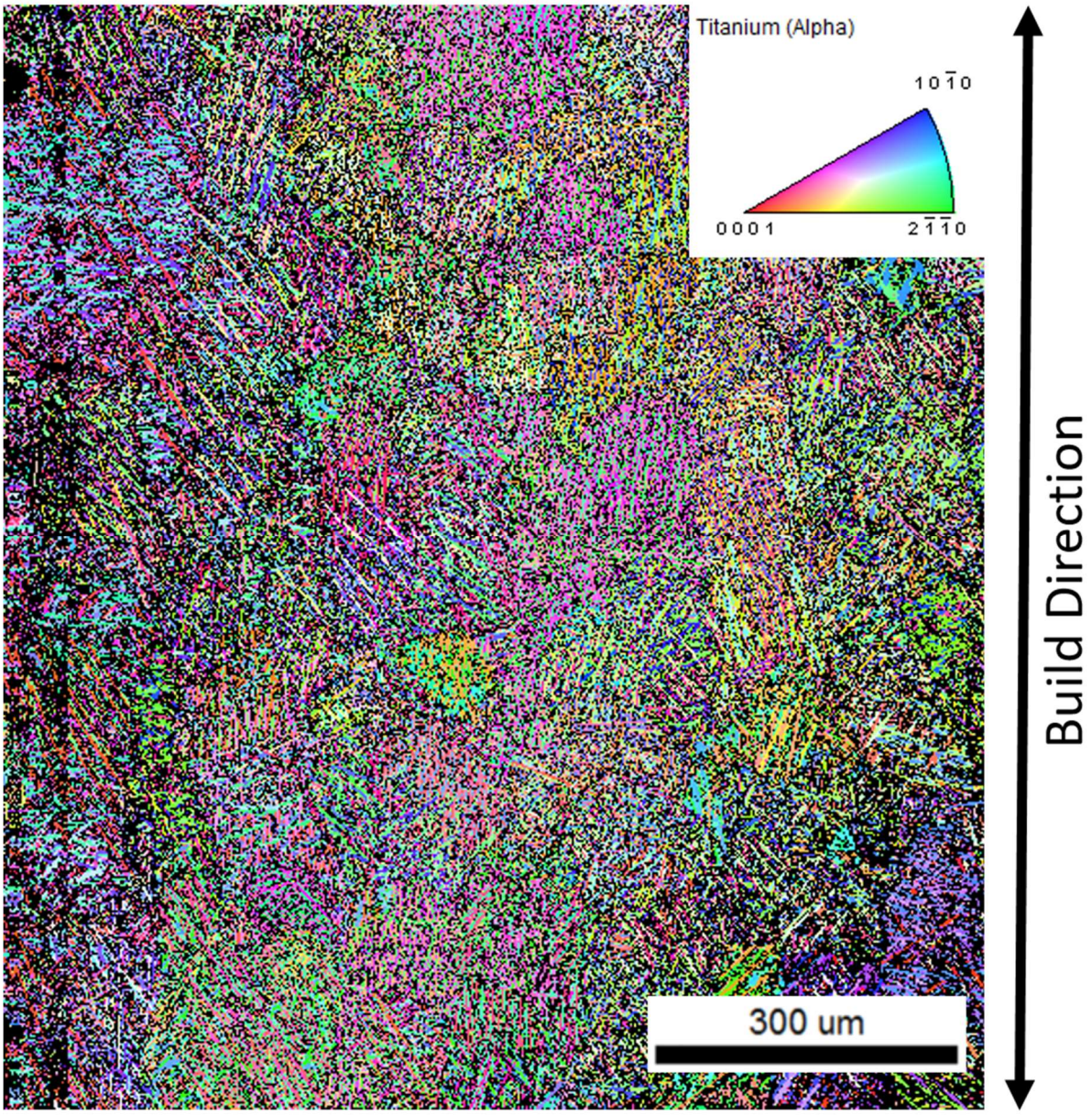
Titanium (Alpha)
$10\bar{1}0$
0001
$2\bar{1}\bar{1}0$
300 um
Build Direction

Figure 4.1

(b)

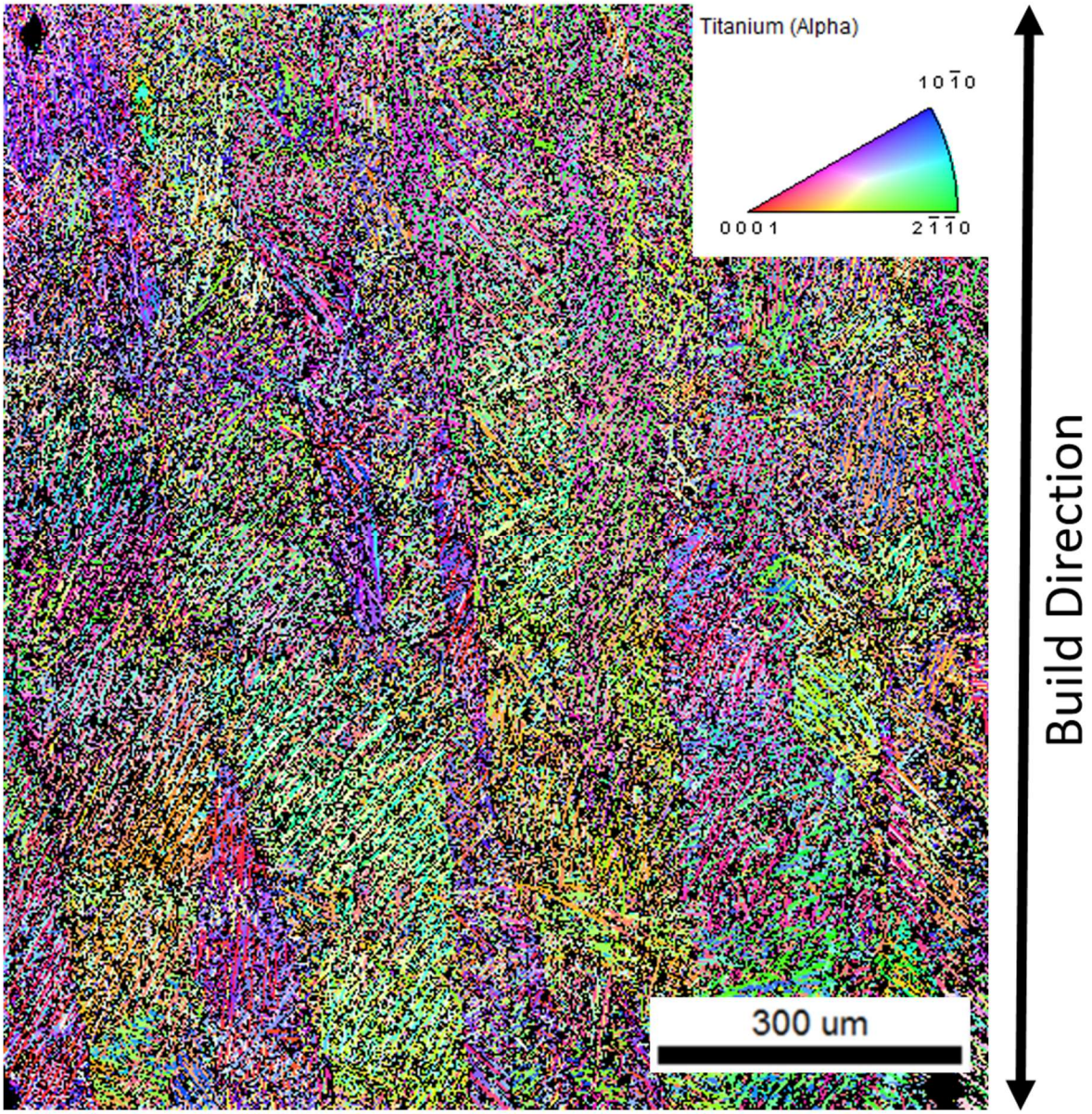

Figure 4.1 (cont.): Color coded orientation maps for representative samples Z30AB (a) and Z60AB (b).

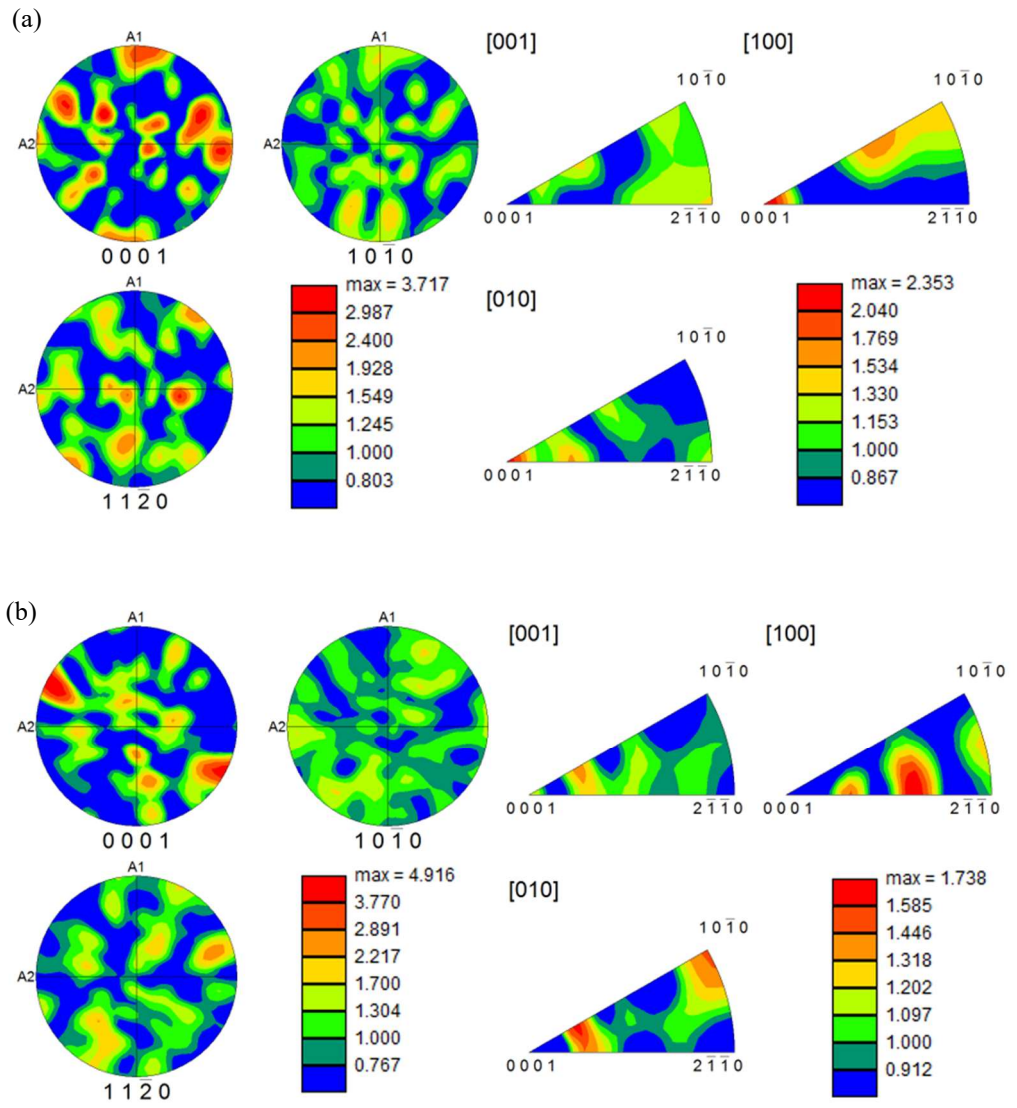

Figure 4.2: Contour pole figure and inverse pole figure plots for sample Z30AB (a) and Z60AB (b).

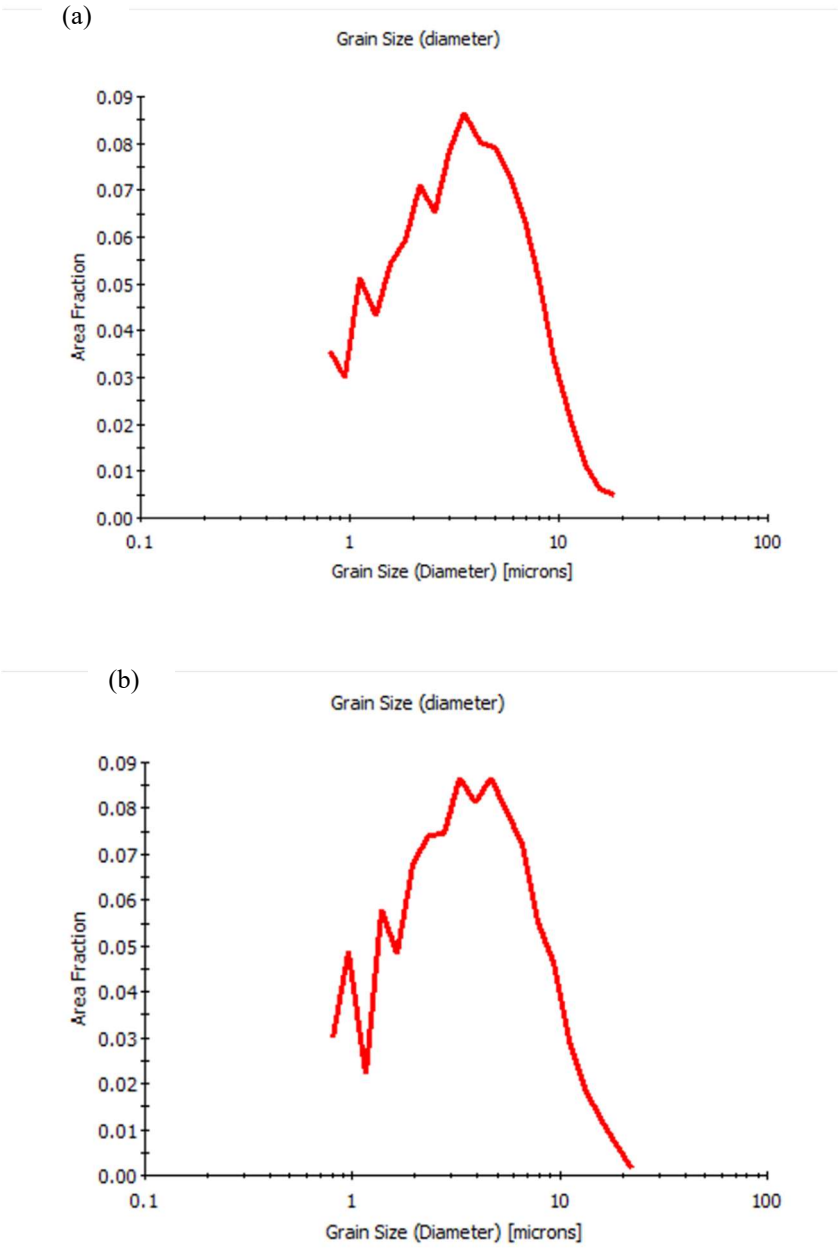

Figure 4.3: Grain size histograms showing size distribution for samples Z30AB (a) and Z60AB (b).

Both orientation maps in Figure 4.1(a) and (b) show a fine needle-like, or acicular, structure in the α phase. No β phase was detected in the analysis. This is visually consistent with what was presented in the SEM backscattered electron images in section 3.2.2, and consistent with observations made in literature as noted in section 3.2.2. Additionally, there seems to be remnants of the prior β grain structure seen in both orientation maps. Although it is possible to reconstruct

prior β grain boundaries using the α orientation maps and Burgers orientation relationships (Simonelli, 2014), this reconstruction was not performed here. Instead, outlines of what are thought to be boundaries of prior β grains were manually traced for both samples and are given in Figure 4.4 to provide a sense of the general appearance of these grains. It is clear from Figure 4.4 that the prior β grains appear to be wider and generally larger in the Z60AB sample in (b) than in the Z30AB sample in (a). In both cases, the prior β grains are elongated and preferentially oriented parallel to the build direction. This is consistent with what is seen in literature as noted in section 3.2.5 (Xu, et al., 2015). Nonetheless, the dual scale structure of the AM metal is clear in Figure 4.4 where prior β grain boundaries elongated in the build direction span hundreds of microns in length while containing an acicular α phase structure of micron thickness and of similar orientations within each β grain boundary. Investigating how this dual length scale structure affects the developing of local strain inhomogeneity under loading is one of the main goals of this effort.

(a)

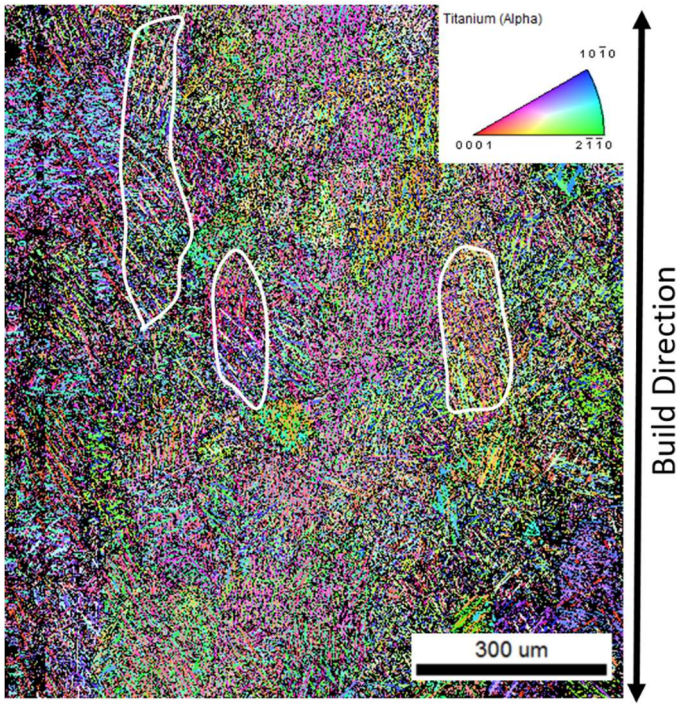

Figure 4.4

(b)

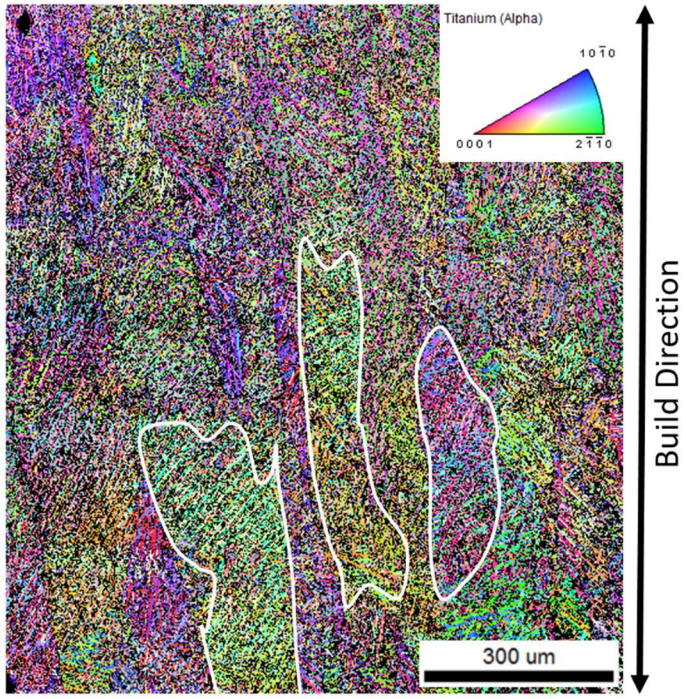

Figure 4.4 (cont.): A few traced potential prior β grain boundaries for the Z30AB sample in (a) and the Z60AB sample in (b) based on the orientation maps in Figure 4.1.

The contour pole figures presented in Figure 4.2 for the Z30AB sample in (a) and the Z60AB sample in (b) show that there is no clear texture in the α phase. This is consistent with observations of the orientation maps showing no large regions of α phase colonies and with what is observed in literature for laser melted Ti-6Al-4V (Simonelli, 2014). However, reconstructing the prior β phases may reveal a preferential [1 0 0] texturing of the cubic β phase on the observed area of interest as observed in Simonelli (2014). Finally, it appears from the grain size histograms (also provided by EBSD Analytical) in Figure 4.3 for the Z30AB sample in (a) and the Z60AB sample in (b) that the α grain size is similar between the two samples and relatively fine compared to the very large prior β grains outlined in Figure 4.4.

4.1.2 Layer Bands

One observation made in the SEM backscattered electron composition mode images was the presence of regularly spaced dark "layer bands" oriented perpendicular to the build direction. These layer bands shown for samples Z30AB-4 and Z60AB-2 in Figure 4.5 were spaced about 85 μm apart for the 30 μm layer samples and 170 μm apart for the 60 μm layer samples, roughly 3 times the layer thickness for each type of sample. Layer bands seen in AM Ti-6Al-4V have been referenced in literature on several occasions including in Wu et al. (2004), Kobryn and Semiatin (2001), Kobryn and Semiatin (2003), Kelly and Kampe (2004), Baufield et al. (2010), Thijs et al. (2010), Murr et al. (2009), Zhai et al. (2016), and Carroll et al. (2015). Several different explanations have been given as to what causes the contrast seen between the layer bands and the regions in between as well as their formation process, but most agree that their presence is due to the complex thermal history that AM metals undertake as layers are initially deposited, melted, and reheated by laser scanning of subsequent layers. In Thijs et al. (2010) it was proposed that segregation of aluminum occurred due to the fast solidification of the melt pool, and thus Ti_3Al phase precipitates were formed in these layer bands and produced the contrast seen in optical and SEM micrographs. Fluctuations in aluminum content seen in energy dispersive x-ray spectroscopy (EDS) measurements were used to confirm this. Kelly and Kampe (2004) investigated the nature of these layers using hardness, composition fluctuations, and microstructure of laser melted Ti-6Al-4V. Hardness tests were performed in that effort on the suspicion that oxygen contamination embrittled the samples at the layer interfaces. However, no significant hardness variation between layer bands and in-between regions led to that hypothesis being ruled out. Composition analysis was used to determine any amount of atomic segregation within and between layer bands, and contrary to conclusions drawn in Thijs et al. (2010), no Ti_3Al segregation was found in Kelly and

Kampe (2004). Micrographs of chemically etched samples in Kelly and Kampe (2004) showed Widmanstätten α phase structure in the layer bands compared to a coarser basketweave α structure in the surrounding areas. Conclusions were then drawn that the appearance of these layer bands is due to thermal heating across several layers resulting in these differences in structure between layers (Kelly & Kampe, 2004). Disappearance of these layer bands is seen at higher laser powers, which suggests the reheating coarsens a larger volume of the build to the point where the entire structure is coarsened and layer bands are indistinguishable from the rest of the part (Wu, et al., 2004).

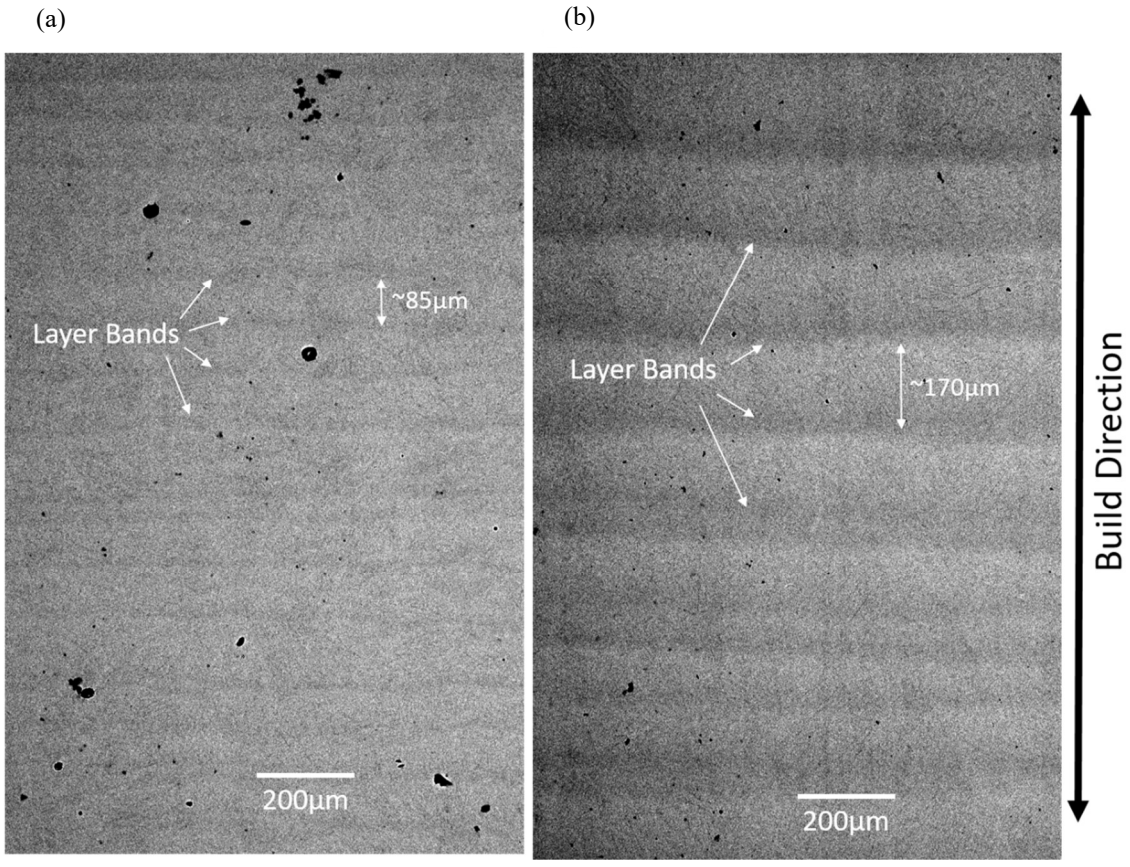

Figure 4.5: SEM backscattered electron composition mode images of polished samples Z30AB-4 (a) and Z60AB-2 (b) showing the difference in layer band thicknesses between the two samples.

In a similar manner to Kelly and Kampe (2004), in the present work microhardness tests were performed on a polished face of sample Z30AB-1 with a 100 g weighted indenter to allow the indentation size resolution needed to measure the hardness within a layer band. These images were then overlapped with SEM backscattered electron composition mode images seen in Figure 4.6 to determine indentation locations with respect to the layers and the results of the hardness tests are shown in Table 4.1. Comparing hardness measurements in the dark regions to measurements in the light regions showed no significant variation in hardness, similar to Kelly and Kampe's (2004) results. To study any composition segregation due to possible Ti_3Al precipitates, a line scan composition analysis was performed on the Z30AB-1 sample using a JEOL 6060LV SEM. From this analysis with results seen in Figure 4.7, no periodic fluctuation in the composition of any constituent element was seen. This again agrees with the findings of Kelly and Kampe (2004). No optical micrograph analysis was performed on samples as no etching was done, however, it may be reasonable to expect a similar form of structure differences in the metal when comparing regions between layers and within layers after segregation and potential oxygen contamination embrittlement were not shown in these tests. This, structure difference conclusion was drawn in Kelly and Kampe (2004), Kobryn and Semiatin (2001), Kobryn and Semiatin (2003), and Wu et al. (2004) for laser melted Ti-6Al-4V before.

Table 4.1: Average Vickers hardness number (VHN) and standard deviation for measurements located on layer bands and between layer bands. 20 measurements were taken in total. 13 of these were located between layer bands while 7 were located on layer bands. A 0.1kgf weight used.

VHN	Average	Standard Deviation
Between Layer Bands	449.1	19.9
On Layer Band	445.0	23.9

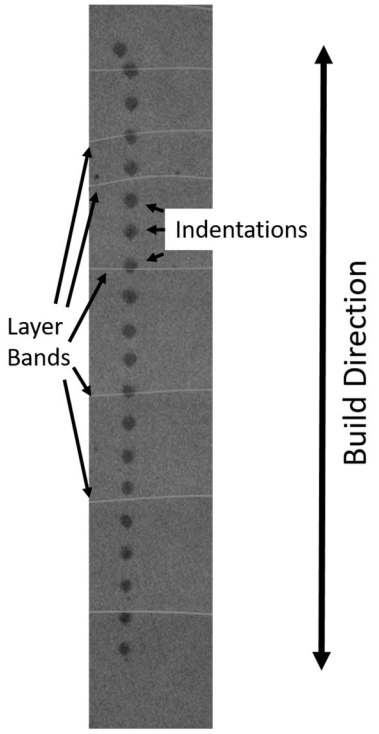

Figure 4.6: Overlapped image of microhardness indentations with SEM backscattered electron image showing the locations of the layer bands, which are traced for easier visualization. Indentations were made in a line and are labelled.

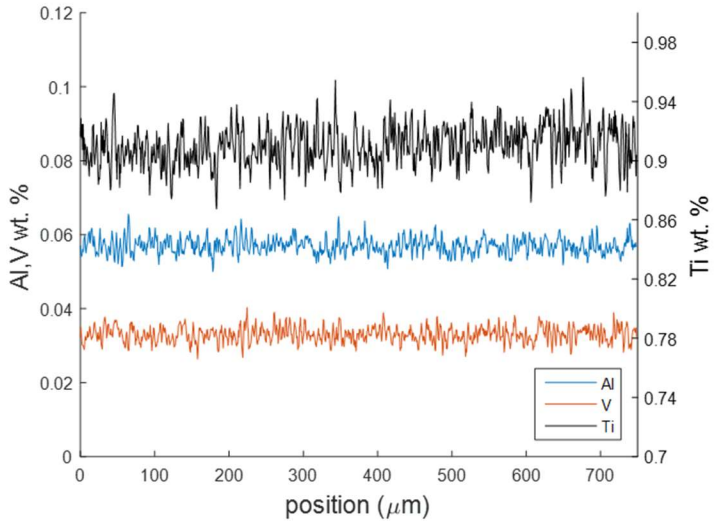

Figure 4.7: Energy dispersive electron spectroscopy (EDS) line scan showing the composition changes of the various constituent elements along the build direction.

It is unclear why the layer band spacing observed in this work is only seen every 85 µm for the 30 µm layer thickness samples and every 170 µm for the 60 µm layer thickness samples

corresponding to roughly 3 layers. Layer banding has been previously seen to occur at spacings roughly equivalent to layer thicknesses as seen in Wu et al. (2004), Zhai et al. (2016) and others and at fractions of layer thicknesses in Baufield et al. (2010) and Kelly and Kampe (2004). Further work would be required to resolve this question.

One of the main goals of this high magnification strain study was to relate the observed strain field to any microstructural features such as α or prior β grain boundaries or the layer bands discussed in section 4.1.2. To do this, SEM images were taken in backscatter composition mode to clearly reveal layer bands and identify some prior β grain boundaries as well as observe the orientation or alignment of α laths within these boundaries. This orientation should not be confused with the orientation of the crystal structure visible in the EBSD analysis images. A stitched SEM image of the area of interest for ex-situ imaging taken in backscatter composition mode is shown in Figure 4.8. Figure 4.8 also shows the same image with layer bands and visible prior β grain boundaries traced. The layer bands were traced along the line of sharpest contrast at each band.

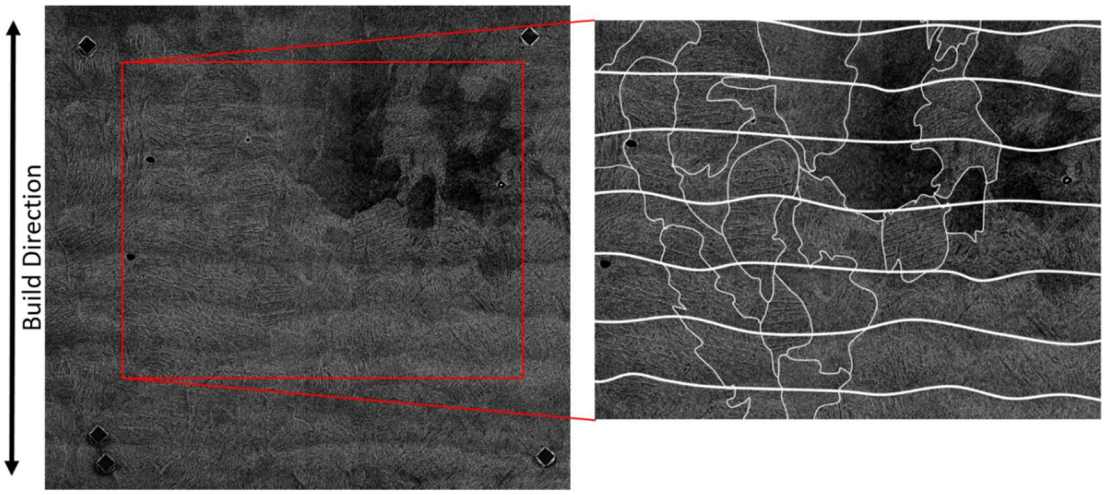

Figure 4.8: SEM backscatter electron image of region of interest showing microstructural features. Layer bands and prior β grain boundaries are traced on the image to the right.

4.2 High Magnification Ex-Situ Digital Image Correlation

4.2.1 Imaging Procedure and Sample Loading

To study how locally heterogeneous plastic strain accumulation might be affected by the dual scale structure of acicular, or needle-like, α grains within prior β grain boundaries, an ex-situ high resolution DIC study was performed on sample Z30AB-4 as detailed in (Carroll J. , Abuzaid, Lambros, & Sehitoglu, 2010). A general description of the ex-situ imaging process was given in section 2.2.6. For this study, the sample was polished and speckled with a silicon powder particle pattern as was needed for the resolution requirements of this experiment. To map out the area of interest for ex-situ image correlation, fiducial markers were made on the sample prior to taking any images. The area of interest used was 808x603 μm and the fiducial markers can be seen outside of this area in the magnified optical image shown in Figure 4.9. To achieve the high resolution DIC measurements required, 72 images of the patterned surface in the area of interest were captured before any deformation using an optical microscope with a 40X objective lens that gave a pixel spatial resolution of 0.1817 μm/pix and stitched together prior to loading the sample in tension to a total strain of 0.0310 mm/mm as measured by the extensometer. The sample was then carefully unloaded and 65 more images were taken of the surface at the same optical magnification and under the same lighting conditions. The stress and strain of the first loading cycle is plotted in Figure 3.1 in section 3.2.1 and replotted along with load cycle 2 in Figure 4.10, and the yield strength and modulus as measured by the extensometer are presented in Table 4.2 seen in section 4.2.3. The sample was then loaded once more in a second experiment until an extensometer strain of 0.0243 mm/mm was reached. The extensometer was zeroed before the first load cycle and before the second load cycle so the 0.0243 mm/mm strain did not include any plastic strain incurred in the sample from the first loading. Subsequently, 90 images at the same optical magnification

were again taken on the microscope and stitched together. Although the images were taken in a grid-like fashion to allow correspondence of individual images within one set of ex-situ images to another, there were several occasions, especially after the second load cycle, where optical focus was not maintained within a given image. To correct this, images were taken at intermediate locations between grid spaces to provide full focus in the stitched image. This was the reason different numbers of images were stitched together at each set of ex-situ images.

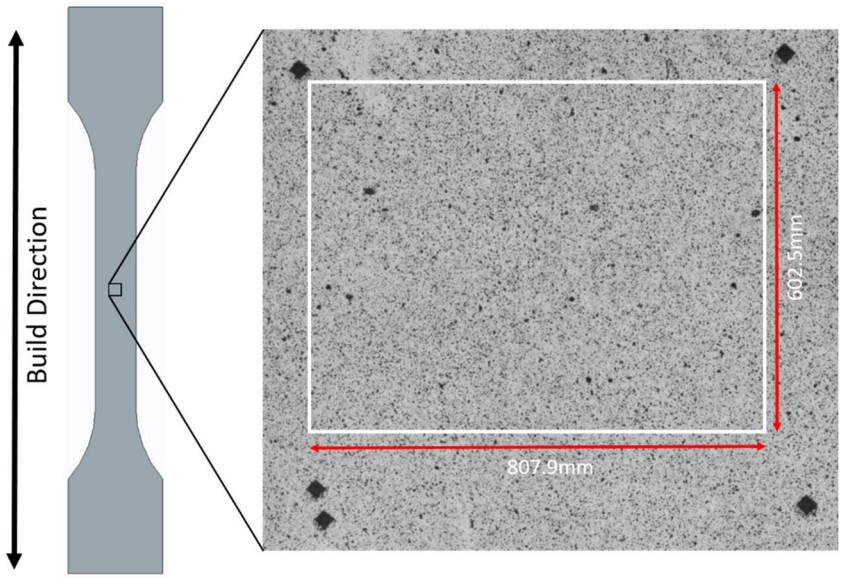

Figure 4.9: Schematic showing location of area of interest on the tension sample. Fiducial markers as well as the silicon powder particle speckle pattern can be seen on the area of interest. The region used for ex-situ DIC correlations is outlined with a box.

Figure 4.10 shows the two stress strain curves from the two load cycles used in this experiment. For clarity, Figure 4.10 is labelled with circled numbers to represent points where ex-situ images were taken. These will be referred to as points 1, 2, and 3 for the duration of the chapter. The second stress strain curve was offset in strain such that the intersection point of the modulus as calculated from the second load cycle data with the x-axis was set equal to the x-intercept of a line that runs through the final data point on load cycle one with slope equal to the modulus of the first load cycle. This strain value was 0.0193 mm/mm and a strain value of 0.0335 mm/mm was

calculated in a similar manner for the second load cycle as these values represent the expected extensometer unloaded strains at points 2 and 3 where the elastic portions of the stress strain curves are removed. These strain values are presented in Table 4.2 in section 4.2.3 and compared to average strains measured from DIC.

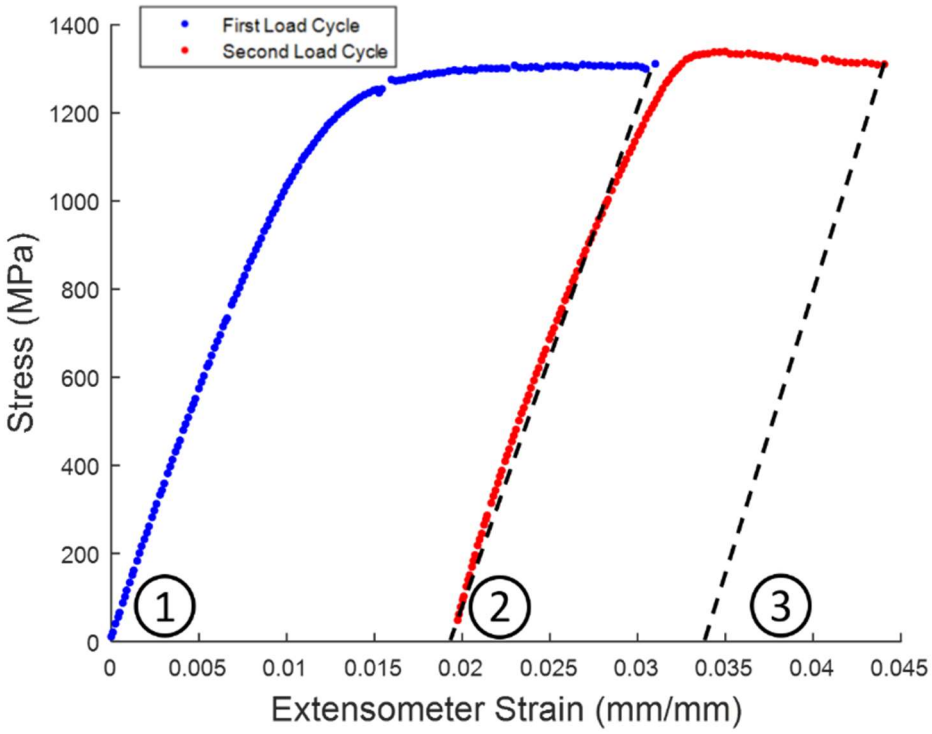

Figure 4.10: Plot of stress vs. strain for the 2 load cycles. The second load cycle was offset such that the expected strain after unloading the sample during the first load cycle matched the initial strain at zero load to start the second cycle. Dashed lines representing this unloading stress and strain are shown in black. The circled numbers 1, 2, and 3 represent the states (with stress = 0) at point 1, point 2, and point 3 referenced throughout the rest of Chapter 4.

4.2.2 High Magnification Ex-Situ Correlations

Correlations performed on the stitched images over the area of interest for sample Z30AB-4 had a subset size of 31x31 pixels (5.63x5.63 µm) with a step of 5 pixels (0.91 µm) for a total of 614,422 correlation points. This subset size is significantly smaller than both the distance between layer bands and the prior β grain sizes that are traced in Figure 4.8 and roughly equivalent to the α grain size seen in Figure 4.1. The stitched images corresponding to unloading points 2 and 3 in

Figure 4.10 were correlated to the image at point 1 (undeformed state), and additionally, the stitched image of point 3 was correlated to the image at point 2 separately to directly quantify the strain accumulation between load cycles. A comparison of average axial strains (ε_{yy}) strains calculated at points 2 and 3 using various different methods is seen in Table 4.2. The elastic modulus calculated using the extensometer measured strains (see section 3.2.1 for more details on this) is also presented in Table 4.2. Finally, yield strength for the first load cycle is also shown. "Extensometer expected unloaded strain" refers to the strains calculated and presented in section 4.2.1, while the DIC spline fit averaged strain is calculated from fitting spline curves to the DIC displacement fields for the correlations of points 2 and 3, determining the gradient of displacement from these spline fits at each point, $\varepsilon_{yy} = \frac{\partial v}{\partial y}$, and averaging over the field. Finally, DIC displacement field linear fit is the slope of a linear regression fit of the displacements in the direction of applied tension, *v*, to the positions, *y*, calculated as it was presented in section 2.2.5. There is good agreement between the DIC spline fit averaged strain and the DIC displacement field linear fit calculated strain suggesting that even at this narrow field of view, 808x603 μm, a linear fit estimate of strain works in an average sense. The difference in strain with the extensometer-expected unloaded strain shows opposite behavior to that seen in the in-situ measurements where the DIC strain deviated to a higher value as compared to the extensometer strain measurement as the sample was strained beyond the yield point. In the in-situ measurements, this behavior was explained with the observation that the area of interest in the in-situ measurements was physically smaller than the gauge length of the extensometer and thus contains a larger area proportion of the necking region during plastic deformation resulting in higher averaged measured strain. This explanation can also be used to describe the opposite behavior seen in the ex-situ measurements. The 808x603 μm size area of interest is small compared to the

3,000x12,700 μm area between the extensometer arms and may be outside of the necking region and thus, not fully representative of the larger strains expected in the necking region giving an artificially lower value.

Table 4.2: Comparison of strains at points 2 and 3 calculated with different methods described in sections 4.2.1 and 4.2.3. The elastic modulus calculated from the extensometer strain measurements are shown as well for both load cycles and the yield strength is presented for load cycle 1.

Load Cycle	Elastic Modulus (GPa)	Yield Strength (MPa)	Extensometer Expected Unloaded Strain (mm/mm)	DIC Spline Fit Averaged Strain (mm)	DIC Displacement Field Linear Fit (mm/mm)
Load Cycle 1	112.4	1178.7	0.0193	0.0165	0.0167
Load Cycle 2	123.7	N/A	0.0335	0.0246	0.0242

Contour plots of the high resolution DIC strain fields were generated, aligned, and overlapped with the traced layers and prior β grain boundaries to produce several of the figures included in this section and section 4.2.3. Strain fields for the correlations of loading points 2 and 3 to point 1 are presented in Figure 4.11, Figure 4.12, and Figure 4.13. Figure 4.11 includes the strain in the direction of applied tension, ε_{yy}, while Figure 4.12 shows the strain transverse to the tension direction, ε_{xx}, and Figure 4.13 shows the shear strain, ε_{xy}. The first observation to be made from Figure 4.11, Figure 4.12, and Figure 4.13 is that the strain fields in all contours show highly heterogeneous strain accumulation that is not seen in the low magnification in-situ measurements. It is also clear that ε_{yy} is the dominant strain with magnitudes more than five times higher than the other two components (ε_{yy} and ε_{yy}), as seen in the contour bars of Figure 4.11. When considering strain in the direction of tension, ε_{yy}, some regions in Figure 4.11(a) and Figure 4.11(b) show very low strain, even negative strain in some areas, whereas other areas show strain values greater than twice the DIC spline fit average strain. To illustrate this further, a histogram of the strain field for ε_{yy} is plotted for both load cases and overlapped in Figure 4.14(a). Furthermore, Figure 4.14(b)

highlights the change in the average strain from point 2 to point 3 as well as the change in the minimum and maximum strain values. An increase in the average strain and the maximum strain is seen both in the shift of the histogram in Figure 4.14(a) and the plot in Figure 4.14(b). The minimum strain has very little change as it goes from -0.0060 mm/mm to -0.0056 mm/mm, especially when compared with the change in the average and maximum strain. These observations, combined with the noticeable widening of the histogram corresponding to the strain accumulation after the second load cycle, suggests that not only do the strain fields exhibit significant heterogeneity, but that heterogeneity (defined as the difference between minimum and maximum local strain) increases as the material is further strained.

(a)

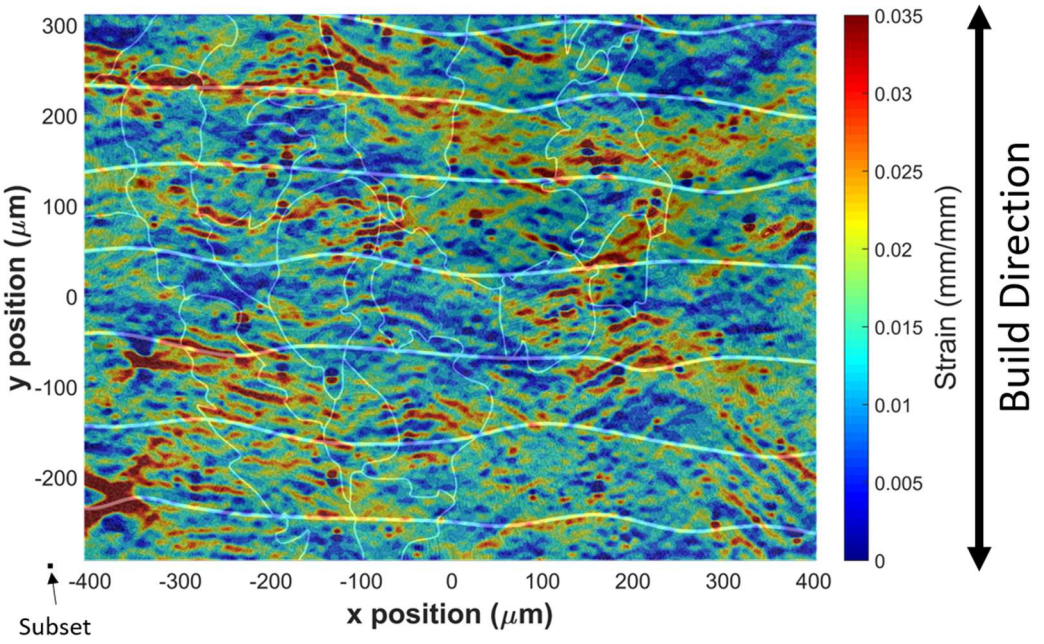

(b)

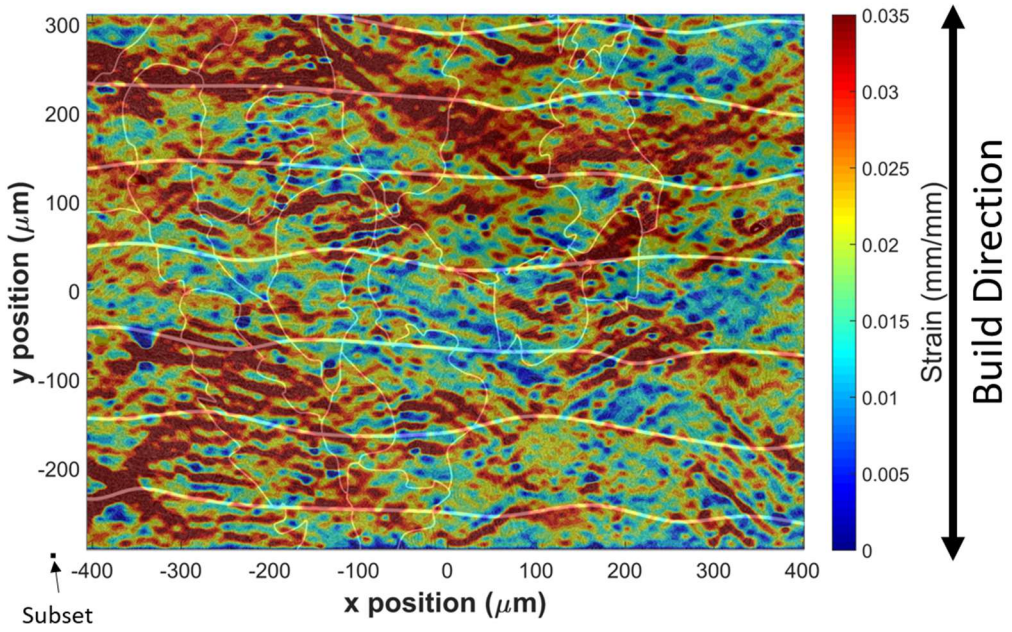

Figure 4.11: Contour plots of ε_{yy} for the correlation of point 2 to point 1 (a) and point 3 to point 1 (b). The subset size is represented in the lower left corner of each plot. Subset size was 31x31 pixels (5.61x5.61μm) with a step of 5 pixels (0.91μm) and a total of 614,422 correlation points.

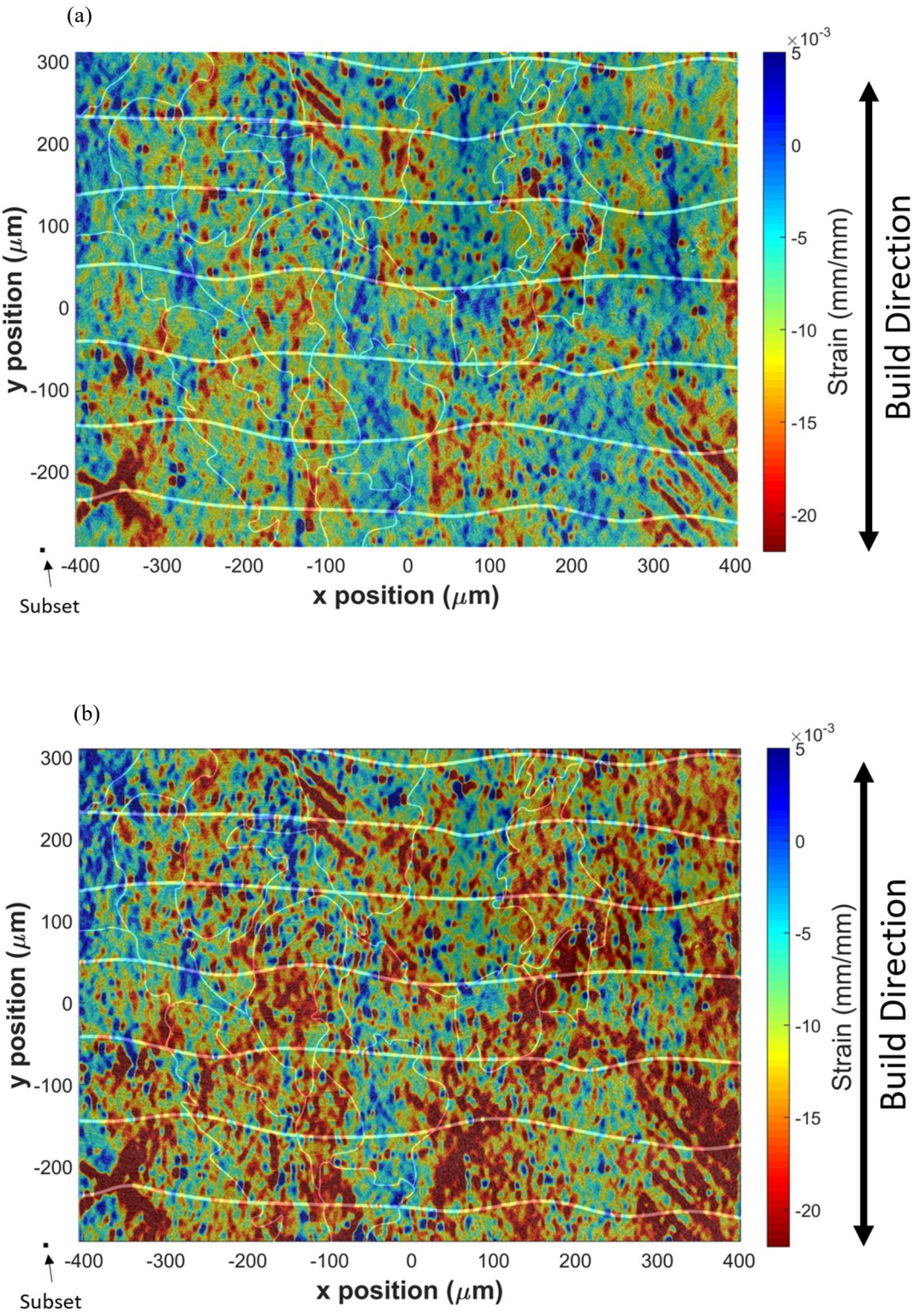

Figure 4.12: Contour plots of ε_{xx} for the correlation of point 2 to point 1 (a) and point 3 to point 1 (b). The subset size is represented in the lower left corner of each plot. Subset size was 31x31 pixels (5.61x5.61µm) with a step of 5 pixels (0.91µm) and a total of 614,422 correlation points.

(a)

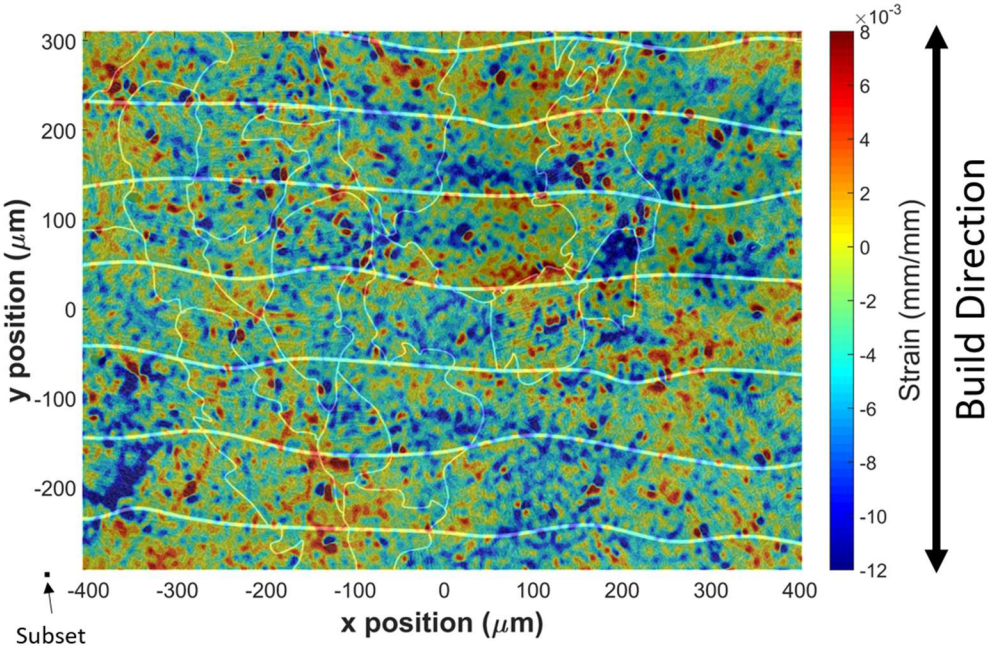

(b)

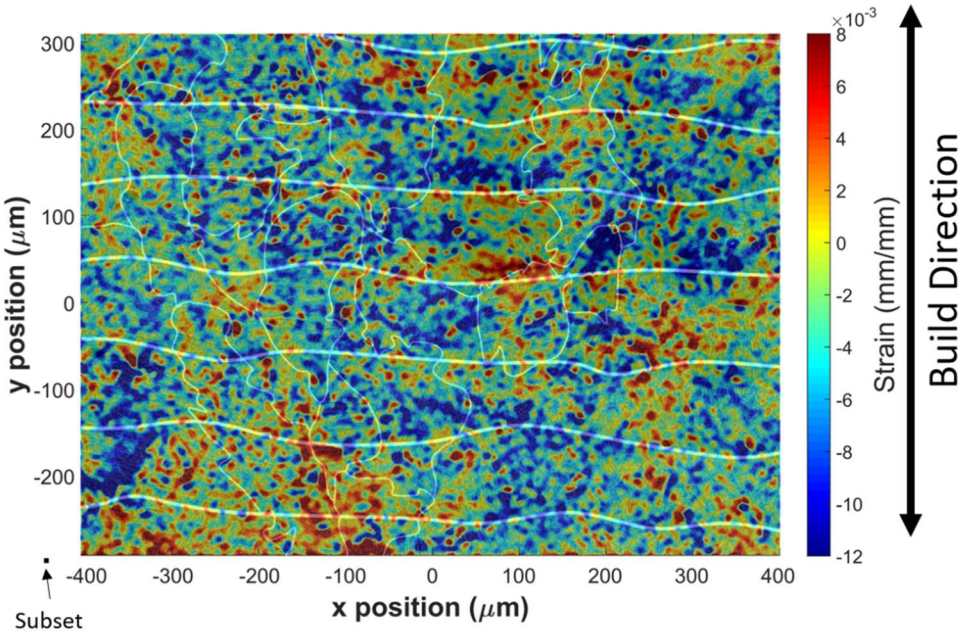

Figure 4.13: Contour plots of ε_{xy} for the correlation of point 2 to point 1 (a) and point 3 to point 1 (b). The subset size is represented in the lower left corner of each plot. Subset size was 31x31 pixels (5.61x5.61μm) with a step of 5 pixels (0.91μm) and a total of 614,422 correlation points.

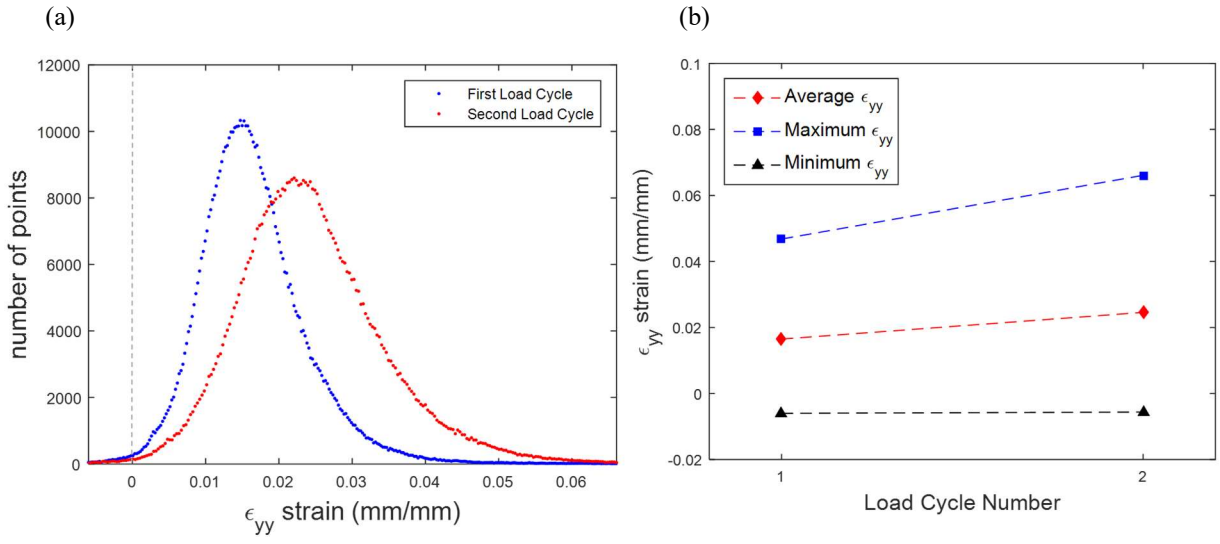

Figure 4.14: A strain histogram of ε_{yy} plotted for the correlation of point 2 to point 1 and point 3 to point 1 is shown in (a) while a plot of showing the strain evolution of the average, minimum and maximum recorded strains is shown in (b). A shift of the histogram to higher strain is seen from load cycle 1 to load cycle 2 in (a) showing an increase in the average strain also seen in (b). A widening of the histogram in (a) and the range between minimum and maximum strains in (b) indicates an increase in the strain heterogeneity.

4.2.3 Effect of Microstructure on Strain Field Inhomogeneity

From Figure 4.11 any microstructural effects on the strain field appear most obvious in the plots of ε_{yy}. Particularly, the most obvious features in the strain field are the striations of alternating high and low strain seen almost everywhere in the contour plot. These striations are also seen in the ε_{xx} contour plots of Figure 4.12, and they appear to align with the long axis of the acicular α phase. To better illustrate this, the contour plot in Figure 4.11(b) is plotted alongside the SEM backscatter electron image for Z30AB-4 (Figure 4.8) in Figure 4.15. White arrows showing the similarity in strain striation orientation (Figure 4.15(b)) and microstructural martensitic lath alignment (Figure 4.15(a)) in some of the more obvious locations are also shown. Furthermore, a line scan plot (see Figure 4.16) shows the measured strain along the black line pictured in Figure 4.15(b). The *x*-axis of Figure 4.16 gives the *y*-coordinate position of the contour plot seen in Figure 4.15(b). The measured strain along this line scan is seen to oscillate between high and low values for both pictured load cycles in Figure 4.16. High strain near α laths could be due to void formation

and growth in these areas. Void formation and growth is important in low work hardening rate alloys such as Ti-6Al-4V and especially with martensitic Ti-6Al-4V due to the preference of void formation over slip transfer at martensitic lath interfaces. In martensitic Ti-6Al-4V it is common to see this void nucleation and subsequent growth aligned with the laths (Banerjee & Williams, 2013) and (Margolin & Mahajan, 1978). Thus, observations of preferential strain alignment with martensitic α laths are consistent with literature. Additionally, terraced features thought to correspond with crack propagation along α grain boundaries were observed scattered across the observed fracture surfaces presented in Figure 3.11 out of section 3.2.6. Figure 3.11 is reshown here in Figure 4.17 for convenience. Note the regions of voiding along the terraces potentially associated with the high strain measured along these interfaces.

(a)

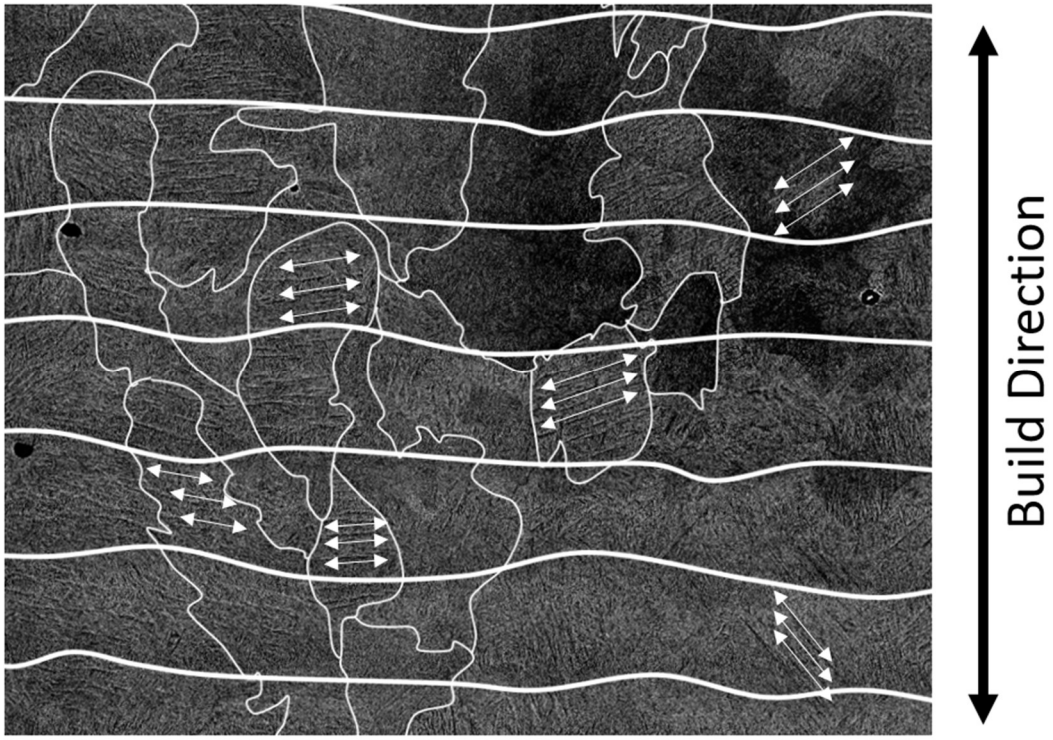

Figure 4.15

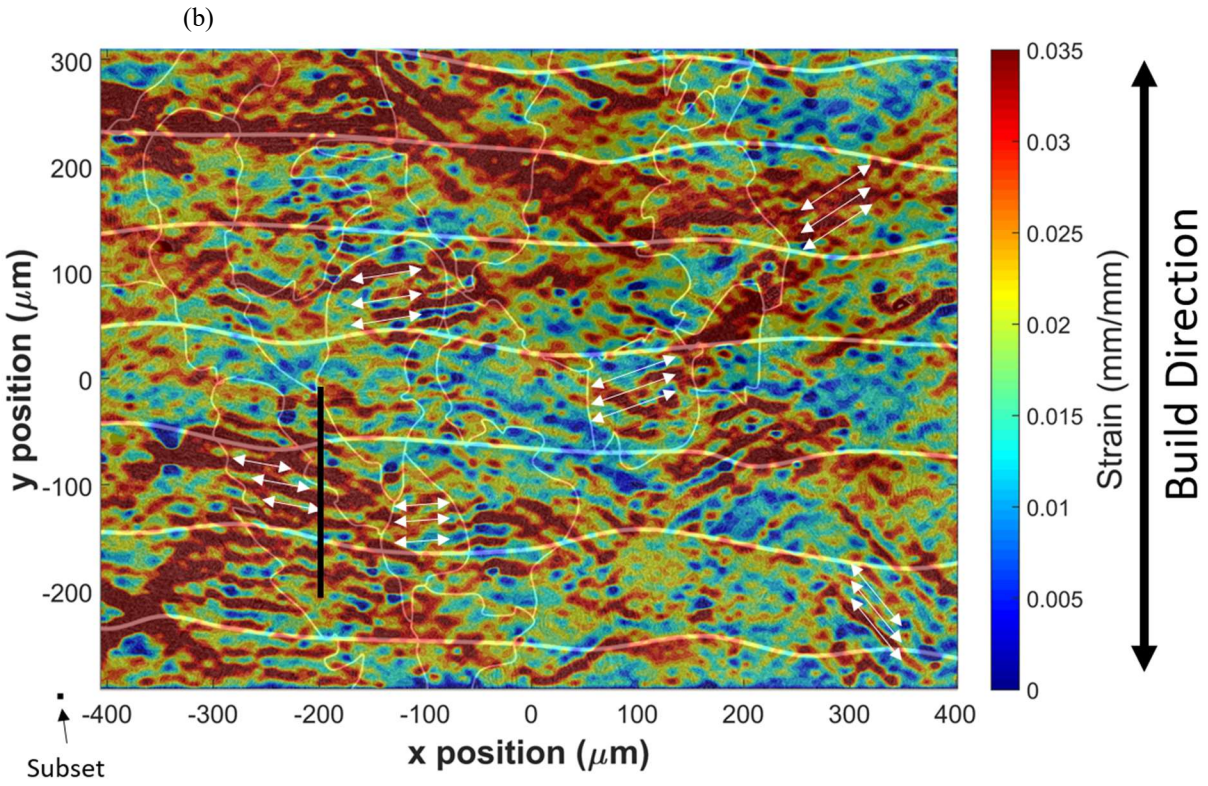

Figure 4.15 (cont.): SEM backscatter image of region of interest with traced layer bands and prior β grain boundaries (a) alongside a contour plot of ε_{yy} for correlation from point 3 to point 1 (a). Arrows indicating the alignment of martensitic α laths in (a) are also shown in (b) to visualize the alignment of strain accumulation with the laths. The subset size is represented in the lower left corner of each plot. Subset size was 31x31 pixels (5.61x5.61μm) with a step of 5 pixels (0.91μm) and a total of 614,422 correlation points.

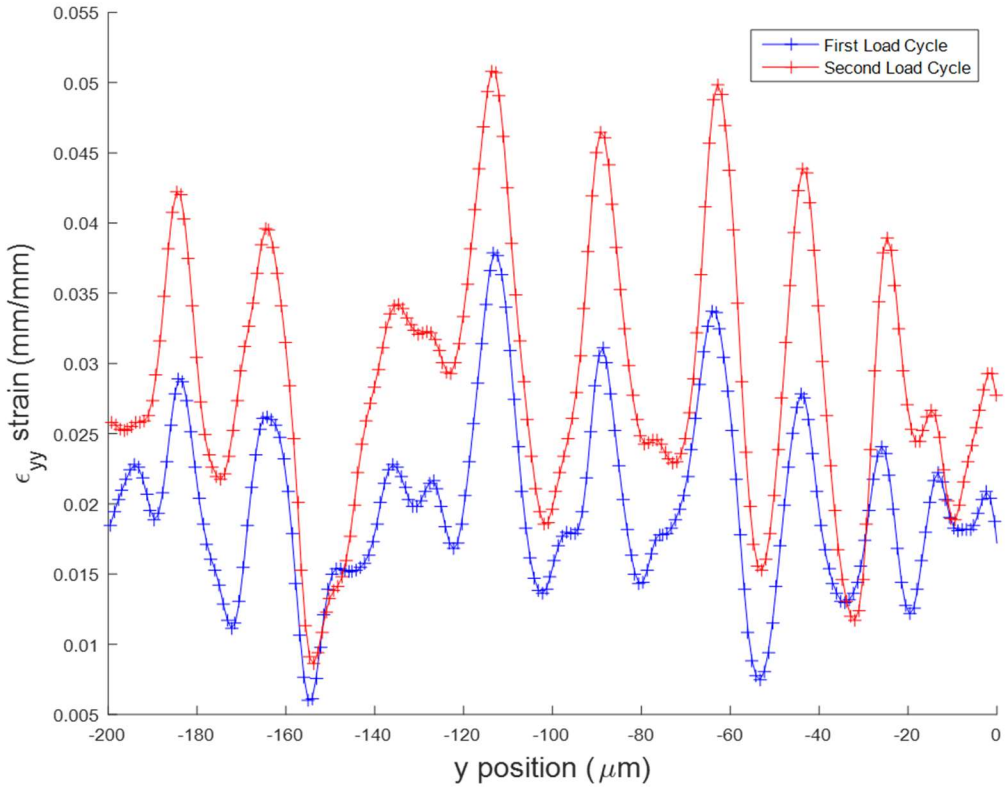

Figure 4.16: Line scan showing the accumulated strain (ε_{yy}) along the black line pictured in Figure 4.15. The peaks and valleys along the line show large strain heterogeneity associated with strain accumulation at α phase laths.

(a) (b)

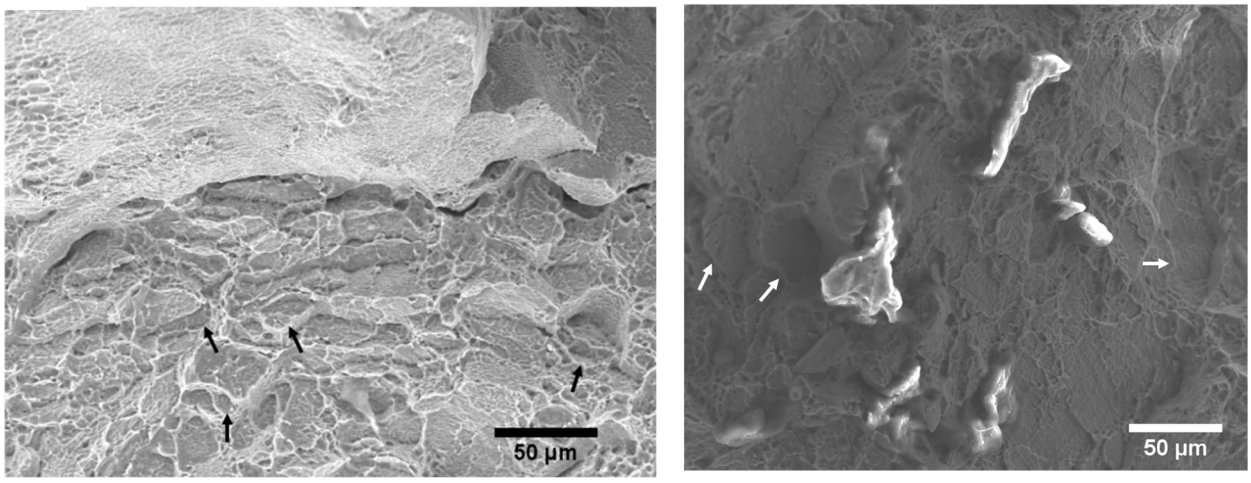

Figure 4.17

(c)

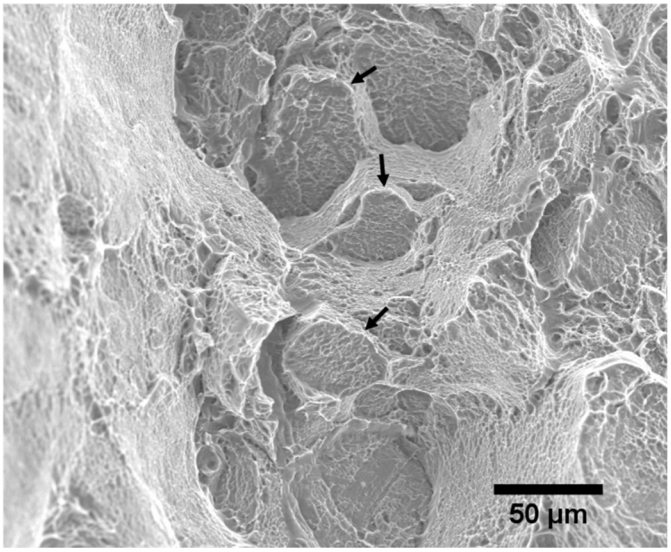

Figure 4.17 (cont.): Images of terraced features from Figure 3.11 for samples Z30AB-1 (a), Z30HT-1 (b), and XY30AB-1 (c). These features are thought to be due to crack propagation across martensitic α lath interfaces.

A secondary observation is seen in the strain accumulation at the traced layer bands. A few of these areas are circled, numbered and presented in Figure 4.18 for the ε_{yy} strain of the correlation of loading point 3 to the reference state of point 1. It can be seen in region 1 that an area of high strain runs in line with the layer band centered in the region across the outlined prior β grain boundaries. In region 2, strain within β grains is shown to fluctuate in magnitude across traced layer bands. The traced prior β grain boundary on the left side of region 2 has very large strain confined between two layer bands, and the prior β grain to its right likewise has large strain confined between the layer bands with higher strain seen nearer to the lower layer band. Region 3 shows a prior β grain where preferential strain alignment with α lath direction is evident, yet larger strain is seen to be confined between the 2 layer bands within the region with strain dropping off above the top layer band. Finally, region 4 shows a prior β grain where regions of high and low strain are clearly separated by a layer band. As described in sections 3.2.4 and 4.1.2, each layer deposition presents an opportunity for microstructural discontinuities such as grain orientation

mismatch or cyclical coarsening of grain structure due to the repeating pattern in thermal history as the part is manufactured. Specifically, in section 4.1.2 it was suggested that a coarsening of grain structure may be possible at the observed layer bands as further investigations of the layer bands remained consistent with observations of Kelly & Kampe (2004). These discontinuities present preferential locations of void nucleation due to strength mismatch at these interfaces (Banerjee & Williams, 2013). In section 3.2.4 this was used to potentially describe the observed anisotropy in yield strength seen in the AM Ti-6Al-4V samples. Thus, the strain accumulation at layer bands seen in Figure 4.18 could be due to this effect of void nucleation at microstructural discontinuities associated with the coarsening of α laths at these layer bands.

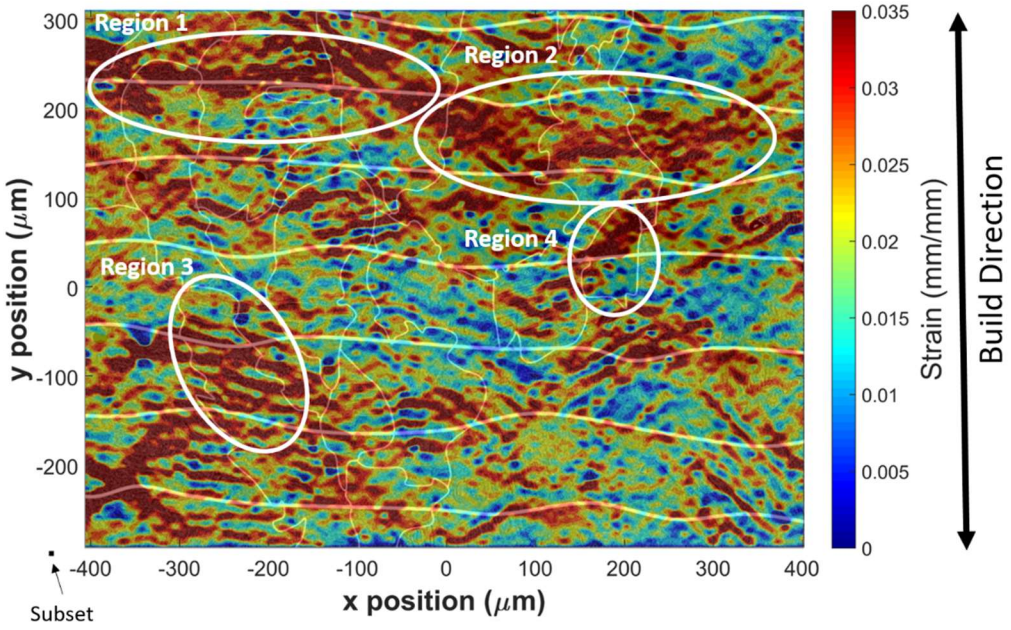

Figure 4.18: Contour plot of ε_{yy} for correlation from point 3 to point 1 showing circled regions of possible interactions of the strain field with layer bands. The subset size is represented in the lower left corner of each plot. Subset size was 31x31 pixels (5.61x5.61μm) with a step of 5 pixels (0.91μm) and a total of 614,422 correlation points.

There appears to be little association of prior β grain boundaries with regions of high or low strain. One of the only noticeable regions where high strain is seen at a prior β grain boundary

is circled in the ε_{xy} plot of the correlation of point 3 to point 1 shown in Figure 4.19. As stated in section 3.2.4, a common explanation given in literature for observed macro-scale anisotropy in yield strength and ductility of AM Ti-6Al-4V is that preferential slip can occur at prior β grain boundaries slip can occur at prior β grain boundaries. The lack of high strain accumulation at prior β grain boundaries seen in this micro-scale analysis shows that this explanation is not sufficient to describe the macro-scale anisotropy seen in samples presented in this work with macro-scale properties given in Chapter 3. Furthermore, β phase is not seen in the EBSD results in section 4.1.1, and thus there is no potential for this interface to occur. In the absence of grain boundary α, preferential void nucleation can be seen along martensitic α laths (Banerjee & Williams, 2013). This is consistent with the observation of high strain accumulation aligned preferentially with martensitic α laths made earlier.

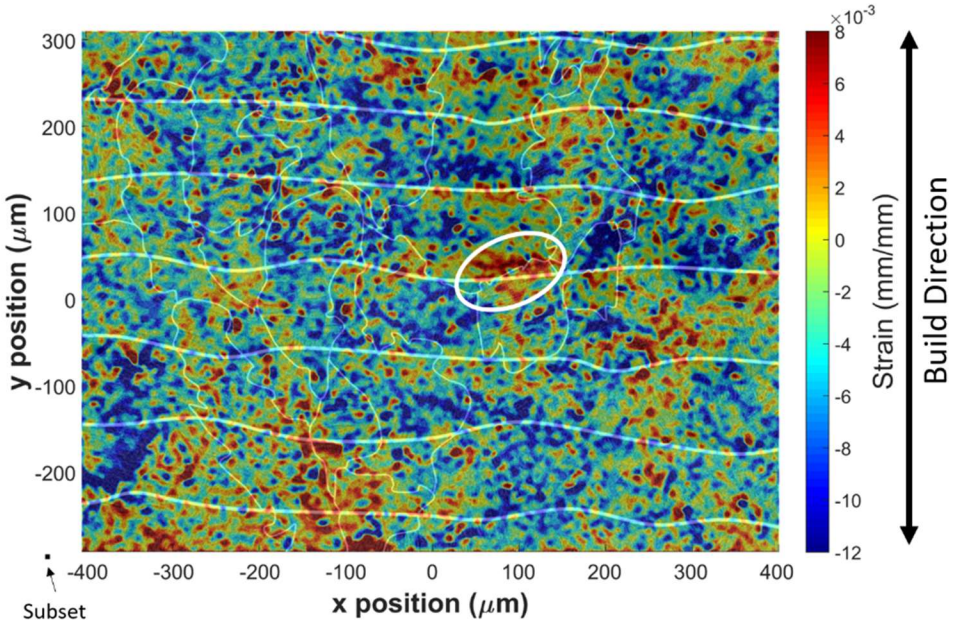

Figure 4.19: Contour plot of ε_{xy} for correlation from point 3 to point 1 showing a circled region of high shear strain in at a prior β grain boundary. The subset size is represented in the lower left corner of each plot. Subset size was 31x31 pixels (5.61x5.61μm) with a step of 5 pixels (0.91μm) and a total of 614,422 correlation points.

As mentioned earlier, the results from the correlation of point 2 to point 1 were subtracted from the results of the correlation from point 3 to point 1 to represent the changes from point 2 to point 3. Contour plots of the strain from this operation are shown in Figure 4.20. The first observation to note in Figure 4.20 is the accumulation of strain in the same relative areas in the field of interest when compared to the correlation of point 2 to point 1 in Figure 4.11(a). It is noteworthy that some regions that showed high strain accumulation in Figure 4.20 exhibit a greater magnitude of strain accumulation than other regions that also exhibit strain accumulation between points 2 and 3. This further cements the idea that there is increased heterogeneity within the strain field as more strain is applied. Again, strain is seen to accumulate preferentially along martensitic α laths and at the layer bands with no preferential strain accumulation along prior β grain boundaries in the ε_{yy} plot. Some of the highest strain accumulation is seen in the near the layer band in the top left corner of the contour in Figure 4.20 corresponding to region 1 marked in Figure 4.18 perhaps due to further void growth in that area. One final note to make for this correlation is that there is a gradient of strain accumulation in the contour plot of ε_{yy} shown in Figure 4.20(a) going from high strain accumulation in the upper left corner of the plot to lower strain accumulation in the lower right of the plot. This gradient again appears in the plot of ε_{xx} in Figure 4.20(b), except a higher strain accumulation is evident in the lower right corner as compared to the upper left corner. It is unclear at the present time why this is the case.

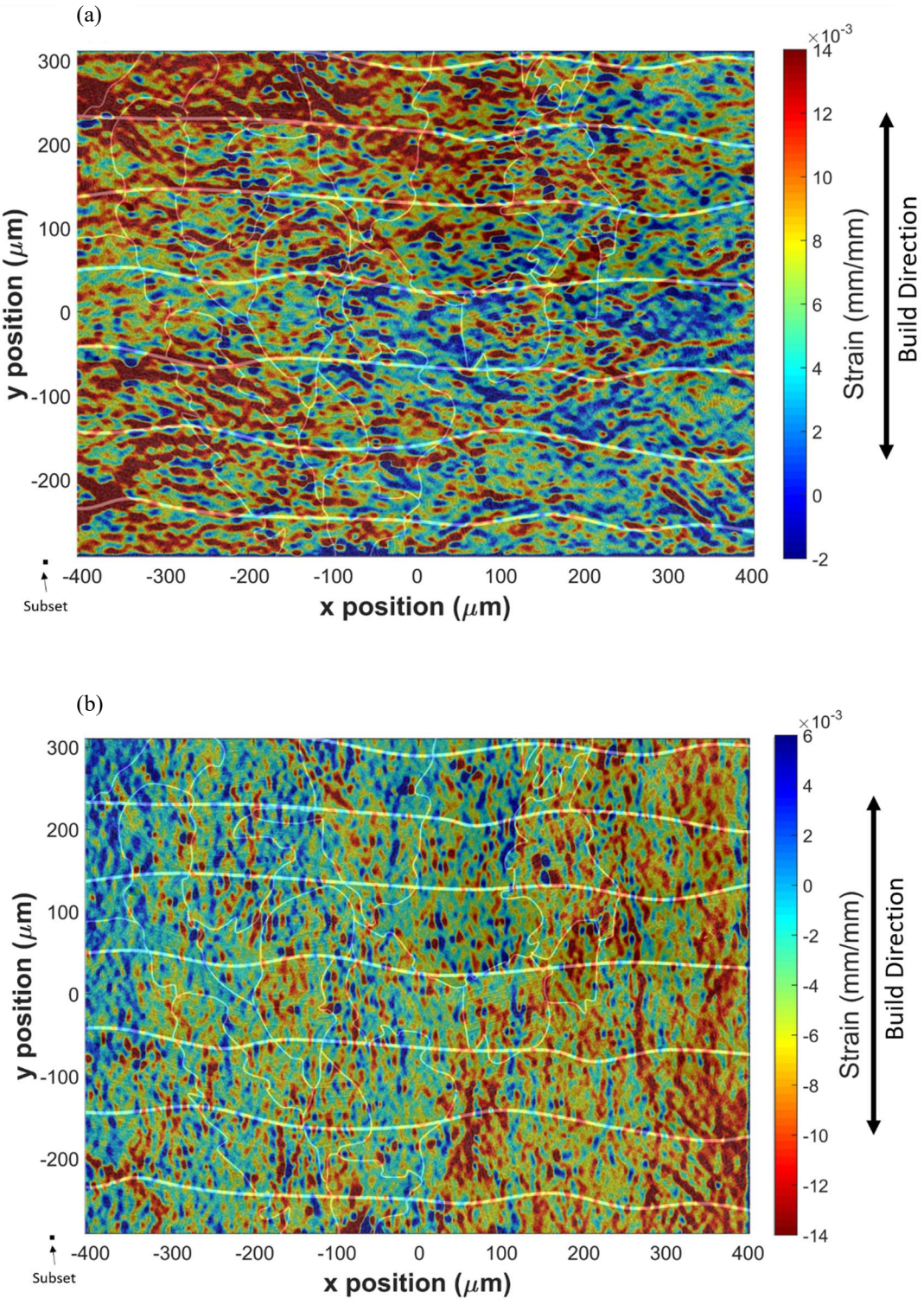
(a)
y position (μm)
x position (μm)
Subset
Strain (mm/mm)
×10^-3
Build Direction
(b)
y position (μm)
x position (μm)
Subset
Strain (mm/mm)
×10^-3
Build Direction

Figure 4.20

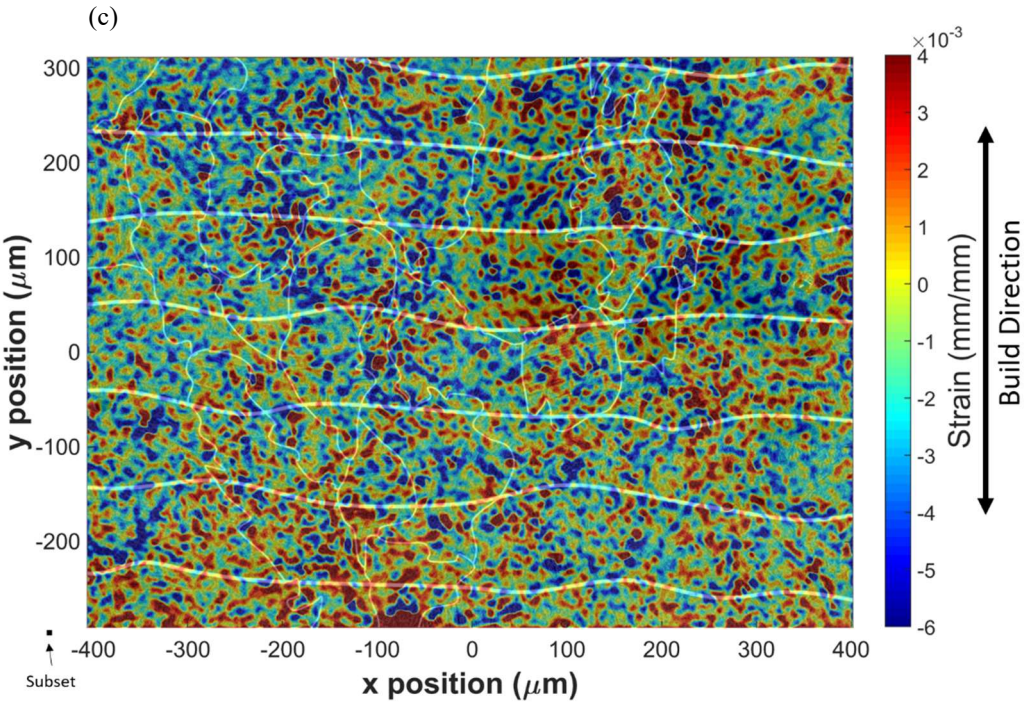

Figure 4.20 (cont.): Contour plots of ε_{yy} (a), ε_{xx} (b), and ε_{xy} (c) for the correlation of point 3 to point 2. The subset size is represented in the lower left corner of each plot. Subset size was 31x31 pixels (5.61x5.61µm) with a step of 5 pixels (0.91µm) and a total of 614,422 correlation points.

Chapter 5: Conclusions and Future Work

The main objectives of this work were to: (a) to characterize the mechanical properties of the AM Ti-6Al-4V specimens using uniaxial tension experiments, determine if there are any differences due to a change in build orientation or layer thickness, describe these possible differences, and compare measured properties to those seen in literature, (b) to characterize the microstructure of the as-built specimens, observe changes due to build orientation or layer thickness effects, and determine the features unique to the AM process and (c) to evaluate the effects any characteristic microstructural features, especially those possible features unique to the AM process, have on the material deformation behavior by mapping strain accumulation to microstructural features. A summarized overview of the major conclusions drawn in this work is presented in this chapter organized by chapter. This chapter also presents recommendations for future work.

5.1 Conclusions Drawn from Macro-Scale Study of AM Ti-6Al-4V Specimens

Experiments presented in Chapter 3 focused on studying the bulk material behavior of the AM Ti-6Al-4V specimens and determining any differences observed due to changes in build orientation, powder bed layer thickness, or heat treatments. Hardness test measurements based on fiducial markers used to align different image sets showed a material softening of the heat treated samples as compared to as-built (non-heat treated) samples to a level consistent with annealed, conventionally processed Ti-6Al-4V. No significant hardness changes were seen due to build orientation or layer thickness. Several conclusions on the bulk material behavior were drawn from the uniaxial static tension experiments performed. As-built AM Ti-6Al-4V specimens exhibited a higher yield strength and lower ductility as compared to values provided in literature for both conventionally processed and annealed Ti-6Al-4V, and solution treated and aged conventionally processed Ti-6Al-4V. The as-built specimens tested also exhibited greater yield strength than the

tested conventionally processed and annealed Ti-6Al-4V sample. The reduction in ductility could be due to possible residual stresses not explored in this work or potential microcracks that are seen in the fracture surface images of Figure 3.13. Heat treated AM Ti-6Al-4V specimens showed a reduced yield strength to a level comparable with the tested conventional Ti-6Al-4V samples and consistent with literature on AM Ti-6Al-4V. However, a reduction in strain to failure compared to the as-built specimens is inconsistent with results seen in literature and could be due to the large imperfections seen on the fracture surface of the heat treated sample brought to failure. The reduction in yield strength and hardness of the heat treated samples is likely due to the formation and coarsening of the α colony structure presented in Figure 3.6 in section 3.2.3. Slight anisotropy was seen in the yield strength and ultimate tensile strength of the as-built AM Ti-6Al-4V specimens where XYZ oriented samples exhibited higher strength than the ZXY samples. This is thought to be due to possible microstructural discontinuities caused by layer banding described in section 4.1.2. No anisotropy was observed in ductility. Powder bed layer thickness for each deposited layer had no influence on strength or ductility. Observed specimen fracture surfaces revealed several features commonly seen in literature on AM Ti-6Al-4V. These features include large powder particle sized voids, terraced features associated with cracks along α lath interfaces, and microcracks possibly due to incomplete homologous wetting described in section 3.2.6 and in Das (2003). Ductile microvoids were also seen in large regions along the fracture surfaces.

5.2 Conclusions Drawn from Micro-Scale Study of AM Ti-6Al-4V Specimens

Chapter 4 conclusions were focused on the micro-scale deformation behavior seen on the AM Ti-6Al-4V Z30AB-4 specimen that underwent two load cycles into the plastic region of the stress-strain curve. EBSD results of undeformed samples of the Z30AB and Z60AB build configuration showed a largely acicular α phase microstructure with no β phase detected as well

as remnants of a prior columnar β grain structure with the long axis of these prior grains oriented in the build direction. Prior β grain thickness increased with an increase in the layer thickness, yet no change was seen in the α grain size distribution, which is likely due to the consistency in input energy provided by the scanning laser. This is consistent with literature on laser melted AM Ti-6Al-4V. Also, no significant texturing in the α phase was revealed in the pole figures of Figure 4.2. Layer bands perpendicular to the build direction were observed in SEM backscattered electron imaging mode separated by distances of around three layers in both the 30μm and 60μm layer thickness samples and are thought to be a visible coarsening of the acicular α grains due to multiple passes of the scanning layer causing a thermal cycling of the material.

As part of the micro-scale deformation study, significant heterogeneities were seen in the strain accumulation behavior over the area of interest in the Z30AB-4 specimen. This heterogeneity increased as the average strain increased as seen in the strain histograms and strain evolution plot of Figure 4.14 as well as in the contour plots of Figure 4.20 showing the accumulation of strain as a result of the second load cycle. Measured strain in the tension direction, ε_{yy}, was even compressive in some locations contrasting the tensile load applied. Strain was seen to largely accumulate along α grain laths most likely due to preferential voiding at these interfaces. It is the reduced slip length associated with these fine laths that give the AM Ti-6Al-4V the high strength as is discussed in Chapter 3. This behavior is consistent with behavior seen in literature on conventionally processed Ti-6Al-4V lamellar structures. Preferential strain accumulation was also seen across some prior β grains along layer bands. This is thought to be a result of void nucleation at potential microstructural discontinuities seen at layer interfaces as new layers are deposited. Finally, no preferential strain accumulation was seen along prior β grain boundaries suggesting a lack of preferential slip along grain boundary α that is commonly seen in lamellar

structures of conventionally processed Ti-6Al-4V. These last two conclusions suggest that the observed anisotropy seen in the results of the static uniaxial tension experiments of the AM Ti-6Al-4V specimens presented in Chapter 3 is not grain boundary related and likely related to the interfaces between consecutive deposited layers.

5.3 Recommended Future Work

One useful improvement that could provide additional insight on the macro-scale results presented in this work is to test a statistically larger number of samples. This would strengthen conclusions based on the observed anisotropy in strength and determine whether these samples reveal any anisotropy in ductility or increased ductility due to heat treatments as seen in literature. Fracture toughness and fatigue crack initiation and growth experiments could also be performed to further characterize the mechanical properties of this material. Results could be compared to existing literature on the fatigue and fracture properties of laser melted AM Ti-6Al-4V.

Several improvements could also be made to provide additional insight on the micro-scale results presented here. First and foremost, overlapping EBSD grain orientation maps with the high magnification ex-situ results presented here would provide more complete data and useful information on possible grain orientation effects on preferential strain accumulation. Prior β grains could be reconstructed as well in a method like that outlined in Simonelli (2014) to show the location of prior grain boundaries as well as the orientation of the prior grains. As stated in section 4.1.1, the grain orientation maps may also provide more complete data if a smaller step size was used in the EBSD scan. Higher magnifications could be used in the in-situ DIC measurements to aid measurements in the high magnification ex-situ measurements by exhibiting the effects of strain accumulation while the sample is loaded. Additionally, finer patterns combined with higher magnifications for the ex-situ measurements could reveal more details into the α grain lath

deformation behavior although the size of the area of interest may have to shrink due to the large volume of pictures required. A micro-scale study of a 60 μm layer thickness ZXY orientation sample may be of interest to complement micro-scale results seen in the 30 μm layer thickness ZXY orientation sample presented in this work. A micro-scale study of fatigue of the AM Ti-6Al-4V material may also be useful to supplement results seen here. These experiments could be performed using high magnification in-situ or ex-situ DIC measurements in a manner like that explored in Carroll (2011).

Further investigations into the microstructure by means of etching and optical microscopy or more detailed EBSD measurements at the observed layer bands could reveal the exact structure of the bands rather than relying on the indirect deductive approach presented in section 4.1.2. Also, high resolution computed tomography could provide more details on the exact geometry of any large voids present in the material either due to unmelted powder particles or incomplete homologous wetting. Finally, a thorough investigation characterizing the residual stresses in the material could be performed and compared to literature and could provide insight into the mechanical behavior seen in this work.

References

Abanto-Bueno, J. (2004). *Fracture of a Model Functionally Graded Material Manufactured from a Photo-Sensitive Polyethylene.* University of Illinois at Urbana-Champaign, Aerospace Engineering, Urbana.

Abuzaid, W. Z., Sangid, M. D., Carroll, J. D., Sehitoglu, H., & Lambros, J. (2012). Slip Transfer and Plastic Strain Accumulation Across Grain Boundaries in Hastelloy X. *Journal of the Mechanics and Physics of Solids, 60*, 1201-1220. doi:10.1016/j.jmps.2012.02.001

ASM Aerospace Specification Metals Inc. (a). (n.d.). *Titanium Ti-6Al-4V (Grade 5), Annealed.* Retrieved June 7, 2017, from ASM: asm.matweb.com

ASM Aerospace Specification Metals Inc. (b). (n.d.). *Titanium Ti-6Al-4V (Grade 5), STA.* Retrieved June 7, 2017, from ASM: asm.matweb.com

ASTM International. (2016). ASTM E 837-08: Standard Test Methods for Tension Testing of Metallic Materials. Retrieved January 5, 2017

Banerjee, D., & Williams, J. (2013). Perspectives on Titanium Science and Technology. *Acta Materiala*, 844-879. doi:10.1016/j.actamat.2012.10.043

Baufield, B., Van der Biest, O., & Gault, R. (2010). Additive Manufacturing of Ti-6Al-4V Components by Shaped Metal Deposition: Microstructure and Mechanical Properties. *Materials and Design*, S106-S111. doi:10.1016/j.matdes.2009.11.032

Brandl, E., Baufield, B., Leyens, C., & Gault, R. (2010). Additive Manufactured Ti-6Al-4V Using Welding Wire: Comparison of Laser and Arc Beam Deposition and Evaluation with respect to Aerospace Material Specifications. *Physics Procedia*, 595-606. doi:10.1016/j.phpro.2010.08.087

Carroll, B. E., Palmer, T. A., & Beese, A. M. (2015). Anisotropic Tensile Behavior of Ti-6Al-4V Components Fabricated with Directed Energy Deposition Additive Manufacturing. *Acta Materiala*, 309-320. doi:10.1016/j.actamat.2014.12.054

Carroll, J. (2011). *Relating Fatigue Crack Growth to Microstructure via Multiscale Digital Image Correlation.* University of Illinois at Urbana-Champaign, Department of Mechanical Engineering, Urbana.

Carroll, J. D., Abuzaid, W., Lambros, J., & Sehitoglu, H. (2013). High Resolution Digital Image Correlation Measurements of Strain Accumulation in Fatigue Crack Growth. *International Journal of Fatigue, 57*, 140-150. doi:10.1016/j.ijfatigue.2012.06.010

Carroll, J., Abuzaid, W., Lambros, J., & Sehitoglu, H. (2010). An Experimental Methodology to Relate Local Strain to Microstructural Texture. *Review of Scientific Instruments, 81*(8), 08373. doi:10.1063/1.3474902

Castells, R. (2016, June 29). *DMLS vs SLM 3D Printing for Metal Manufacturing.* Retrieved from Element Materials Technology Web Site: http://www.element.com

Das, S. (2003). Physical Aspects of Process Control in Selective Laser Sintering of Metals. *Advanced Engineering Materials, 5*(10), 701-711. doi:10.1002/adem.200310099

Dutta, B., & Froes, F. H. (2016). *Additive Manufacturing of Titanium Alloys: State of the Art, Challenges, and Opportunities.* Boston: Elsevier Inc. doi:10.1016/B978-0-12-804782-8.00003-3

Facchini, L., Magalini, E., Robotti, P., Molinari, A., Hoges, S., & Wissenbach, K. (2010). Ductility of a Ti-6Al-4V Alloy Produced by Selective Laser Melting of Prealloyed Powders. *Rapid Prototyping Journal, 16*(6), 450-459. doi:10.1108/13552541011083371

Gibson, I., Rosen, D., & Stucker, B. (2015). *Additive Manufacturing Technologies: 3D Printing, Rapid Prototyping, and Direct Digital Manufacturing 2nd Edition.* New York: Springer. doi:10.1007/978-1-4939-2113-3

Gong, H., Rafi, K., Gu, H., Janaki Ram, G., Starr, T., & Stucker, B. (2015). Influence of Defects on Mechanical Properties of Ti-6Al-4V Components Produced by Selective Laser Melting and Electron Beam Melting. *Materials and Design*, 545-554. doi:10.1016/j.matdes.2015.07.147

GPI Prototype & Manufacturing Services. (n.d.). *DMLM - Direct Metal Laser Melting.* Retrieved June 9, 2017, from GPI Prototype & Manufacturing Services Web Site: http://gpiprototype.com/

Islam, M., Purtonen, T., Piili, H., Salminen, A., & Nyrhila, O. (2013). Temperature Profile and Imaging Analysis of Laser Additive Manufacturing of Stainless Steel. *Physics Procedia*, 835-842. doi:10.1016/j.phpro.2013.03.156

ISO/ASTM International. (2013). *ISO/ASTM 52921:2013(E): Standard Terminology for Additive Manufacturing-Coordinate Systems and Test Methodologies.* Retrieved May 22, 2017

Jonnalagadda, K., Chasiotis, I., Yagnamurthy, S., Lambros, J., Pulskamp, J., Polcawich, R., & Dubey, M. (2010). Experimental investigation of strain rate dependence of nanocrystalline Pt films. *Experimental Mechanics, 50*, 23.

Kasperovich, G., & Hausmann, J. (2013). Thermomechanical Treatment of TiAl64V Alloy Fabricated by Selective Laser Melting: Optimization of Microstructure and Fatigue Properties. *Advanced Materials, Processes and Applications for Additive Manufacturing.* Montreal: MST13 Congress: Materials Science and Technology.

Kelly, S., & Kampe, S. (2004). Microstructural Evolution in Laser-Deposited Multilayer Ti-6Al-4V Builds: Part I. Microstructural Characterization. *Metallurgical and Materials Transactions A, 35A*, 1861-1867.

Kobryn, P., & Semiatin, S. (2001). The Laser Additive Manufacture of Ti-6Al-4V. *JOM*(September), 40-42.

Kobryn, P., & Semiatin, S. (2003). Microstructure and Texture Evolution During Solidification Processing of Ti-6Al-4V. *Journal of Materials Processing Technology*, 330-339.

Lewandowski, J. J., & Seifi, M. (2016). Metal Additive Manufacturing: A Review of Mechanical Properties. *Annual Review of Materials Research, 46*, 151-186.

Lutjering, G. (1998). Influence of Processing on Microstructure and Mechanical Properties of (à+ß) Titanium Alloys. *Materials Science and Engineering*, 32-45.

Margolin, H., & Mahajan, Y. (1978). Void Formation, Void Growth and Tensile Fracture in Ti-6Al-4V. *Metallurgical Transactions A, 9A*(June), 781-791.

McMaster-Carr Supply Company [US]. (2017). *High-Strength Grade 5 Titanium Sheets and Bars.* Retrieved from McMaster-Carr: https://www.mcmaster.com/

Murr, L., Quinones, S., Gaytan, S., Lopez, M., Rodela, A., Martinez, E., . . . Wicker, R. (2009). Microstructure and Mechanical Behavior of Ti-6Al-4V Produced by Rapid-Layer Manufacturing, for Biomedical Applications. *Journal of the Mechanical Behavior of Biomedical Materials, 2*, 20-32. doi:10.1016/j.jmbbm.2008.05.004

Prabhu, A. W., Vincent, T., Chaudhary, A., Zhang, W., & Babu, S. S. (2015). Effect of Microstructure and Defects on Fatigue Behaviour of Directed Energy Deposited Ti-6Al-4V. *Science and Technology of Welding and Joining, 20*(8), 659-669. doi:10.1179/1362171815Y.0000000050

Qiu, C., Adkins, N. J., & Attallah, M. M. (2013). Microstructure and Tensile Properties of Selectively Laser-Melted and of HIPed Laser-Melted Ti-6Al-4V. *Materials Science & Engineering*, 230-239. doi:10.1016/j.msea.2013.04.099

Rafi, H. K., Starr, T. L., & Stucker, B. E. (2013). A Comparison of the Tensile, Fatigue, and Fracture Behavior of Ti-6Al-4V and 15-5 PH Stainless Steel Parts Made by Selective Laser Melting. *International Journal of Advanced Manufacturing Technology*, 1299-1309. doi:10.1007/s00170-013-5106-7

Sandala, R. S. (2012). *Deformation Mechanisms of Two-Phase Titanium Alloys.* University of Manchester, Engineering and Physical Sciences. Manchester: University of Manchester.

Seifi, M., Salem, A., Beuth, J., Harrysson, O., & Lewandowski, J. (2016). Overview of Materials Qualification Needs for Metal Additive Manufacturing. *Journal of Materials, 68*(3), 747-764. doi:10.1007/s11837-015-1810-0

Simonelli. (2014). *Microstructure Evolution and Mechanical Properties of Selective Laser Melted Ti-6Al-4V.* Loughborough University, Department of Materials. Loughborough: School of Aeronautical, Automotive, Chemical and Materials Engineering.

Simonelli, M., Tse, Y., & Tuck, C. (2014). Effect of the Build Orientation on the Mechanical Properties and Fracture Modes of SLM Ti-6Al-4V. *Materials Science & Engineering*, 1-11. doi:10.1016/j.msea.2014.07.086

Sutton, M. A., Orteu, J.-J., & Schreier, H. W. (2009). *Chapter 6: In-Plane Measurements.* New York: Springer Science+Business Media, LLC. doi:10.1007/978-0-387-78747-3_6

Thijs, L., Verhaeghe, F., Craeghs, T., Van Humbeeck, J., & Kruth, J.-P. (2010). A Study of the Microstructural Evolution During Selective Laser Melting of Ti-6Al-4V. *Acta Materiala*, 3303-3312. doi:10.1016/j.actamat.2010.02.004

Vrancken, B., Thijs, L., Kruth, J.-P., & Van Humbeeck, J. (2012). Heat treatment of Ti6Al4V produced by Selective Laser Melting: Microstructure and Mechanical Properties. *Journal of Alloys and Compounds*, 177-185. doi:10.1016/j.jallcom.2012.07.022

Wu, X., Liang, J., Mei, J., Mitchell, C., Goodwin, P., & Voice, W. (2004). Microstructures of Laser-Deposited Ti-6Al-4V. *Materials and Design*, 137-144. doi:10.1016/j.matdes.2003.09.009

Xu, W., Brandt, M., Sun, S., Elambasseril, J., Liu, Q., Latham, K., . . . Qian, M. (2015). Additive Manufacturing of Strong and Ductile Ti-6Al-4V by Selective Laser Melting via In Situ Martensite Decomposition. *Acta Materiala*, 74-84. doi:10.1016/j.actamat.2014.11.028

Yang, J., Yu, H., Yin, J., Gao, M., Wang, Z., & Zeng, X. (2016). Formation and Control of Martensite in Ti-6Al-4V Alloy Produced by Selective Laser Melting. *Materials and Design*, 308-318. doi:10.1016/j.matdes.2016.06.117

Zhai, Y., Lados, D. A., Brown, E. J., & Vigilante, G. N. (2016). Fatigue Crack Growth Behavior and Microstructural Mechanisms in Ti-6Al-4V Manufactured by Laser Engineered Net Shaping. *International Journal of Fatigue*, 51-63. doi:10.1016/j.ijfatigue.2016.08.009